

UC San Diego

UC San Diego Electronic Theses and Dissertations

Title

Microstructure and Mechanical Properties of CoCrFeMnNi High Entropy Alloy

Permalink

<https://escholarship.org/uc/item/5z15m9jf>

Author

Alotaibi, Senhat

Publication Date

2017

Peer reviewed|Thesis/dissertation

UNIVERSITY OF CALIFORNIA, SAN DIEGO

Microstructure and Mechanical Properties of CoCrFeMnNi High Entropy Alloy

A Thesis submitted in partial satisfaction of the requirements
for the degree of Master of Science

in

Engineering Sciences (Mechanical Engineering)

by

Senhat Alotaibi

Committee in Charge:

Professor Marc Meyers, Chair
Professor Shengqiang Cai
Professor Vlado Lubarda

2017

Copyright
Senhat Alotaibi, 2017
All rights reserved.

The Thesis of Senhat Mohammed Alotaibi is approved, and it is acceptable in quality and form for publication on microfilm and electronically:

Chair

University of California, San Diego

2017

Table of Contents

Signature Page	iii
Table of Contents.....	iv
List of Figures.....	vii
List of Tables.....	xi
Acknowledgements.....	xii
Abstract of The Thesis	xiii
1 Introduction	1
1.1 Historical overview of Multicomponent alloys	1
1.2 High Entropy Alloys	3
1.3 Four Core Effects of High Entropy Alloys	5
1.3.1 High Entropy Effect.....	5
1.3.2 Severe Lattice Distortion.....	6
1.3.3 Sluggish Diffusion Effects.....	7
1.3.4 Cocktail effect.....	8
2 Literature Review.....	10
2.1 Multicomponent Alloys	10
2.1.1 Mechanical properties.....	10
2.1.2 Thermal Properties	12
2.1.3 Electrical Properties	13
3 Experimental Procedure	16

3.1	As Received Material	16
3.2	Mechanical Testing	17
3.2.1	Quasi Static Compression	18
3.2.2	Dynamic Compression by Split Hokinson Pressure Bar	19
3.2.3	Microhardness	23
3.3	Microstructure Examination Procedures.....	24
3.3.1	As Received Material Examination.....	24
3.3.2	Deformed specimen Microstructural Examination Preparation	24
4	Results and Discussion	32
4.1	Mechanical Response.....	32
4.1.1	Stress Flow	32
4.1.2	Strain Rate Sensitivity.....	33
4.1.3	Plasticity Constitutive Equation	35
4.2	Microstructure.....	41
4.2.1	Chemical Composition	41
4.2.2	Elemental Analysis by EDX	42
4.2.3	Microstructural Characterization.....	45
4.2.4	X-ray powder diffraction (XRD).....	46
4.2.5	Adiabatic Shear Band Evolution	47
4.2.6	Microstructure inside the adiabatic shear band.....	55
4.2.7	Microhardness	67

4.3	Finite Element Simulation	68
4.3.1	Numerical Model	69
4.3.2	Material Definition	72
4.3.3	Model validation	78
4.3.4	Evolution of the shear band	79
5	Conclusion	88
6	References	90

List of Figures

Figure 1 Historical revolution of materials [1].	1
Figure 2 Publications of Multicomponent alloys [4].	3
Figure 3 Alloys Entropy classification [4].	5
Figure 4 Lattice distortion in the high entropy alloys [14].	7
Figure 5 Activation energy to melting temperature ratio for Cr, Mn, Fe, Co and Ni and its high entropy alloy [8], [9],	8
Figure 6 Hardness of the $Al_xCoCrCuFeNi$ alloys as a function of Al content [10].	9
Figure 7 Stress and Hardness with increasing temperature for $Al_{0.5}CoCrCuFeNi$ [27].	10
Figure 8 Strength and toughness of at room and cryogenic temperatures of $CoCrFeMnNi$ [13].	11
Figure 9 Ashby graph of high entropy alloys showing superior fracture toughness and strength in comparison with other major materials [13].	12
Figure 10 thermal conductivity with increasing temperature for $Al_xCoCrFeNi$ [14].	13
Figure 11 Electrical resistivity of for temperature 280K to 400K $Al_xCoCrFeNi$ [14] ; H refer to Al content.	14
Figure 12 Electrical resistivity of for temperature 0K to 400K $Al_xCoCrFeNi$ [14] ; H refer to Al content.	15
Figure 13 Dimension of hat shape specimen in mm.	17
Figure 14 Quasi Static mechanical testing machine (Instron Model 3367).	18
Figure 15 Schematic diagram of the split Hopkinson pressure bar.	19
Figure 16 Strain waves recorded by the two strain gauges.	20
Figure 17 Hat shape specimen geometrical configuration.	23
Figure 18 Struers Accutom-2 was used as the cutting machine	25
Figure 19 Ecomet 6 was used for polishing using the SiC papers and polishing cloth...	26
Figure 20 Ultrasonic cleaner.	27
Figure 21 SEM image of the Adiabatic shear band in the hat shape specimen at low temperature.	28

Figure 22 Specimen is milled by ions to the right dimensions.....	29
Figure 23 Specimen is left out by a probe.....	30
Figure 24 Specimen is attached to a grid.....	30
Figure 25 True stress-true strain curves of the CoCrFeMnNi high-entropy alloy at room temperature.....	32
Figure 26 True stress-true strain curves of the CoCrFeMnNi high-entropy alloy at 153K.....	33
Figure 27 Strain rate Sensitivity at room temperature	34
Figure 28 Strain rate Sensitivity at 153K.....	34
Figure 29 The strain hardening effect equation was fitted with experimental results to identify the material parameters B and n.....	36
Figure 30 Johnson Cook model was fitted with the experiment results to reflect the strain rate effect and find the parameter C.....	37
Figure 31 Temperature dependent True Stress vs true plastic strain at constant strain rate of CoCrFeMnNi [28].....	38
Figure 32 $\dot{\epsilon}=10^{-4} \text{ s}^{-1}$ at room temperature.....	39
Figure 33 $\dot{\epsilon} =1600 \text{ s}^{-1}$ at room temperature.....	39
Figure 34 $\dot{\epsilon} =10^{-4} \text{ s}^{-1}$ T=153K.....	40
Figure 35 $\dot{\epsilon} =3000 \text{ s}^{-1}$ T=153K.....	40
Figure 36 CoCrFeMnNi has similar atomic weights.....	41
Figure 37 EDX spectrum of CoCrFeMnNi.....	43
Figure 38 Elemental planar scan of the CoCrFeMnNi high entropy alloy	44
Figure 39 EBSD of unreformed CoCrFeMnNi.....	45
Figure 40 Grain sizes measurement of unreformed CoCrFeMnNi.	46
Figure 41 XRD pattern of CoCrFeMnNi.	47
Figure 42 Shear Stress-Strain of the hat shape specimen at 153 K.	48
Figure 43 Shear Stress-Strain of the hat shape specimen at room temperature 300 K.	49

Figure 44 Temperature rise in hat-shape specimen tested at 153K.....	50
Figure 45 Temperature rise in hat-shape specimen tested at room temperature (300K)51	
Figure 46 Specimen at room temperature (N1)	52
Figure 47 Specimen at room temperature (N2))	53
Figure 48 Specimen at low temperature (C1)	54
Figure 49 Specimen at low temperature (C2)	55
Figure 50 TEM image of shear band microstructure.....	56
Figure 51 Higher magnification of TEM image of the microstructure.	57
Figure 52 Grain size distribution inside the shear band.....	58
Figure 53 Deformation nanotwins worked as refinement mechanism and generated additional elongated nanograins.....	59
Figure 54 A higher magnification of TEM image that shows nanotwins forming elongated nanograins.	60
Figure 55 An overview of microstructure inside the shear band.....	61
Figure 56 grain sizes distribution for specimen at room temperature (300K)	62
Figure 57 Random distribution of dislocation at the start of plastic deformation.....	64
Figure 58 Elongated dislocation cells forms a elongated subgrain structure	64
Figure 59 Breakup of elongated subgrains	65
Figure 60 TEM bright field image of dislocation pile-up inside the subgrains.	65
Figure 61 Dark field TEM image of the same subgrain in Fig56 showing the dislocation arrangement in the subgrains.....	66
Figure 62 Ultrafine equiaxed grains	67
Figure 63 Microhardness measurement of this high entropy alloy in comparison with 316L austenitic stainless steel.....	68
Figure 64 Axisymmetric model of the hat shape specimen	70
Figure 65 A zoom into the external corner shows the structured and fine mesh size in the designed shear band zone.	71

Figure 66 The cylindrical sample meshed with two plate for applying the load.	72
Figure 67 Strain dependent true stress vs true plastic strain of CoCrFeMnNi	74
Figure 68 Temperature dependent True Stress vs true plastic strain at constant strain rate of CoCrFeMnNi [22].....	75
Figure 69 Temperature dependent elastic Modulus of CoCrFeMnNi [22].....	75
Figure 70 Strain rate dependent plasticity model was incorporated in Abaqus as tabular data for CoCrFeMnNi.....	76
Figure 71 Temperature dependent plasticity model was incorporated in Abaqus as tabular data for CoCrFeMnNi.	77
Figure 72 Stress flow comparison between experimental, tabular model and Johnson Cook model results.	79
Figure 73 Effective stress at 10 μ s	80
Figure 74 Effective plastic strain at 10 μ s	81
Figure 75 Temperature Distribution at 10 μ s.....	82
Figure 76 Plastic strain started to grow from each corner and form shear band along the model.....	83
Figure 77 The hat shape specimen continue to deform by rolling in the exterior corner at 50 μ s.	84
Figure 78 Fully grown plastic strain band at 190 μ s the end of the simulation.....	85
Figure 79 Temperature profile of the adiabatic shear band in the model.....	86
Figure 80 Selected path to measure the temperature rise across the shear band	86
Figure 81 Temperature profile for a path perpendicularly crossing the shear band, the thickness of the shear band is indicated.	87

List of Tables

Table 1 Configurational Entropy of equitomic alloys with n number of elements (4)	5
Table 2 Specimens' Dimensions for static compression tests.	16
Table 3 Specimens' Dimensions for Dynamic compression tests.	16
Table 4 Chemical Composition	41
Table 5 Electronegativity of pure elements	42
Table 6 Material Properties.....	73

Acknowledgements

I would like to acknowledge Prof. Marc Meyers' support and effort in guiding me through the whole time while working on this thesis in the last two years and his support of being the chair committee.

I would like to thank Prof. Cai and Prof. Lubarda for availing the time and being my thesis committee members and their valuable input.

I would like to acknowledge the assistance and guides by Zhezhou Li throughout the whole period I spent working on this thesis at UCSD. He has provided his guides on all the work conducted in this thesis.

I would like Prof. Olivia and her students Kaytya Kritsuk and Jungmin Ha to perform the XRD analysis on this high entropy alloy.

I would like to thank Dr. Bingfeng Wang at Central South University in China, for providing CoCrFeMnNi high entropy for testing and examination.

I would like to thank Shiteng Zhao for his support and input and Andrei Pissarenko for his extended support and guidance to complete finite element simulations

Abstract of The Thesis

Microstructure and Mechanical Properties of CoCrFeMnNi High Entropy Alloy

by

Senhat Alotaibi

Master of Science in Engineering Sciences (Mechanical Engineering)

University of California, San Diego, 2017

Professor Marc Meyers, Chair

High entropy alloys are newly discovered class of metal alloys. It gains many researchers' attention due to their good and exceptional mechanical properties. This work aims to examine CoCrFeMnNi mechanical response at different strain rates and temperatures. In addition, to studying the adiabatic shear band evolution and the mechanism of grains refinement inside the shear band. Microhardness were also

measured inside and outside the shear band. The microstructure was examined by optical microscopy, SEM, EBSD and TEM.

CoCrFeMnNi improve its strength with lowering temperature and increasing the strain rate. In addition, adiabatic shear bands were clearly overserved in CoCrFeMnNi hat shape specimens at 153K and 300K. The grains inside the shear band were extremely refined to equiaxed nanograins at 153K while grains were refined to ultrafine equiaxed grains at the test conducted at 300K.

There were dual refinement mechanisms; the deformation twinning and rotational dynamic recrystallization. The initial average grain size was 10 μm while the refined equiaxed nanograins were between 0.05-0.2 μm for 153K test while between 0.25-0.35 μm for 300K test. TEM images shows evidence that the difference in the refinement factor for these tests is due to the increase of twinning density at lower temperature for specimen tested at 153K. CoCrFeMnNi show excellent microhardness inside the shear band and superior property compared with 316L austenitic stainless steel.

Adiabatic shear band was also observed in finite element model. The numerical model shows good approximation with the actual results and also used to validate the developed Johnson Cook plasticity model.

1 Introduction

1.1 Historical overview of Multicomponent alloys

Ancient civilizations began discovery of pure metals such as gold and copper. Materials availability and variety has limited humans' ability to design and invent. Therefore, cultural development and achievement was dated by the type of metals discovered such as stone age, Copper age (5000–3000 BC), Bronze age (3000–1000 BC) and Iron age (from 1000 BC) [26]. Nowadays, humans have incredible variation in materials at their disposal. Below Fig.1 Shows the materials revolution and development with time. It is evident that in the last 60 years, metals, composites and ceramic had significant importance in today's applications.

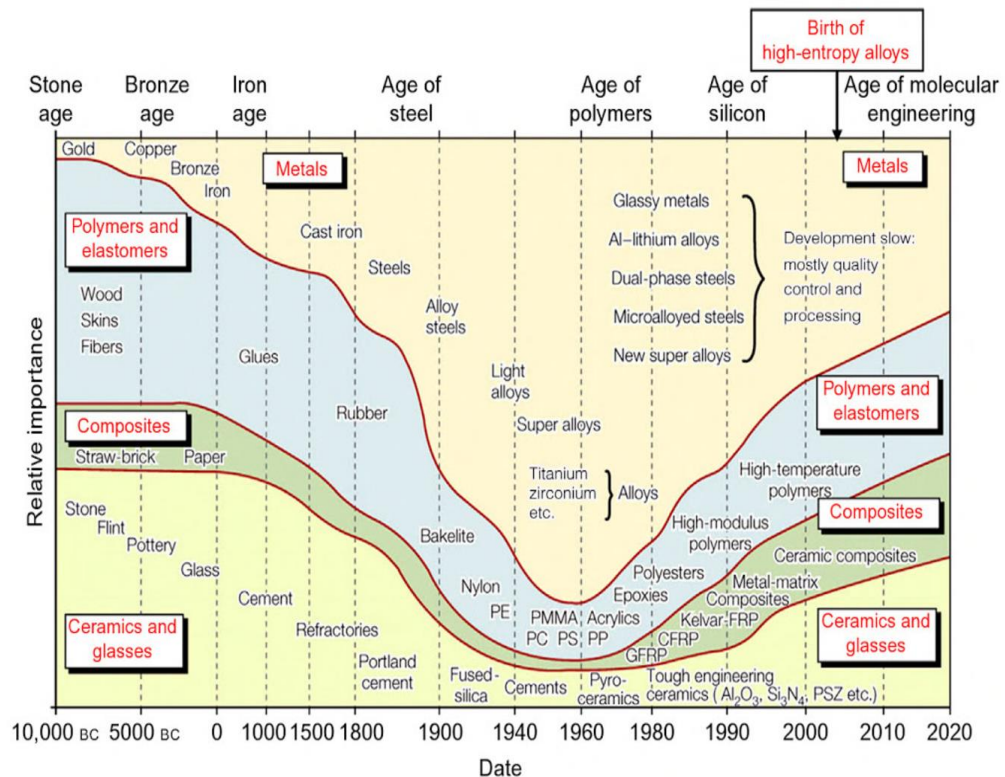


Figure 1 Historical revolution of materials [1].

Alloying is one of the major techniques to produce new materials with desired properties. During the first industrial revolution in mid-18th century in England, many

alloying materials were produced to various applications such as steam powered railways, boats and ships [2]. In 1930s, superalloys evolved due to gas turbines technology development in United States of America. In addition, there were several special alloys that has developed in last 60 years includes intermetallic, quasicrystals and metallic glasses.

Scientists has kept progress development of alloys, in 1981, Brian Cantor and his student Alain Vincent started exploring multicomponent alloys at Bradford University in England. The main alloying strategies was to mix different equiatomic elements at equal portions. For this type of alloys, there is no expectations of the mechanical properties compared with conventional alloys that use one principle element or one compound concept. Cantor's first multicomponent alloy was $\text{Co}_{20}\text{Cr}_{20}\text{Fe}_{20}\text{Mn}_{20}\text{Ni}_{20}$, this alloys forms a single solid solution FCC. Hence, Cantor has introduced this work in 2004 by publication in the Journal Material Science and Engineering A, titled "Microstructural development in equiatomic multicomponent alloys" [3]. Since then, multicomponent elements gain significant considerations by researchers and hence publications have risen significantly as shown in Fig.2.

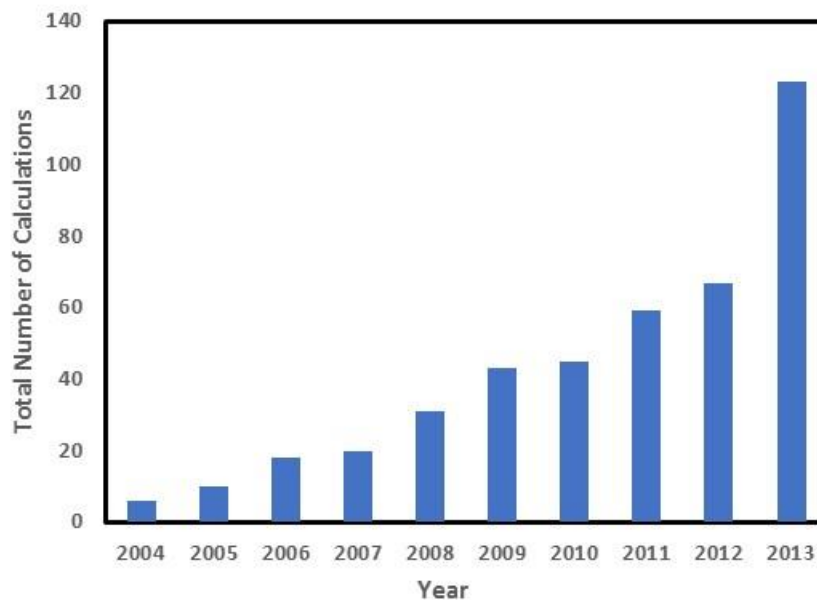


Figure 2 Publications of Multicomponent alloys [4].

It should be clarified here the naming of this special type of alloys is not well defined. Cantor in 2014 [5] has published an article to differentiate between these the names that have been adopted for this alloys in the literature. Cantor has found different multicomponent that do not exhibit high entropy and yet still named high entropy alloys. Cantor states that multicomponent alloy should be used the generalized name for elements mixed at the same or near proportions and are equiatomic. However, if an alloy shows high configurational entropy, then it can be called high entropy alloy. These names are not yet standardized and might be mixed in some of current literature.

1.2 High Entropy Alloys

High entropy alloys are multicomponent alloys but are distinguished in obtaining high entropy effect and a single phase structure. Yeh [11] defines high entropy alloys as multiple elements, often five or more in equiatomic or near equiatomic ratios with high configurational entropy.

Configuration entropy of an alloy system is defined by Boltzmann's equation:

$$\Delta S_{conf} = k \ln w$$

Where

k is boltzmann's constant

W is the number of ways to mixing elements

Hence it can be simplified as

$$\Delta S_{conf} = -R \sum_{i=1}^n X_i \ln X_i$$

Where

n is the number of element in the alloy

Xi is the mole fraction

Therefore, for high entropy alloy where all element are equiatomic and have the same mole fraction

$$\Delta S_{conf} = -R \left(\frac{1}{n} \ln \frac{1}{n} + \frac{1}{n} \ln \frac{1}{n} + \dots \dots \dots \frac{1}{n} \ln \frac{1}{n} \right)$$

$$\Delta S_{conf} = -R \left(\ln \frac{1}{n} \right) = R(\ln(n))$$

Where R is the gas constant 8.314 J/K mol.

Configurational entropy increases with increasing elements in alloys as shown in Table below. Fig.3 shows the classification of alloys based on the entropy.

Table 1 Configurational Entropy of equitomic alloys with n number of elements (4)

n	1	2	3	4	5	6	7	8	9	10	11	12
ΔS_{conf}	0	0.69R	1.1R	1.39R	1.61R	1.79R	1.95R	2.08R	2.2R	2.3R	2.4R	2.49R

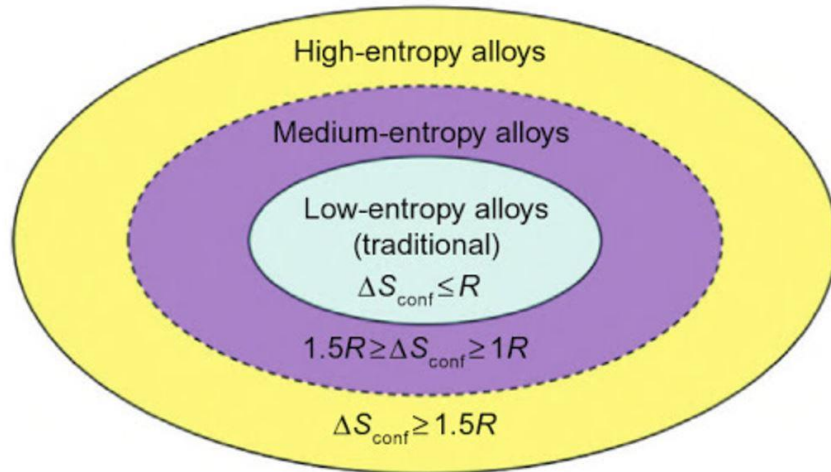


Figure 3 Alloys Entropy classification [4].

1.3 Four Core Effects of High Entropy Alloys

High entropy alloys exhibit good and sometimes superior mechanical properties. There are four core effects that alter the microstructure and mechanical properties [6], [93] compared with the conventional alloys. These four factors are high entropy, sluggish diffusion, severe lattice distortion and cocktail effects.

1.3.1 High Entropy Effect

This effect is considered the most important factor in many of high entropy alloys properties. This effect promotes a stable solid solution since increasing the number of elements decrease mixing free energy by high entropy of mixing.

Gibbs free energy of mixing, ΔG_{mix} is

$$\Delta G_{mix} = \Delta H_{mix} - T\Delta S_{mix}$$

ΔH_{mix} is the mixing enthalpy per mole

ΔS_{mix} is the mixing entropy per mole

T is the Temperature (K)

The mixing entropy composes of the configurational, vibrational, magnetic dipole and electronic randomness. However, the configurational entropy has the major contribution to the total mixing entropy [7]. Therefore, ΔS_{mix} can be assume to be ΔS_{conf} .

1.3.2 Severe Lattice Distortion

Since the high entropy alloys consists of only principle elements, these elements are all solute atoms. Hence, the lattice might be distorted due to the differences in the atomic sizes of these elements. The distortion increases with increases in the atomic sizes differences. The lattice distortion enhances high entropy alloys' solid solution hardening, thermal resistance and x-ray diffuse scattering [8].

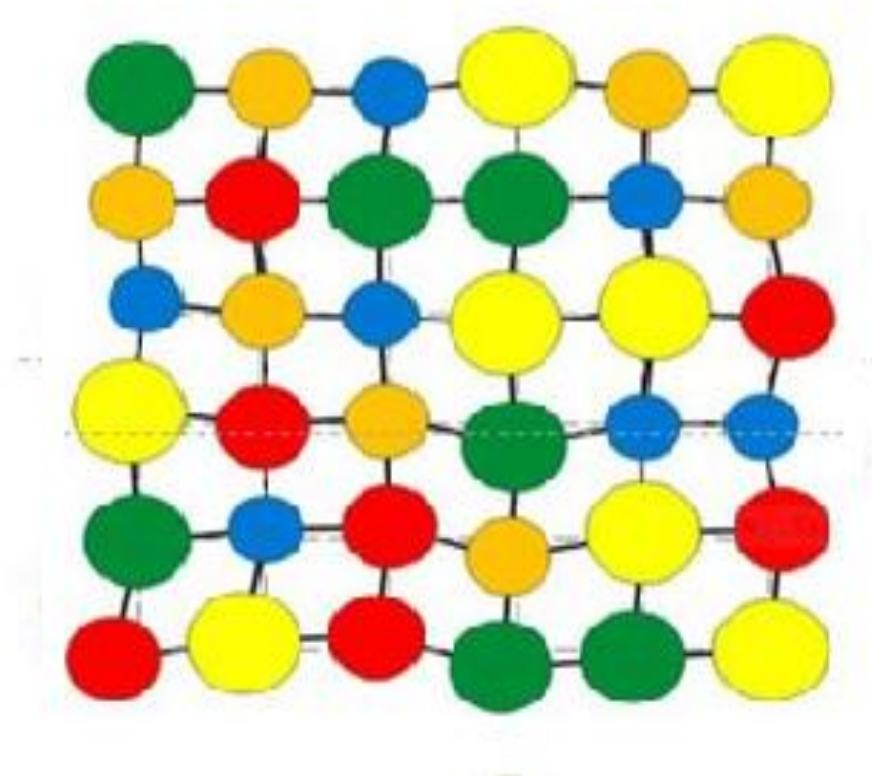


Figure 4 Lattice distortion in the high entropy alloys [14]

1.3.3 Sluggish Diffusion Effects

Tsai [8] studied the diffusion of CoCrFeMnNi high entropy alloy. He found that diffusion is slower with increasing the number of elements in the high entropy alloys in comparison with the pure elements or alloys with few principle elements. Therefore, it is expected that this effect enhances and controls microstructure and properties such as creep resistance [8]. Fig.5 The Y-axis value represent the normalized activation energy defined as the activation energy to melting temperature ratio. This figure shows that the pure elements is corresponding with lowest normalized activation energy shown in red columns, followed by alloys shown in green columns. However, high entropy alloy was the highest shown in blue columns.

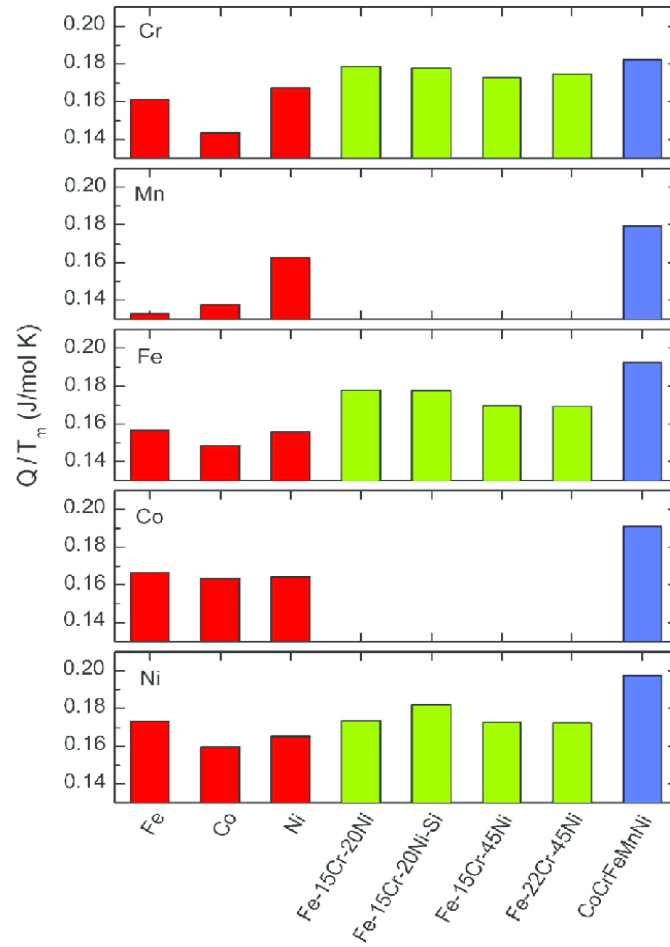


Figure 5 Activation energy to melting temperature ratio for Cr, Mn, Fe, Co and Ni and its high entropy alloy [8], [9].

1.3.4 Cocktail effect

The cocktail effect simply refers to the interaction between the principle elements and the effect of one element on the final alloy. For example, the multicomponent alloy CoCrCuFeNi which consist of five principle elements. Adding and changing the Al content (x%) in $Al_xCoCrCuFeNi$ will enhance the hardness and will form different phases at illustrated in Fig.6 below [10].

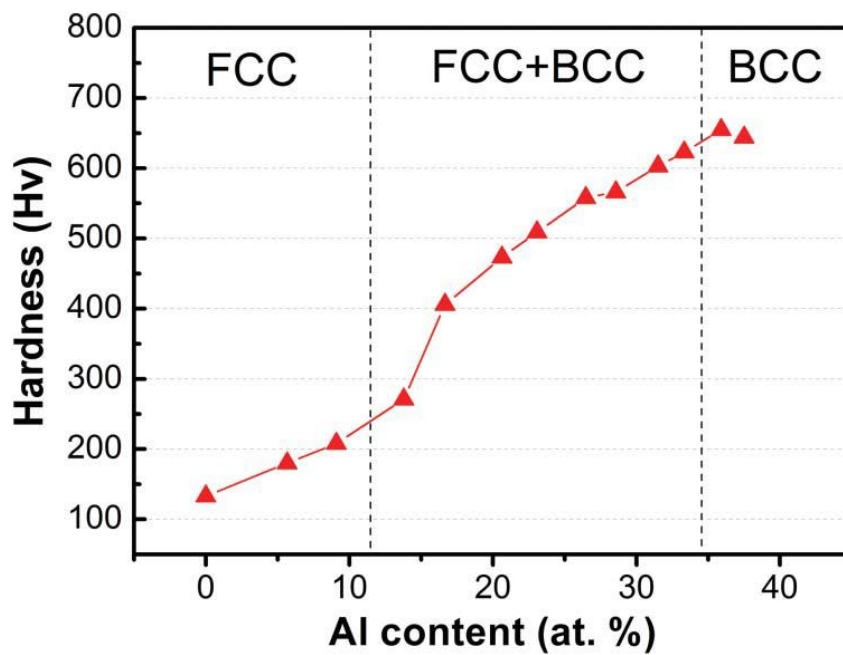


Figure 6 Hardness of the $\text{Al}_x\text{CoCrCuFeNi}$ alloys as a function of Al content [10].

2 Literature Review

2.1 Multicomponent Alloys

2.1.1 Mechanical properties

Multicomponent alloys show good yield strength starting at 300 MPa for FCC high entropy alloys while it can reach yield strength of 3000 MPa for BCC high entropy alloys , In addition, Vickers hardness can reach up to 900 [11],[12].

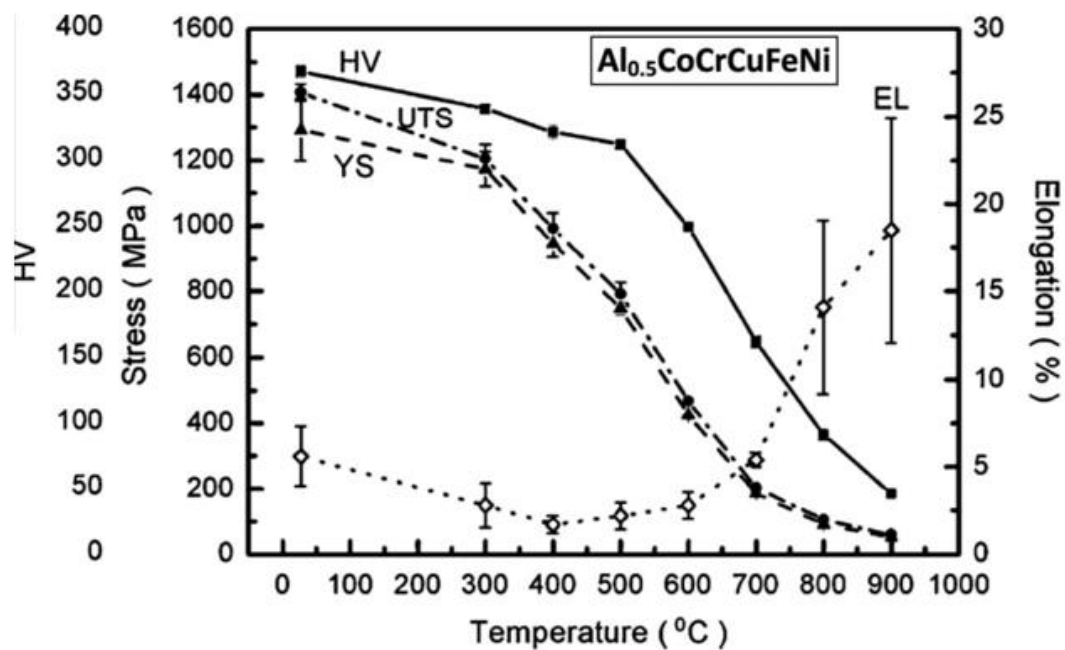


Figure 7 Stress and Hardness with increasing temperature for Al_{0.5}CoCrCuFeNi [27].

One of the extraordinary mechanical properties of CoCrFeMnNi that reported recently is its fracture toughness at cryogenic temperatures. In contrary to most metals and metal alloys, Gludovatz et al [13],[16] has shown that CoCrFeMnNi high entropy alloys exhibits fracture toughness and strength improve with lowering temperatures as shown in Fig.8.

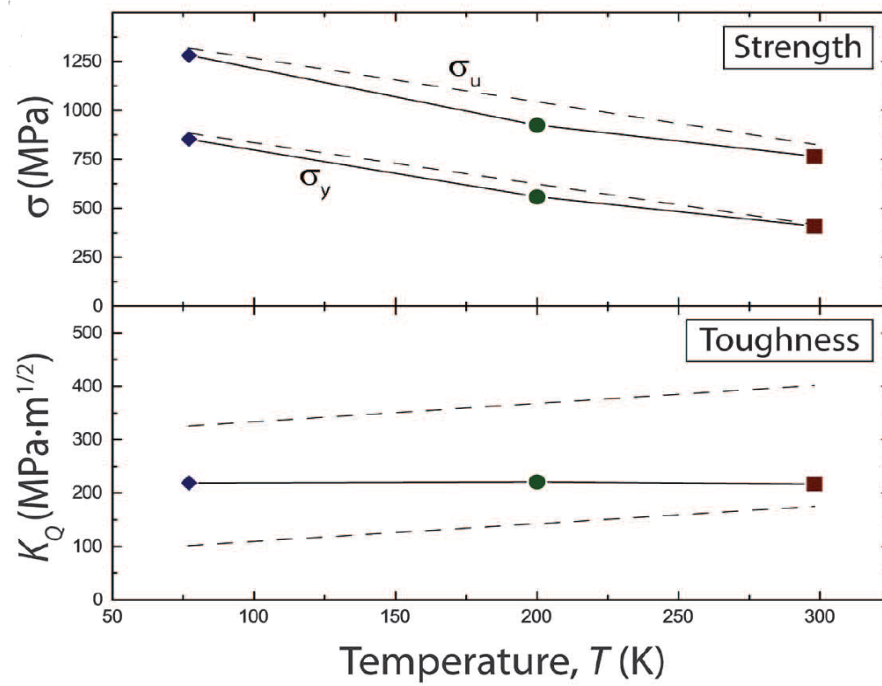


Figure 8 Strength and toughness of at room and cryogenic temperatures of CoCrFeMnNi [13].

Fig.9 shows Ashby graph that illustrate that high entropy alloys exhibits superior fracture toughness and yield strength compared with many materials and in particular many metals and metal alloys

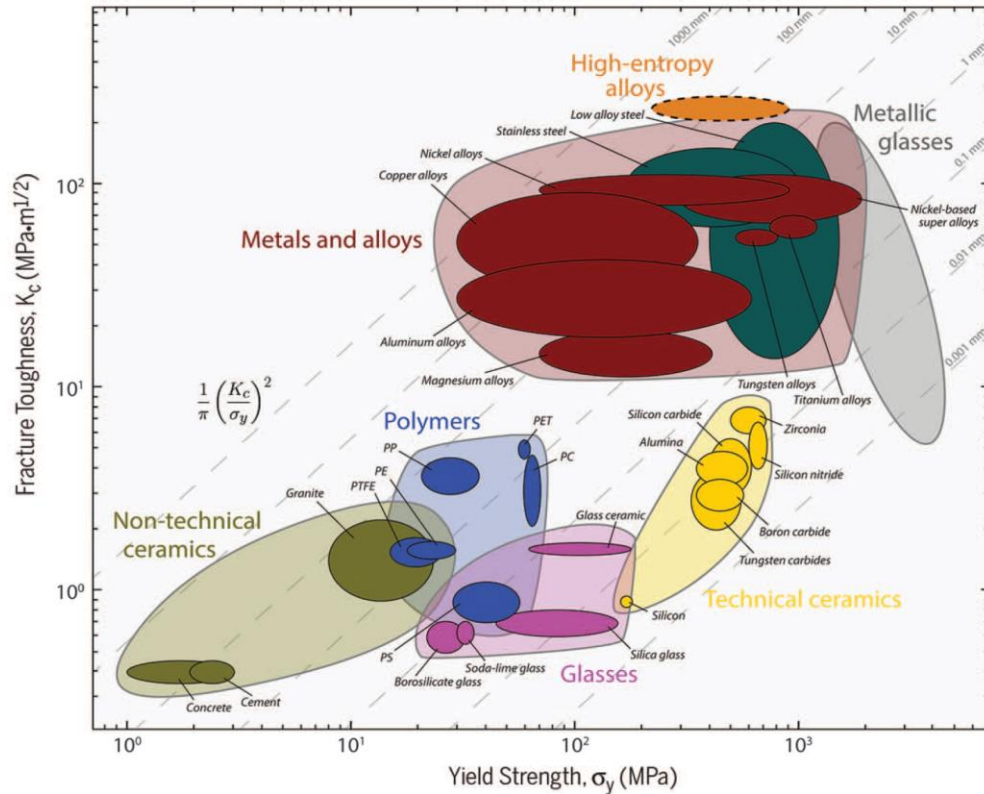


Figure 9 Ashby graph of high entropy alloys showing superior fracture toughness and strength in comparison with other major materials [13].

2.1.2 Thermal Properties

It is reported for some multicomponent alloys containing Al that thermal conductivity increases with increasing the temperature as shown in Fig.10 which is uncommon for pure metals [14]. In addition, changing the Al content results in phases changes and better strength of the material as shown in Fig.6 above.

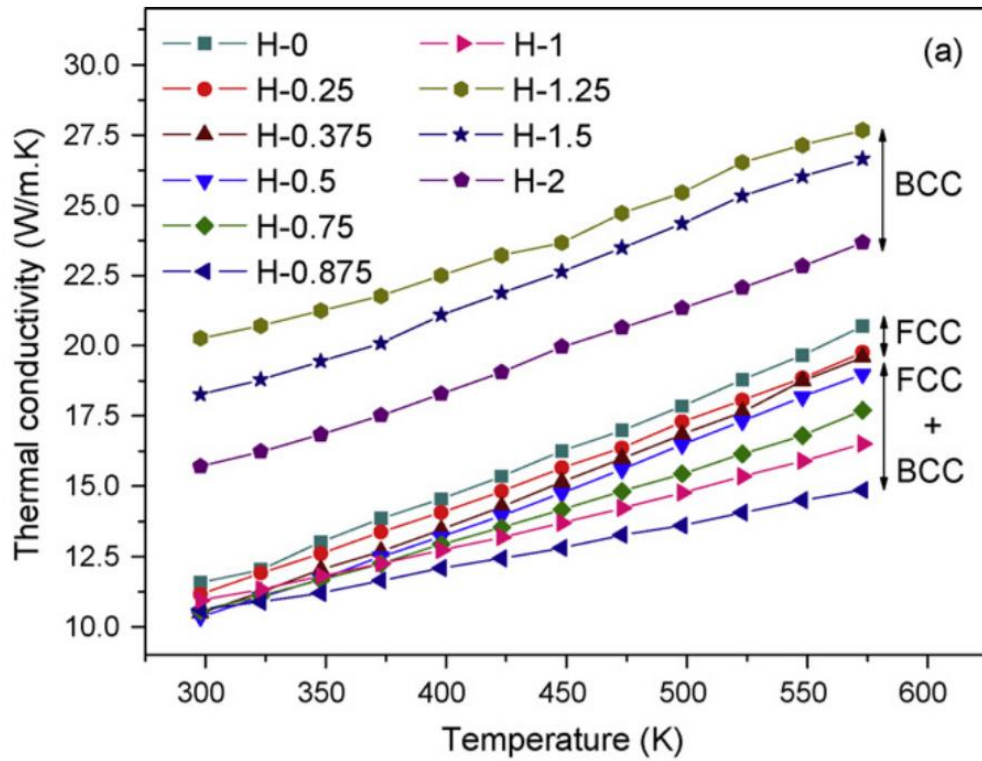


Figure 10 thermal conductivity with increasing temperature for Al_xCoCrFeNi [14].

The level of thermal conductivity of high entropy alloys is around 10-12 W/mK with is low compared with many metal alloys, hence, it might be an opportunity for all plications requiring low thermal conductivity [11].

2.1.3 Electrical Properties

Al_xCoCrFeNi alloys have shown increasing resistivity with increasing temperature, in addition, at lower temperature it shows high resistivity level compared with conventional alloys [14].

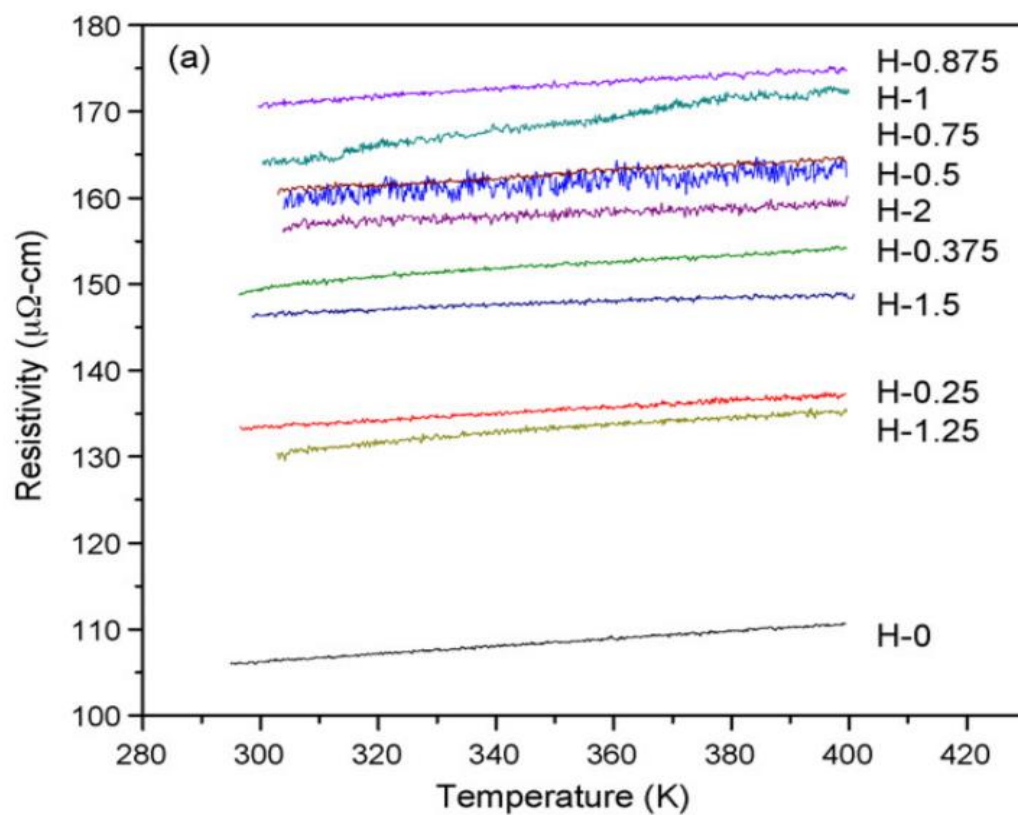


Figure 11 Electrical resistivity of for temperature 280K to 400K $\text{Al}_x\text{CoCrFeNi}$ [14]; H refer to Al content.

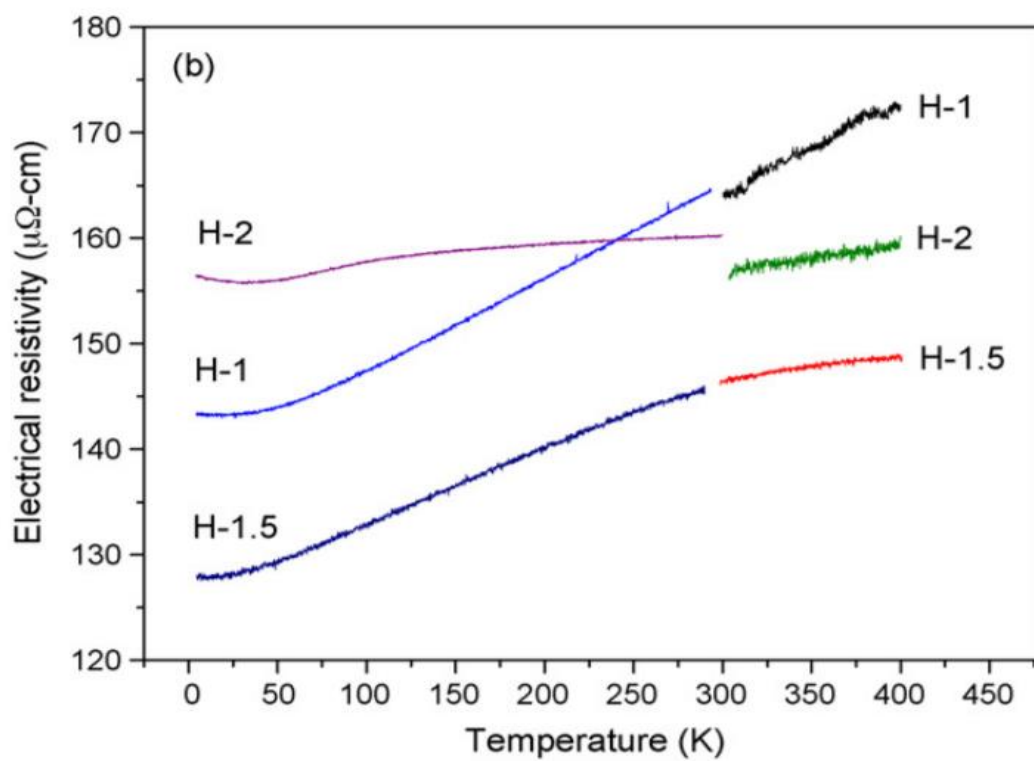


Figure 12 Electrical resistivity of for temperature 0K to 400K $\text{Al}_x\text{CoCrFeNi}$ [14] ; H refer to Al content.

3 Experimental Procedure

3.1 As Received Material

CoCrFeMnNi was manufactured and prepared by Dr. Bingfeng Wang at Central South University in China. Co, Cr, Fe, Mn, Ni pure powders were prepared in equiatomic ratio then heated in a vacuum furnace. The molten powder then dropped through ceramic tube by Argon gas atomization with 4 MPa pressure. The ceramic tube is made with Al₂O₃ and assumed it will not interact with molten powder. This powder then placed into a graphite die of 4 cm and then spark plasma sintering with used to heat the power to around 1000°C [88]. Then, it was mechanically pressurized at 30 MPa and then left for cooling to ambient temperature.

The received material was machined to cylindrical specimen for studying the mechanical response of the material at different strain rate and different temperatures. In addition, hat shape specimens were machined to study the shear band development in this material. Table 2,3 below show the dimensions of the machined specimen for static and dynamic compression tests.

Table 2 Specimens' Dimensions for static compression tests.

Static Compression Test	
Diameter (mm)	Height (mm)
3.42	5.6

Table 3 Specimens' Dimensions for Dynamic compression tests.

Dynamic Compression Test	
Diameter (mm)	Height (mm)
3.441	3.497

Fig.13 below shows the dimension of the hat shape specimens in mm. The top part of the specimen is called the hat while the lower part is called the brim. The reasoning behind this design is explained in 3.2.2.

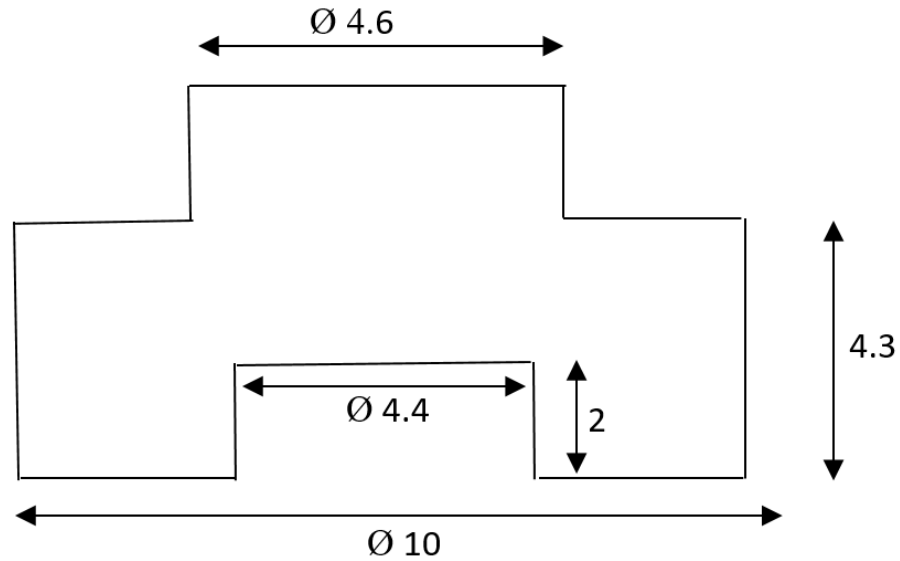


Figure 13 Dimension of hat shape specimen in mm.

3.2 Mechanical Testing

There are two types of mechanical testing conducted on this high entropy alloy. First is the static compression to examine the material low strain rate mechanical response. Second is the dynamic compression using split Hopkinson pressure bar for examine the alloy response at high strain rate. Both tests were conducted for specimen at room temperature and at 153K. The strain rate for the conducted tests range from 10^{-4} s^{-1} to 3000 s^{-1}

3.2.1 Quasi Static Compression

Quasi static compression was conducted on cylindrical specimens by the 3300 Dual column universal testing systems as shown in Fig.14. The top and bottom parts of the specimens and the faces of the two plates' faces of the testing machines were cleaned by the SiC papers.



Figure 14 Quasi Static mechanical testing machine (Instron Model 3367).

In addition, the top and bottom part of the specimen were measured and ensure they are flat enough before the tests were carried out. During testing at low temperature, a box was inserted between the two columns to keep the liquid nitrogen from leaking.

The obtained compressive stress and strain from this equipment is the engineering stress strain and hence need to be converted into the true stress strain.

3.2.2 Dynamic Compression by Split Hokinson Pressure Bar

Split Hokinson Pressure bar(SHPB) is a widely-used test for high strain rate since it was introduced Kolsky in 1949 [78]-[80]. It consists of three bars, the striker, the incident and the transmitted bars as shown in Fig. 15. Two strain gauges are placed at the incident and transmitted bars to record the strain history. All bars are considered elastic and the material used are strong enough to avoid plastic deformation.

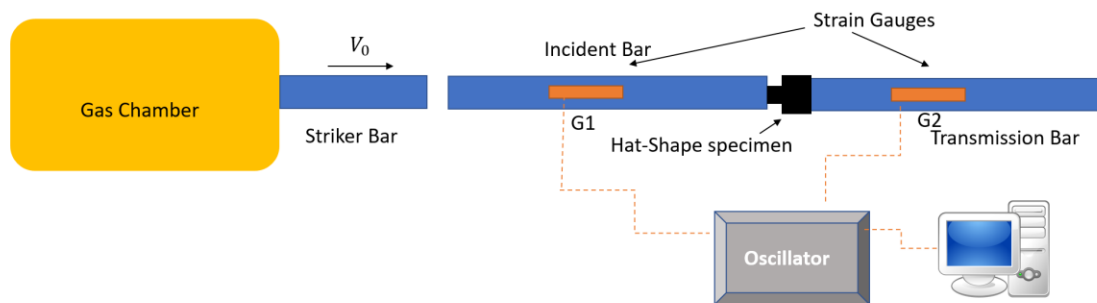


Figure 15 Schematic diagram of the split Hokinson pressure bar.

SHPB tests described as the following [83]; first, a gas chamber is pressurized then the striker bar is propelled with initial velocity (V_0) towards the incident bar to generate a compressive strain wave. The time independent incident strain wave (ϵ_i) is measured at (G1). The wave will be transmitted partially to the specimen and partially reflected to the incident and also recorded again by strain gauge (G1) placed at the mid of the incident bar. The recorded reflected wave represent the reflected strain (ϵ_R). As the specimen

experiences the stress wave, the wave will also propagate into the transmitted bar and recorded by the strain gauge (G2). Hence, this wave is called the transmitted wave and will be converted into transmitted strain (ϵ_T). Typical strain waves are shown in Fig. 16 below

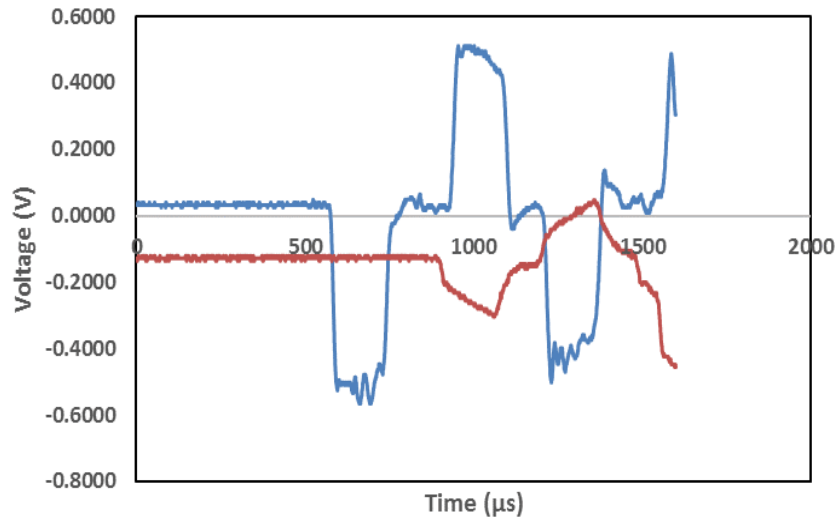


Figure 16 Strain waves recorded by the two strain gauges.

The specimen mechanical response is then calculated from the strain history.

However, the following assumption need to be made:

1. All bars are elastic and remain elastic during the tests.
2. The wave travel is assumed to be in one dimension.
3. The specimen is deforming uniformly and homogeneously.

Hence, the engineering stress and strain can be calculated as as follows:

$$\sigma_e = \frac{EA_b}{A_s} \epsilon_T$$

Where

σ_e the time dependent engineering stress flow

E is young's modulus

A_b is the cross-sectional area of the bar.

A_s is the cross-sectional area of the specimen.

The engineering strain and strain rate are calculated using the following equations

$$\varepsilon_e = -\frac{2C_0}{L_s} \int_0^t \varepsilon_R dt$$

$$\dot{\varepsilon} = -\frac{2C_0}{L_s} \varepsilon_R$$

Where

ε_R reflected strain

L_s is the initial length of the specimen.

C_0 is the longitudinal sound-velocity of the pressure bar defined as shown below

$$C_0 = \sqrt{\frac{E_0}{\rho_0}}$$

The engineering Stress and strain is converted into true stress strain by using the following definition

$$\sigma_T = \sigma_e \times (1 + \varepsilon_e)$$

$$\varepsilon_T = \ln(1 + \varepsilon_e)$$

For the shear stress, shear strain and shear strain rate, the calculation will be dependent on the shear band width since the deformation takes place at this concentrated area of the specimen.

$$\tau = \frac{E_0 A_0}{A_s} \varepsilon_T$$

$$\gamma = -\frac{2C_0}{t_{SB}} \int_0^t \varepsilon_R dt$$

$$\dot{\gamma} = -\frac{2C_0}{t_{SB}} \varepsilon_R$$

Where

τ is shear stress

γ is shear strain

$\dot{\gamma}$ is shear strain rate

t_{SB} the actual shear band thickness

A_s the area of the pressure bar:

$$A_s = \pi \frac{D^2}{4}$$

Where

D is the diameter of the pressure bar approximate 19.5mm

A_0 is the area of the shear band in the specimen.

The below configuration shows the hat shape specimen configuration. The area A_0 is calculated as follows:

$$A_0 = \pi \times \frac{D_e + D_i}{2} \times (L - H - X)$$

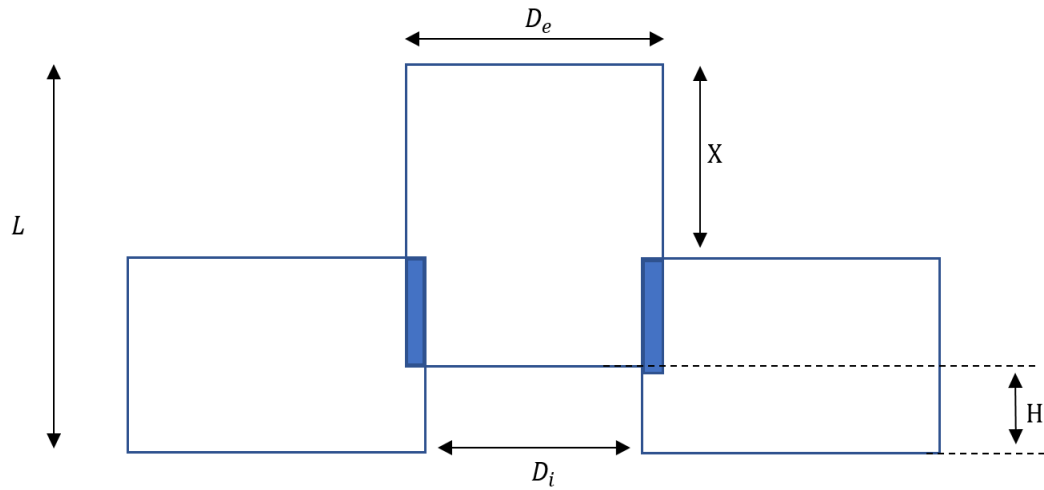


Figure 17 Hat shape specimen geometrical configuration

The specimen is always placed between the transmitted and reflected bars. The specimen is then covered to avoid any projectile that might endanger or harm the students present at the lab. These bars are lubricated by oil to reduce the effects of friction. During low temperature testing, liquid nitrogen was used and placed into a box that covers the specimen.

3.2.3 Microhardness

Hardness is an important mechanical property; hence, hardness was measured for this alloy at the shear band and outside shear band to reveal the hardness enhancement due to microstructural change.

3.3 Microstructure Examination Procedures

This section discusses the procedures of preparing and examining the microstructure of CoCrFeMnNi high entropy alloy.

3.3.1 As Received Material Examination

The received specimen was subjected to microstructural examination as the following:

- Grain size distribution using EBSD.
- Crystal phase identification using X-ray powder diffraction (XRD).
- Elemental planar scan and chemical composition using SEM.

3.3.2 Deformed specimen Microstructural Examination Preparation

Once the specimen is tested and deformed, there are standard procedures that needed to be carried out to show the microstructural evolution under microstructural microscopies. These standard procedures will be briefly discussed below.

3.3.2.1 Cutting

Both cylindrical and hat shape specimens were cut in the direction perpendicular to the applied load. The cutting times varied between one hour to one hour and a half.

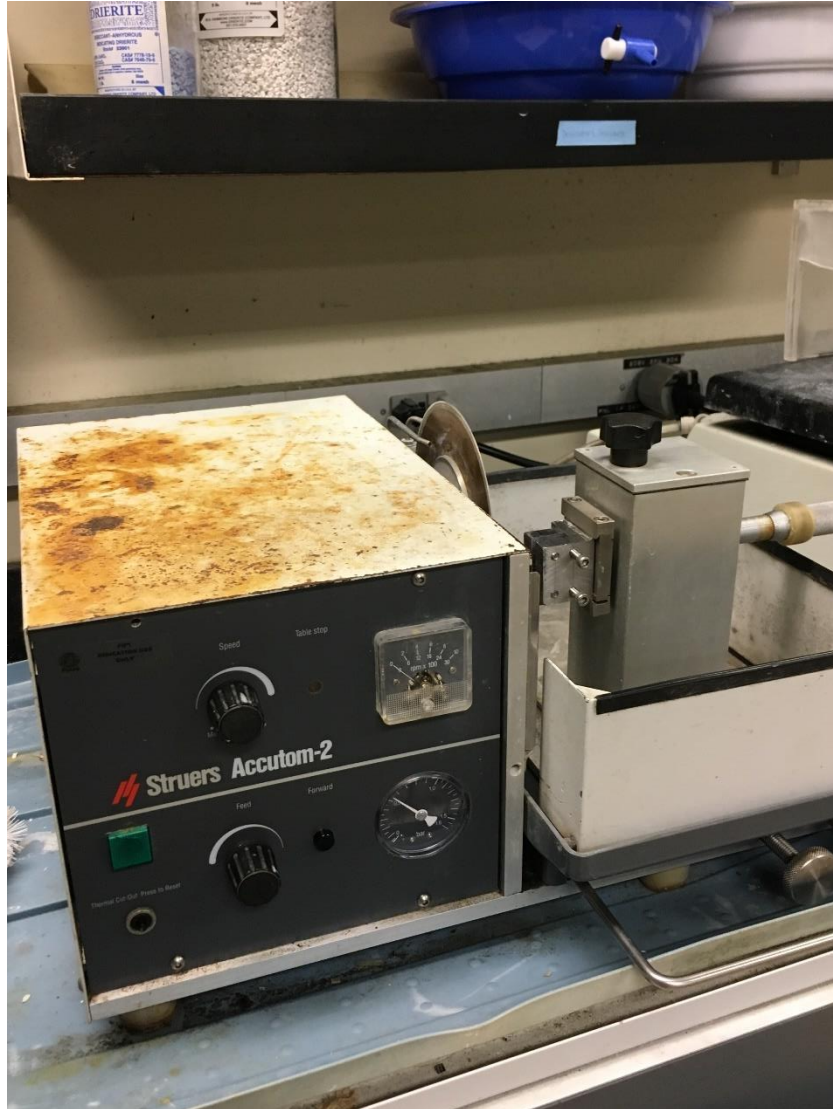


Figure 18 Struers Accutom-2 was used as the cutting machine.

3.3.2.2 Polishing

The specimen is placed in an epoxy then the specimen was grinded with SiC papers from 180 to 4000. The grinding took place on an automated polishing machines. Then, the specimen is further polished with a polishing cloth and viscous Alumina solution. The average time for polish a specimen is between 4-6 hours.



Figure 19 Ecomet 6 was used for polishing using the SiC papers and polishing cloth.

3.3.2.3 Etching

Once the specimen is polished and shows a shiny mirror effect, it needs further etching with a chemical solution to show the microstructure. The selected etching solution for this high entropy alloy 25ml C₂H₅OH + 25ml HCl + 5g CuSO₄.5H₂O. This etching solution was selected after many trials as this material new and there is no published etching solution available in literature. This etching solution is hazardous and cautions

need to be taken handling this solution. The specimen was merged in this solution for 90 second then moved out and merged in Alcohol and finally washed by hot running water for one minute. The etch specimen then directly dried and then merged in alcohol in ultrasonic cleaner for 15 minutes. The ultrasonic cleaner is important to remove residual solution from the specimen and prevent excessive chemical attack in the metal.



Figure 20 Ultrasonic cleaner.

3.3.2.4 Focused Ion Beam (FIB)

The specimens went through the procedures that described earlier that include cutting, polishing and etching before it was ready for FIB. Both at room and at low temperatures, hat shape specimen was prepared for transmission electron microscope (TEM) by focused ion beam (FIB). Before FIB is used, scanning electron microscopy is performed first to identify and locate the adiabatic shear band. Below SEM image is shown and it shows clearly the shear band.

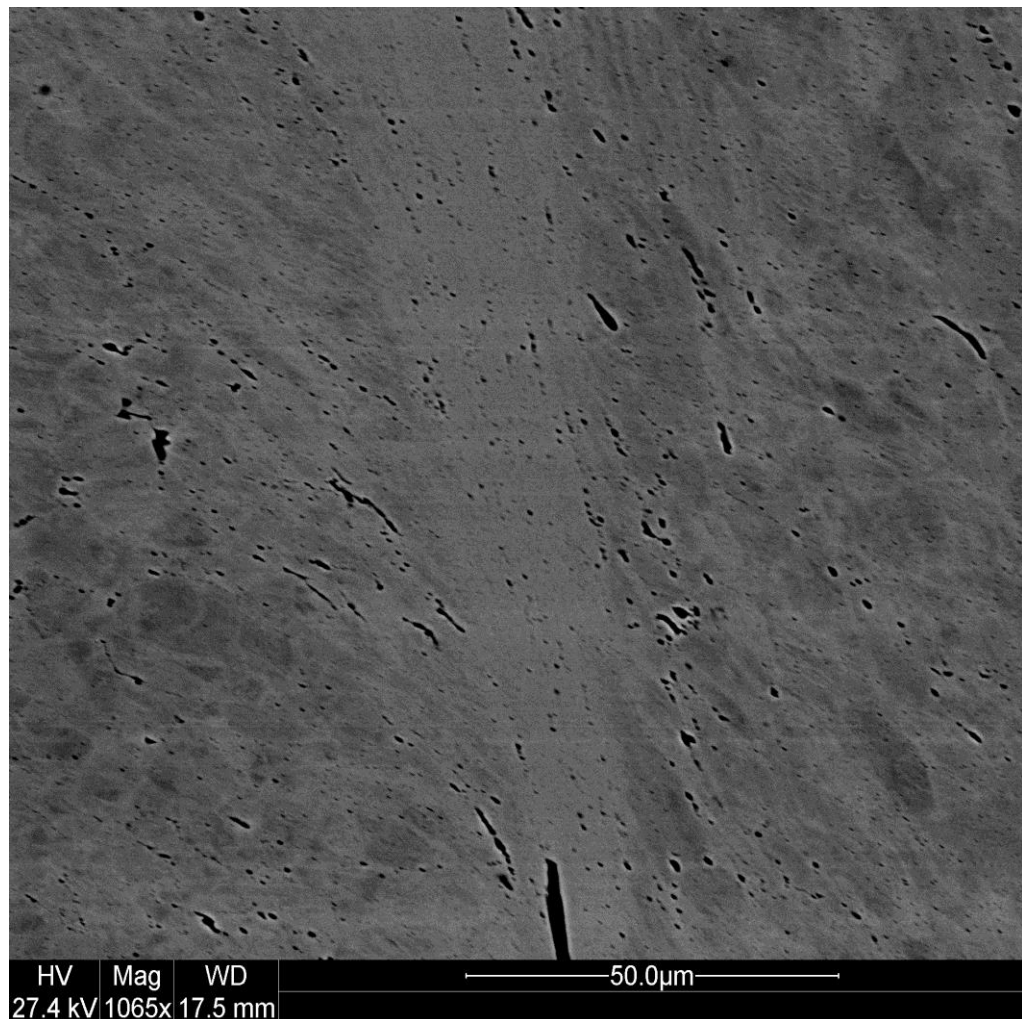


Figure 21 SEM image of the Adiabatic shear band in the hat shape specimen at low temperature.

In FIB, sample first is deposited with Platinum to protect the sample from electron or ion beams. Then, specimen is milled by ions and finally is extracted by a probe as shown in Fig.23. Then the specimen is attached into a grid to be examined by TEM. The TEM specimen dimension is 6 μm by 3 μm .

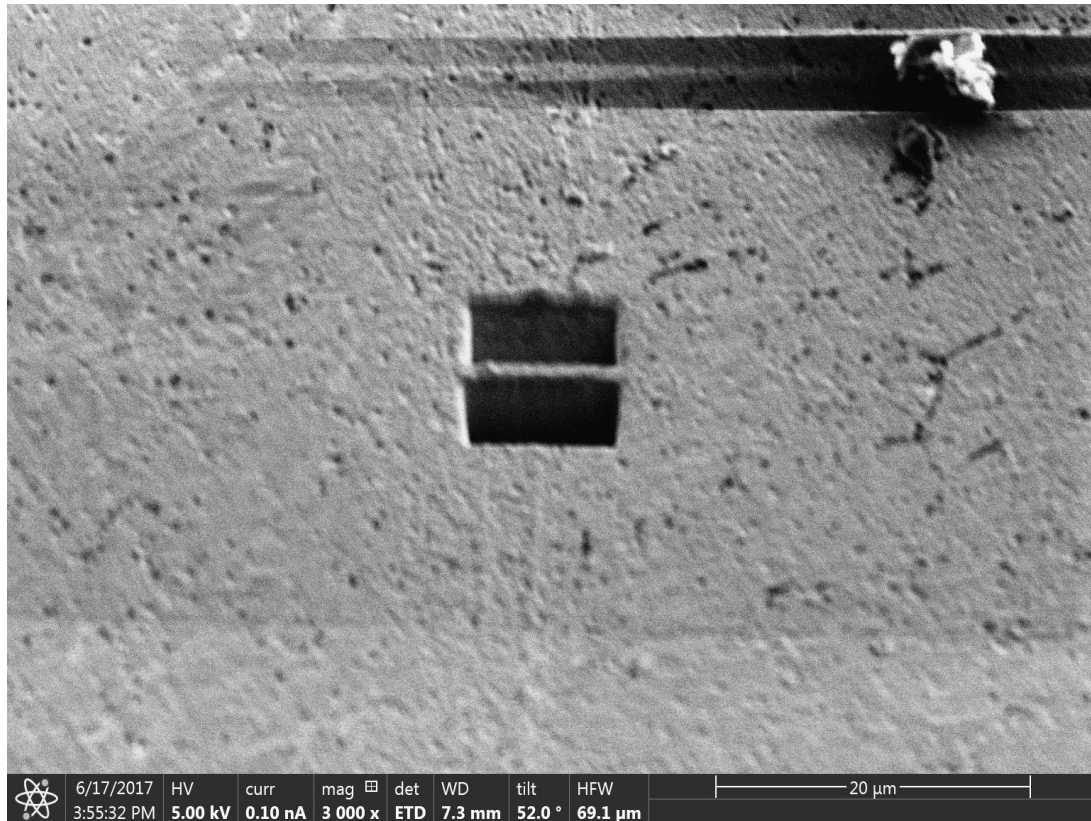


Figure 22 Specimen is milled by ions to the right dimensions.

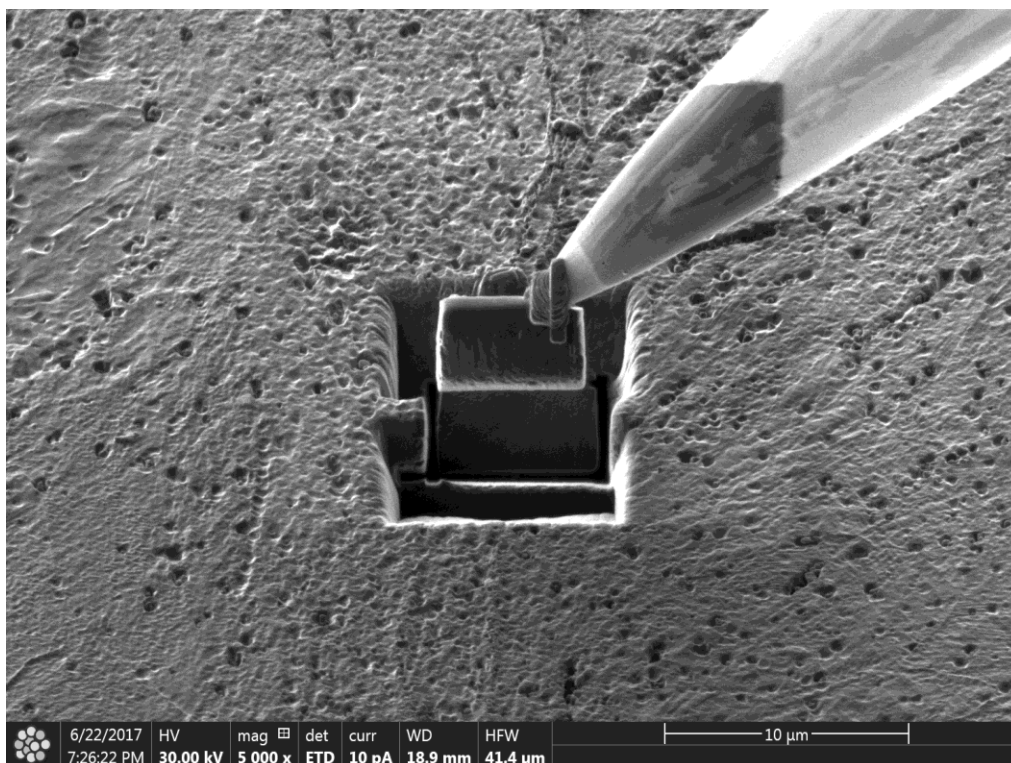


Figure 23 Specimen is left out by a probe.

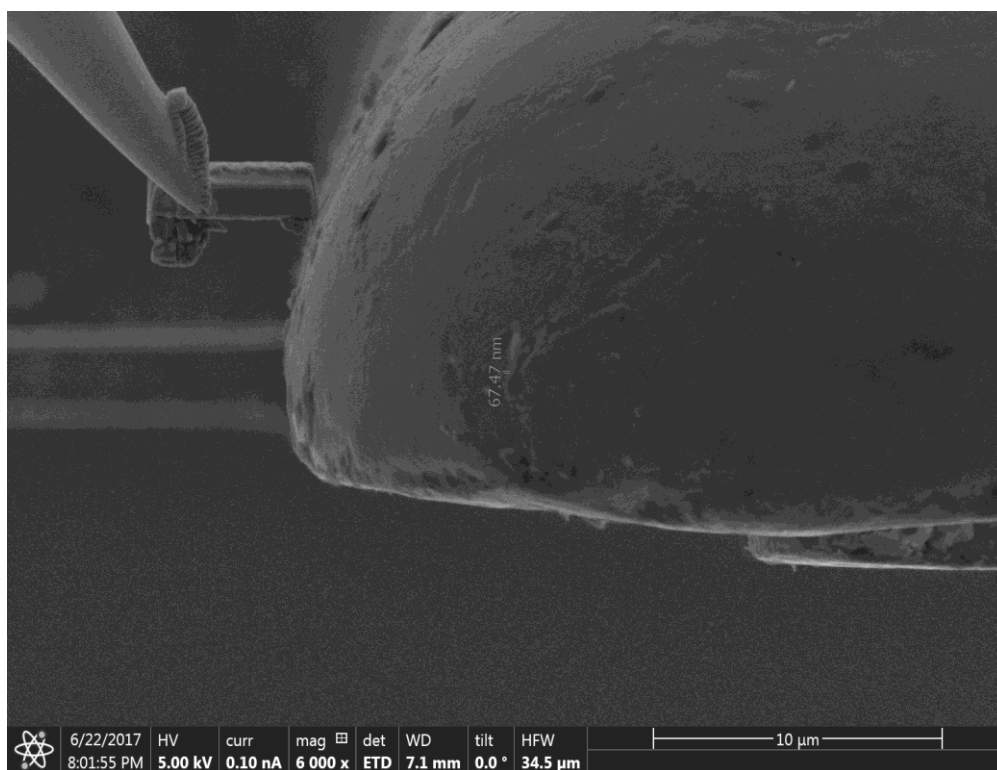


Figure 24 Specimen is attached to a grid.

3.3.2.5 Transmission Electron Microscopy (TEM)

Transmission electron microscope (TEM) was performed on the hat shape specimens at room and low temperatures. This was performed to provide insight into the shear band formation in this high entropy alloy since the optical microscopy and SEM provided only limited information. TEM has the capability to show better resolution of the refined grains inside the adiabatic shear band. The specimen was prepared carefully as described earlier by FIB and then attached on a grid for examination.

4 Results and Discussion

4.1 Mechanical Response

4.1.1 Stress Flow

The true compressive stress versus true strain curves at room temperature and 152K are plotted in Fig.25. and Fig.26 respectively. The yield stress increases with decreasing temperature. At strain rate of 10^{-4} s^{-1} , yield stress jumps from 380 MPa at room temperature to 430 MPa at 153K.

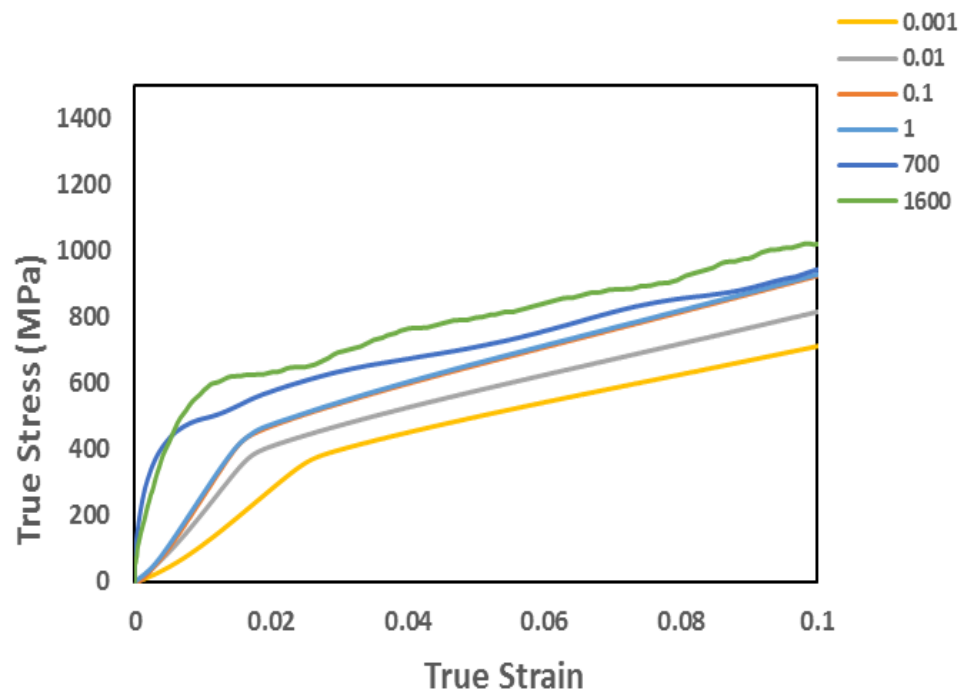


Figure 25 True stress-true strain curves of the CoCrFeMnNi high-entropy alloy at room temperature.

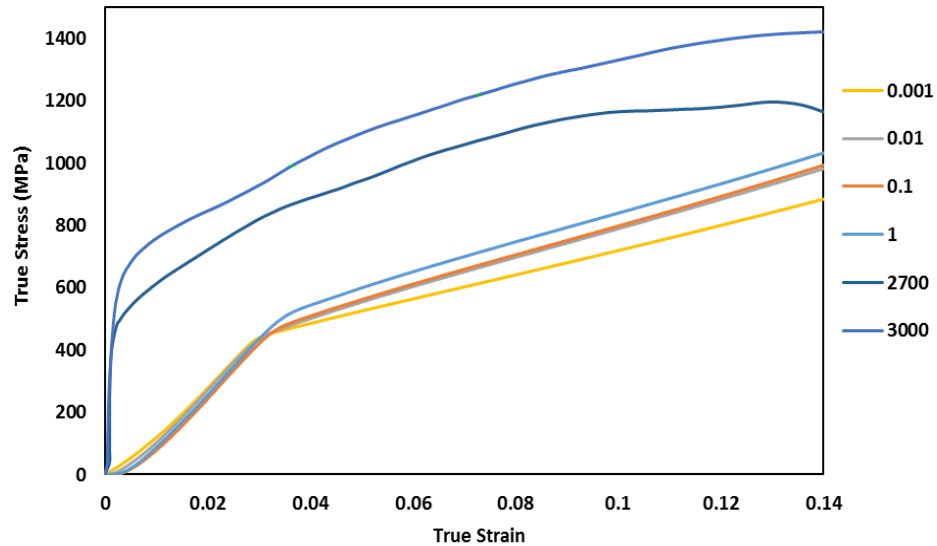


Figure 26 True stress-true strain curves of the CoCrFeMnNi high-entropy alloy at 153K

4.1.2 Strain Rate Sensitivity

The CoCrFeMnNi strengthens with increasing strain rate. At room temperature, the yield stress jump from 380 MPa at strain rate of 10^{-4} s^{-1} to around 540 MPa at 1600 s^{-1} . However, at 153K, the yield stress jump from 430 MPa at strain rate of 10^{-4} s^{-1} to around 650 MPa at 3000 s^{-1} .

Strain rate sensitivity, defined as shown in below equation, were calculated and found to be 0.0246 for tests conducted at room temperature while it is 0.0202 at 153K. Hence, it is evident that CoCrFeMnNi has similar strain rate sensitivity at these two different temperatures.

$$m = \frac{\log(\sigma)}{\log(\dot{\epsilon})}$$

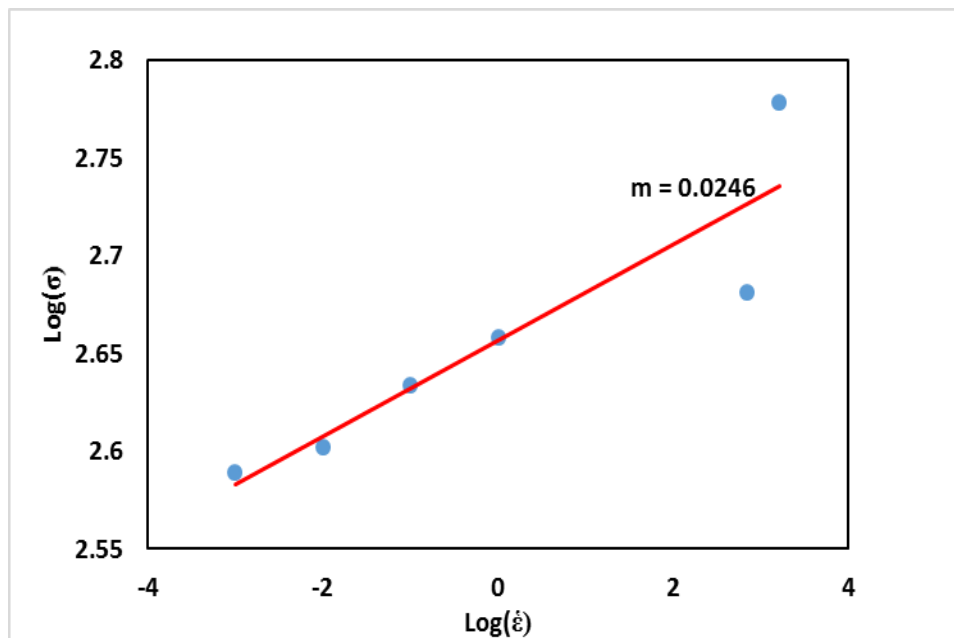


Figure 27 Strain rate Sensitivity at room temperature

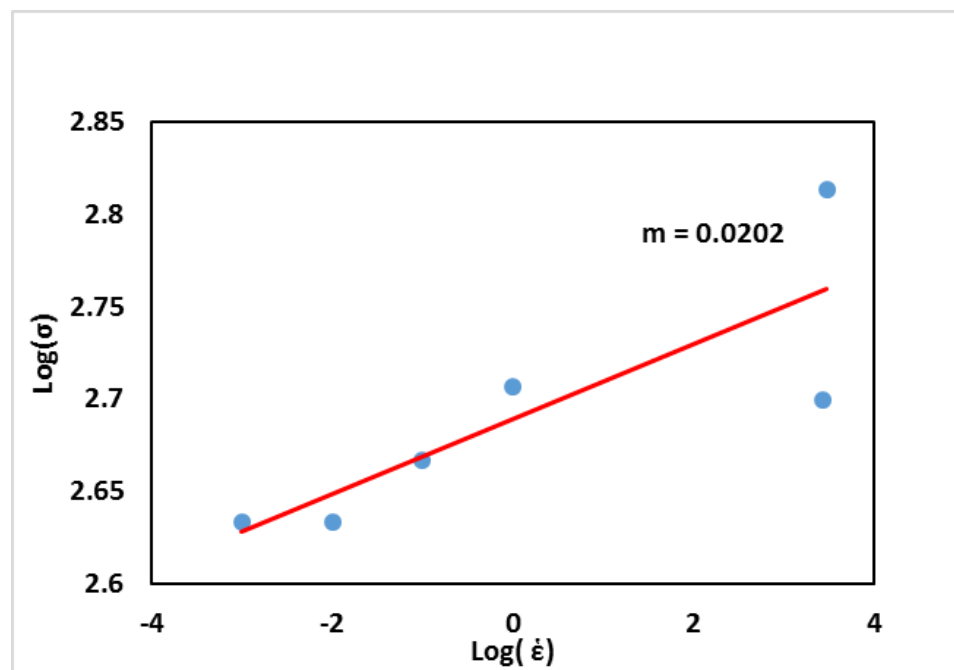


Figure 28 Strain rate Sensitivity at 153K

4.1.3 Plasticity Constitutive Equation

Johnson cook (JC) model [5], [77], [79] is a widely-used plasticity model for metals and metal alloys. It is incorporated in many commercial finite element software. Therefore, JC was developed to describe the inelastic behavior of CoCrFeMnNi.

The model considers the effects of strain hardening, strain rate and thermal effects as illustrated in below equation.

$$\sigma = \underbrace{(A + B\varepsilon^n)}_{\text{Strain Hardening}} \underbrace{\left(1 + C \ln\left(\frac{\dot{\varepsilon}}{\dot{\varepsilon}_0}\right)\right)}_{\text{Strain Rate}} \underbrace{\left[\left(1 - \frac{T - T_{room}}{T_{melting} - T_{room}}\right)^m\right]}_{\text{Thermal Softening}}$$

4.1.3.1 Strain Hardening Effects

The first bracket of the Johnson cook model represents the strain hardening effects on material. A- represents the yield stress, n and B are strain hardening exponent and material parameter taken at reference strain rate $\dot{\varepsilon}_0$. B and n is obtained by fitting the equation $\sigma = (A + B\varepsilon^n)$ into the stress strain curve at strain rate of 10^{-4} s^{-1} that was obtained experimentally. Since A, B and n were obtained at this strain rate, the reference strain rate $\dot{\varepsilon}_0$ was taken to be 10^{-4} s^{-1} . Strain hardening parameters as shown in $\sigma = (388 + 5729\varepsilon^{1.1})$.

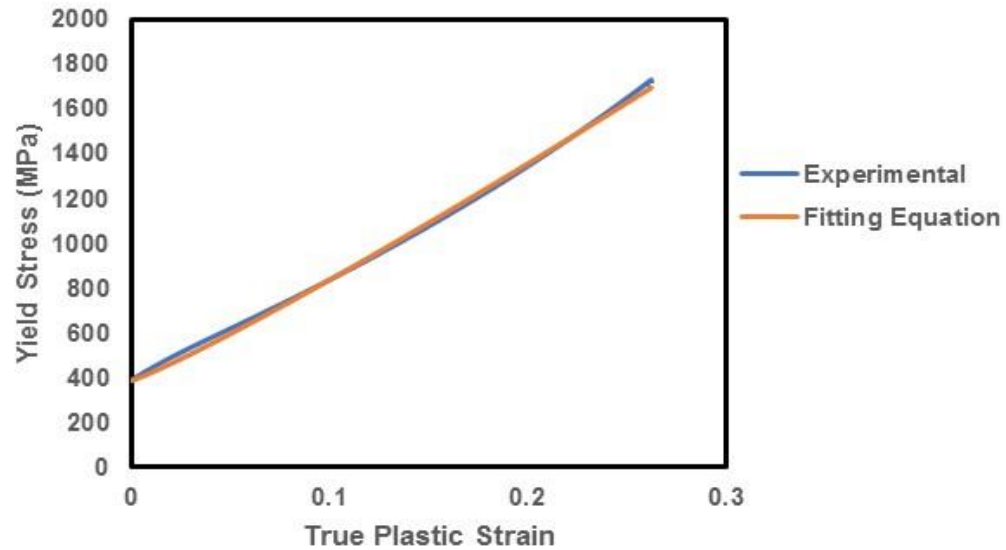


Figure 29 The strain hardening effect equation was fitted with experimental results to identify the material parameters B and n.

4.1.3.2 Strain Rate Effects

Parameter C is a material parameter that will reflect the effect of strain rate on the stress flow. C was determined by fitting two stress strain curve at strain rate of 10^{-4} s^{-1} and 1600 s^{-1} to equation. Note that thermal softening was neglected here since the two curves were at the same temperature hence there is no thermal softening effects.

$$\sigma = (388 + 5729\varepsilon^{1.1})\left(1 - C \ln\left(\frac{\dot{\varepsilon}}{0.001}\right)\right)$$

Where $\dot{\varepsilon}$ is 1600

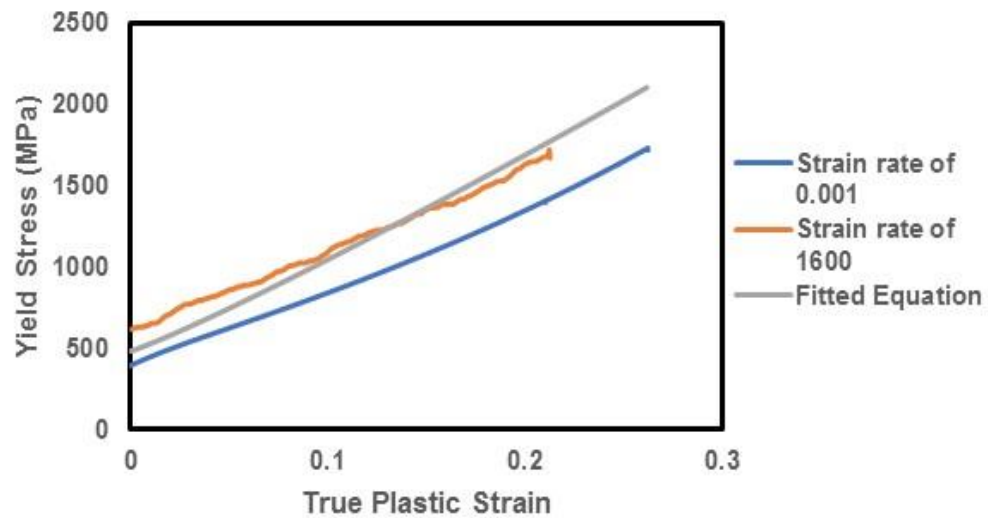


Figure 30 Johnson Cook model was fitted with the experiment results to reflect the strain rate effect and find the parameter C.

4.1.3.3 Thermal Softening

Temperature has significant effects on material mechanical behavior, increasing the temperature decreases the strength of the material. Fig.31 below shows the behavior of CoCrFeMnNi at different temperature and the same strain rate.

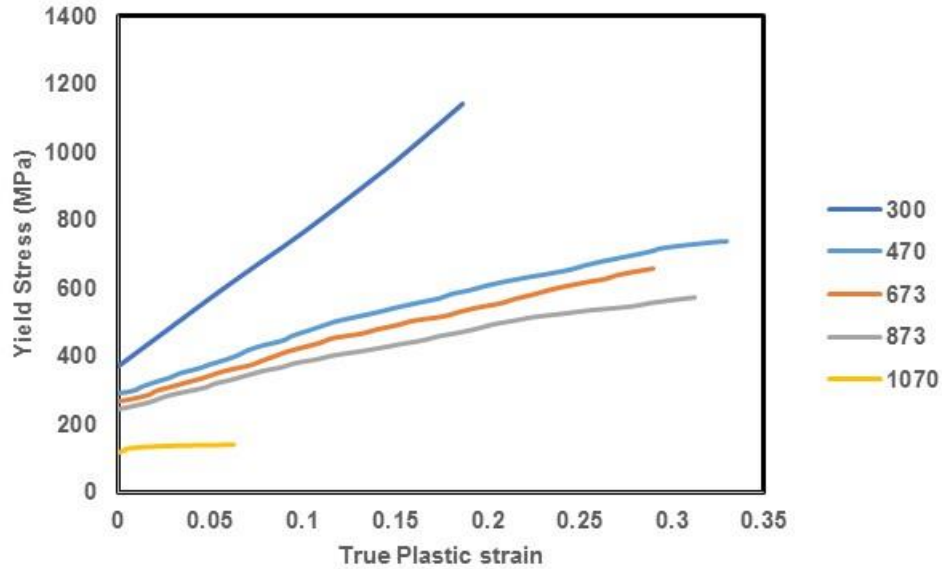


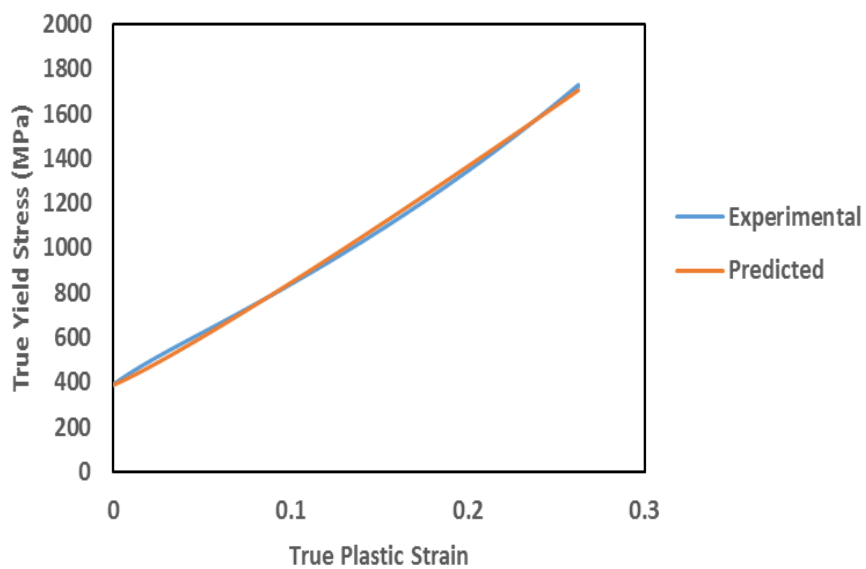
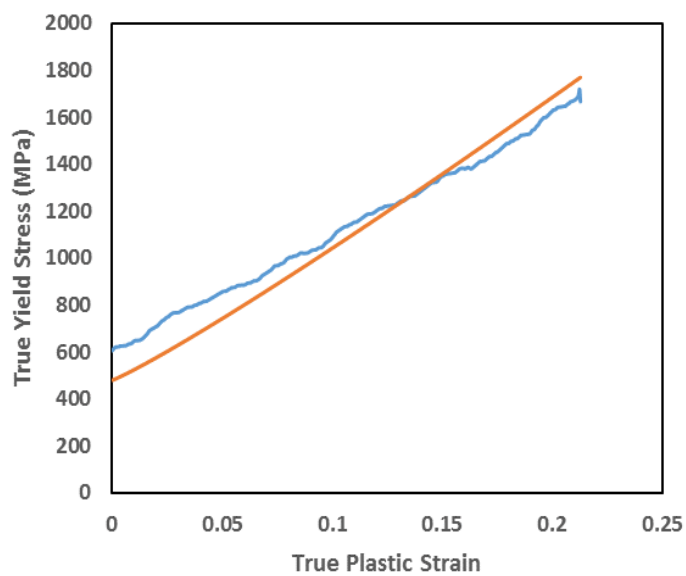
Figure 31 Temperature dependent True Stress vs true plastic strain at constant strain rate of CoCrFeMnNi [28]

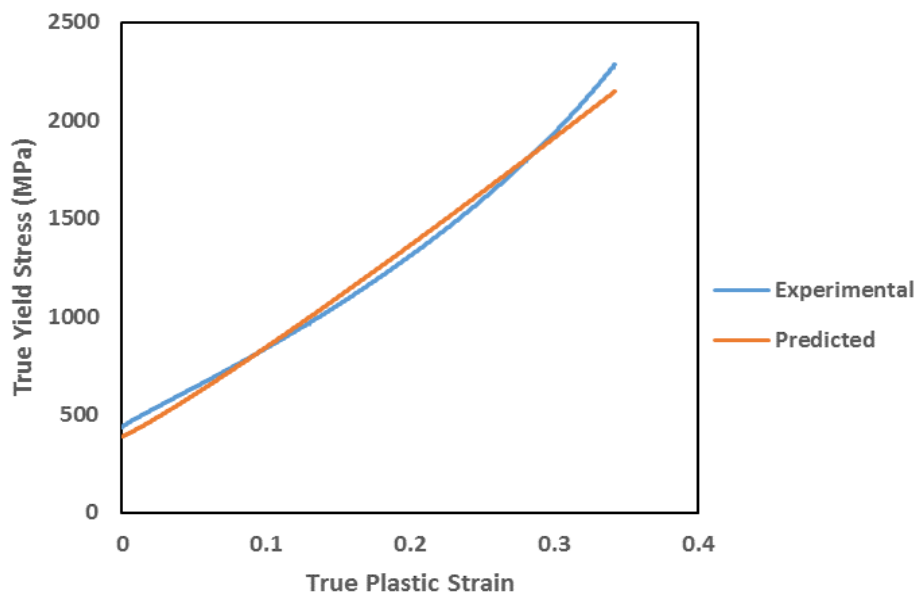
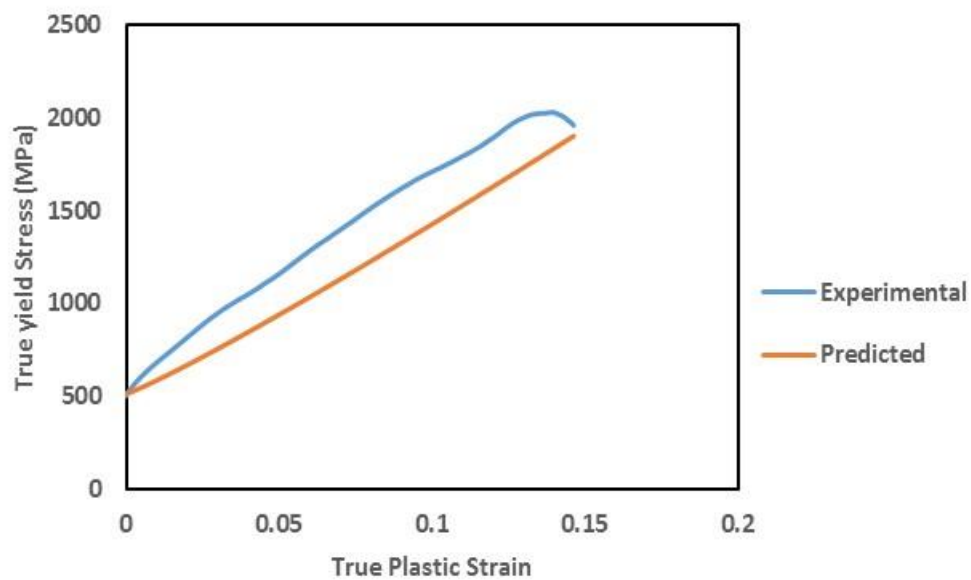
The thermal softening parameter was obtained by fitting the equation to the stress strain curve of CoCrFeMnNi

$$\sigma = (388 + 5729\varepsilon^{1.1})(1 - C \ln\left(\frac{\dot{\varepsilon}}{0.001}\right)) \left[\left[\left(1 - \frac{T - T_r}{T_{melting} - T_r}\right) \right]^m \right]$$

Below equation shows that all Johnson Cook model with all parameters have been obtained. Validation of this constitutive equation was obtained by comparison between the model prediction and experimental data. The predicted stress flow was achieved by applying the strain, strain rate and temperature of the experimental result into the Johnson cook model. Then, compared the obtained stress with experimental stress flow.

$$\sigma = (388 + 5729\varepsilon^{1.1})(1 - 0.00081 \ln\left(\frac{\dot{\varepsilon}}{0.001}\right)) \left[\left[\left(1 - \frac{T - T_r}{1600 - T_r}\right) \right]^{42.3} \right]$$

Figure 32 $\dot{\epsilon}=10^{-4} \text{ s}^{-1}$ at room temperatureFigure 33 $\dot{\epsilon} = 1600 \text{ s}^{-1}$ at room temperature

Figure 34 $\dot{\epsilon} = 10^{-4} \text{ s}^{-1}$ $T = 153\text{K}$ Figure 35 $\dot{\epsilon} = 3000 \text{ s}^{-1}$ $T = 153\text{K}$

4.2 Microstructure

4.2.1 Chemical Composition

CoCrFeMnNi was prepared and supplied by B. Wang, manufacturing process detailed in 3.1. Chemical composition is presented in Table.4. The analysis shows that CoCrFeMnNi was almost manufactured by five equally proportions of Cr, Mn, Fe, Co and Ni. These five elements have similar atomic weight as shown in Fig.36.

Table 4 Chemical Composition

Element	Cr	Mn	Fe	Co	Ni
Weight %	20.27	19.95	20.27	20.05	19.47

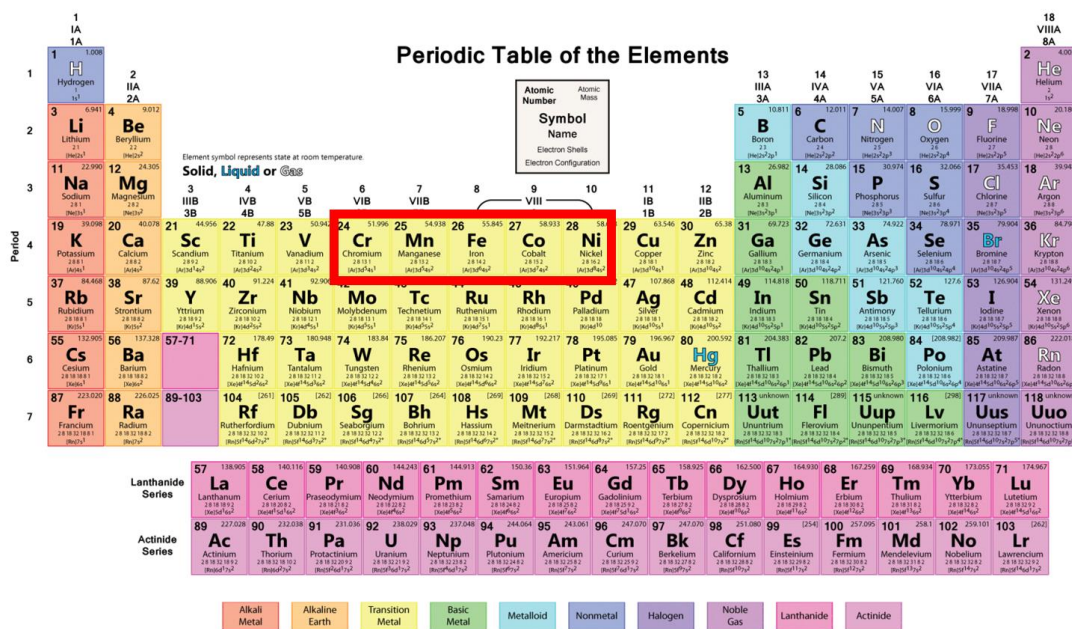


Figure 36 CoCrFeMnNi has similar atomic weights

In addition, note that all the elements of CoCrFeMnNi are transition metals and they have similar electronegativity. Electronegativity is a chemical property that predict the

atoms ability to attract electron and form chemical bonding. Table 5 shows the electronegativity of the pure elements which are very similar.

Table 5 Electronegativity of pure elements

Element	Electronegativity
Co	1.88
Cr	1.66
Fe	1.83
Mn	1.55
Ni	1.91

4.2.2 Elemental Analysis by EDX

Energy-dispersive X-ray spectroscopy (EDX) was performed on the received samples as shown in Fig.37. Elemental planar scan of CoCrFeMnNi shows homogenous distribution of the element across the examined specimen as shown in Fig.38. It also illustrates that spark plasma sintering manufacturing was successful to produce CoCrFeMnNi.

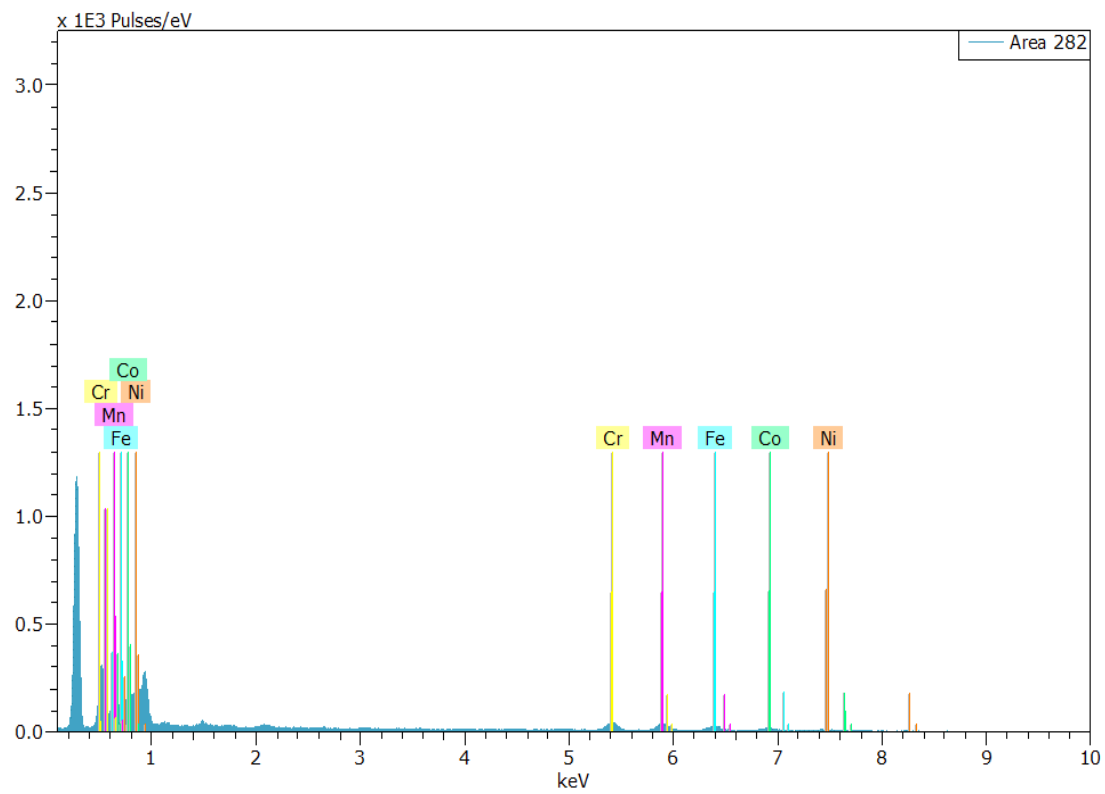


Figure 37 EDX spectrum of CoCrFeMnNi

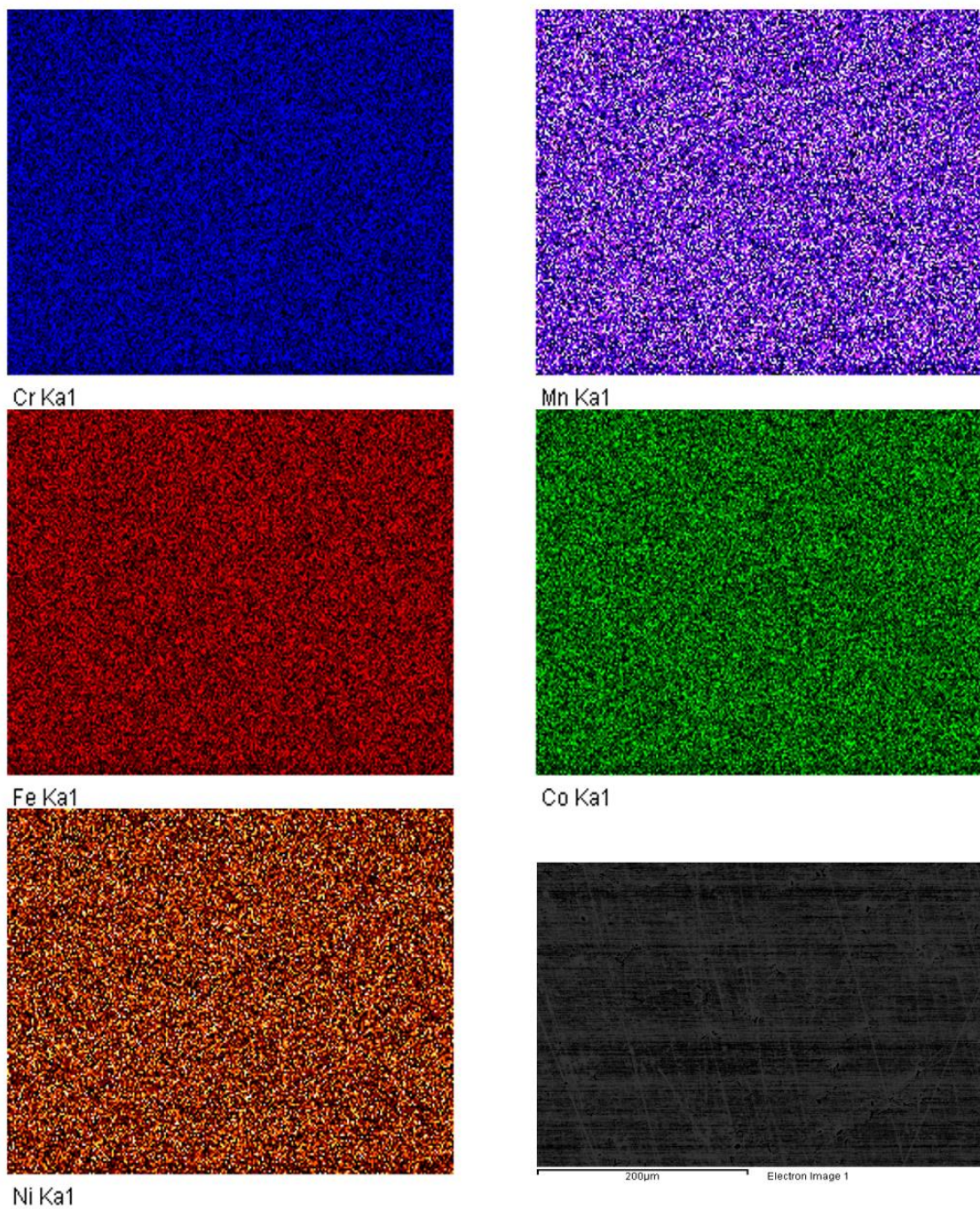


Figure 38 Elemental planar scan of the CoCrFeMnNi high entropy alloy

4.2.3 Microstructural Characterization

Electron back scatter diffraction (EBSD) was conducted on unreformed specimen illustrated in Fig.39 EBSD map also reveals some annealing twins. The grains are polygonal and the grain sizes were measured based on the longest side of the grain. Fig.40 shows the grain sizes distribution based on selected area of the specimen.

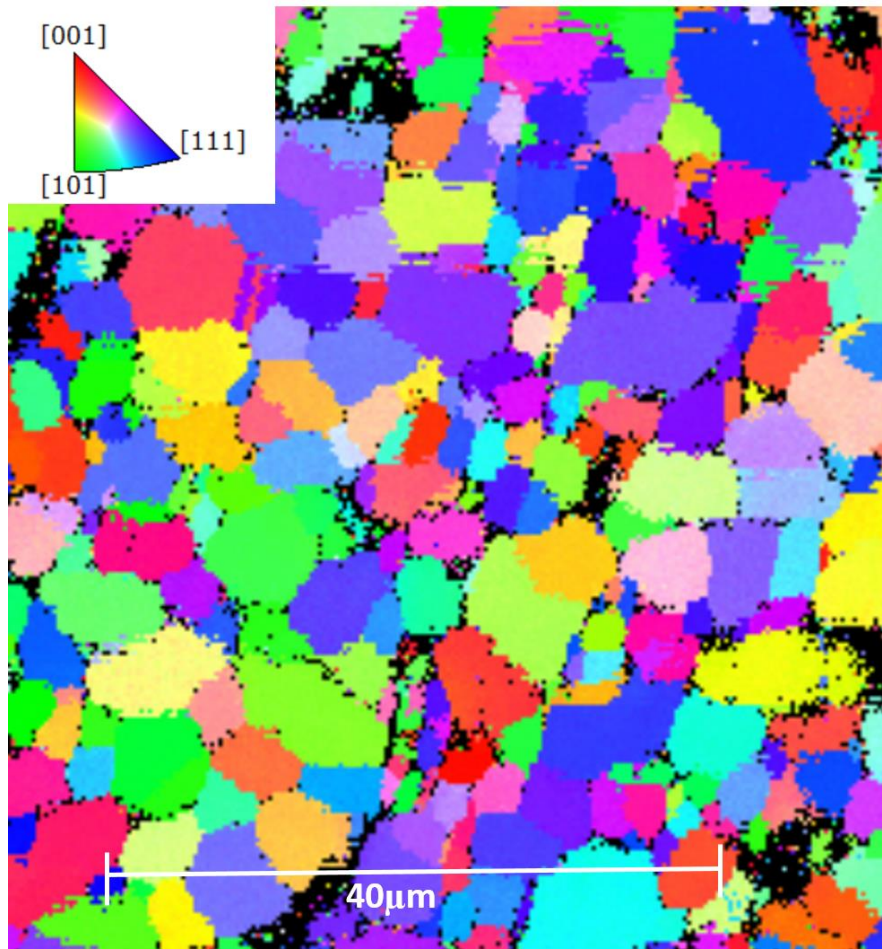


Figure 39 EBSD of unreformed CoCrFeMnNi

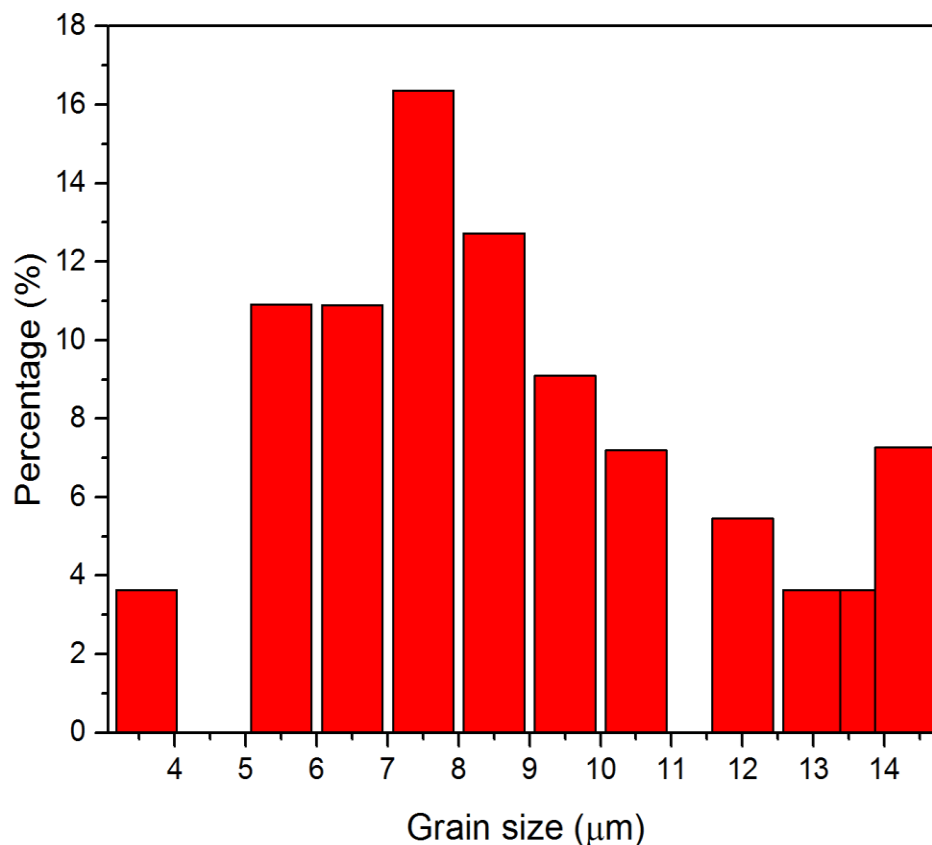


Figure 40 Grain sizes measurement of unreformed CoCrFeMnNi.

4.2.4 X-ray powder diffraction (XRD)

XRD is used for phase identification for crystalline materials. A 5x5mm specimen was prepared for XRD pattern examination. CoCrFeMnNi is composed with elements that are different in crystal structure. Ni is FCC, Fe and Cr is BCC, Co is hexagonal closed packed (HCP) and Mn has its own crystal structure called alpha manganese(A12).

However, by examining the crystallographic structure of this alloy, it has identified as face centered cubic (FCC). This is one of the features of high entropy alloys, which many elements of different crystal structures form an alloy of a simple crystal structure. Fig.41 below shows the XRD pattern measured for this high entropy alloy.

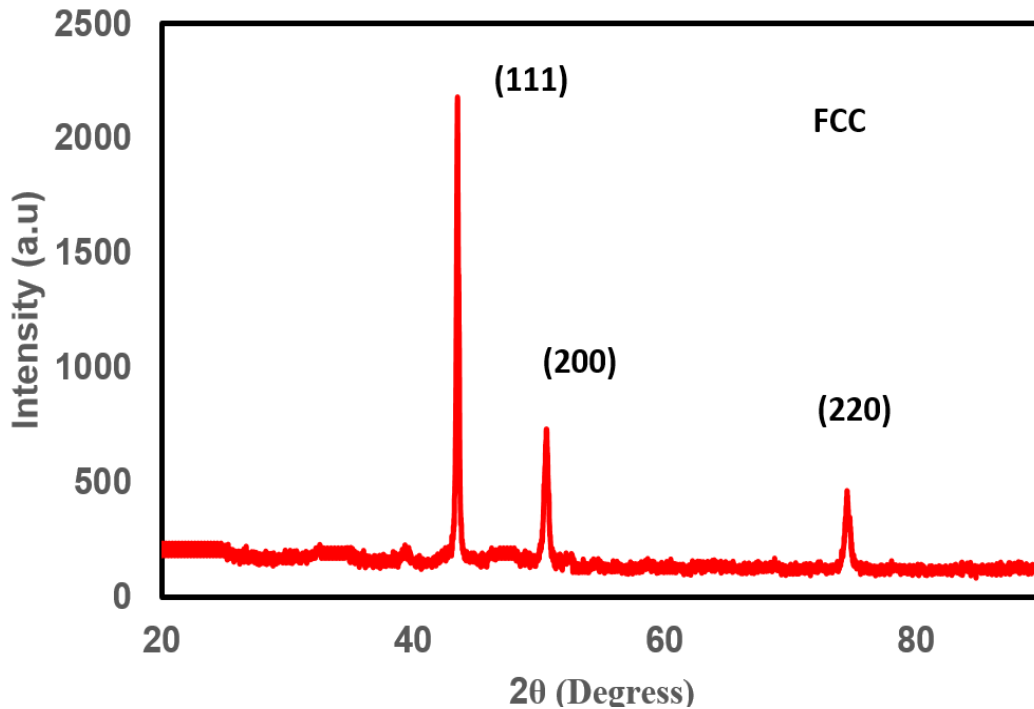


Figure 41 XRD pattern of CoCrFeMnNi.

4.2.5 Adiabatic Shear Band Evolution

The hat shape specimens, described in section 3.1, was used to study adiabatic shear band evolution in CoCrFeMnNi. The microstructure was characterized by optical microscopy, EBSD and TEM. The specimens were cut in direction parallel to the shear direction. Fig.42-45 below show optical microscope of the four deformed specimens. It is well observed in these optical images the existence of shear band. However, optical microscope show usually wider shear band than actually it is. Therefore, it need further examination of the shear band by SEM.

The hat shape specimen experience very high strain rates greater than 10^3 s^{-1} which results in extremely fast deformation process. For strain rate that exceeds 10 s^{-1} , no heat exchange between the metal and the surrounding and adiabatic condition is assumed. Below Fig.42 shows the shear stress strain for hat shape specimen at 153K, it

represents also typical shear stress strain behavior of this material. The plastic deformation starts at shear stress of around 250 MPa then the material starts to show strain hardening. Then, a maximum shear stress is reached and the material lost its stability due to thermal softening leading to the collapse of the material. Fig.43 shows the shear stress strain for hat shape specimen at 300K.

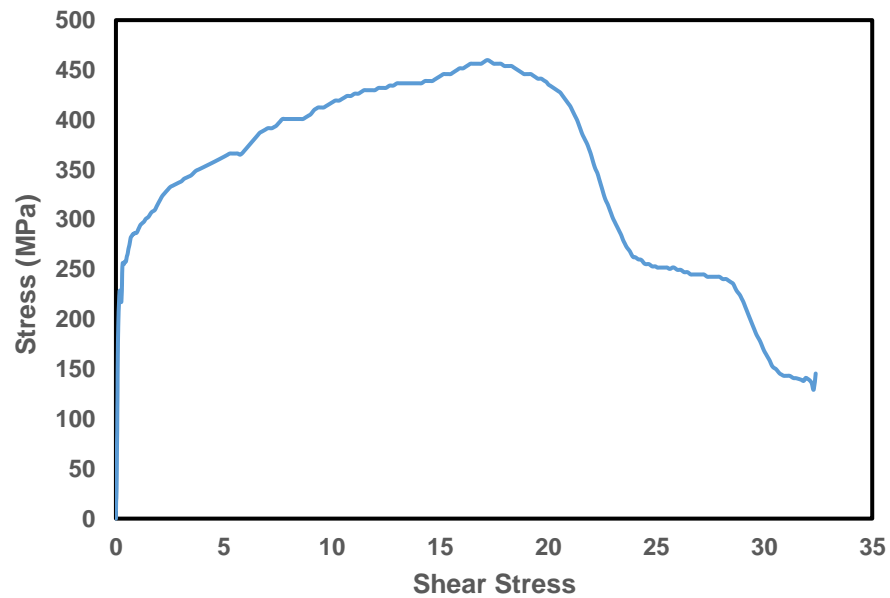


Figure 42 Shear Stress-Strain of the hat shape specimen at 153 K.

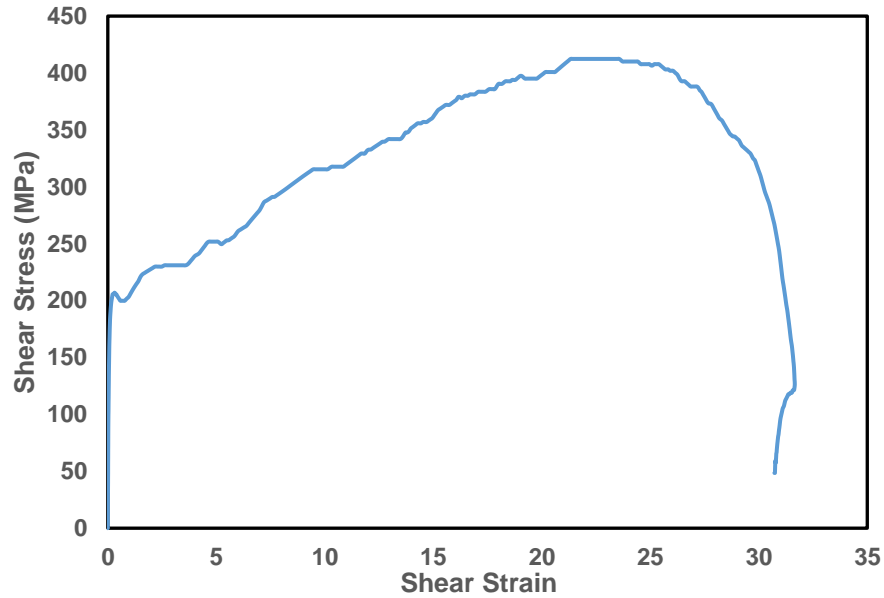


Figure 43 Shear Stress-Strain of the hat shape specimen at room temperature 300 K.

The total deformation time was between 180 to 200 μ s. In addition, the short deformation time and the localization of plastic deformation at the narrowed area limit the heat conduction to other areas of the sample which results in significant temperature rise. Hence, due to the short time and plastic deformation localization, this deformation is considered adiabatic within the sample. The temperature rise results in thermal softening of the material that weakens the bonding between grains. Below relationship illustrates the temperature rise. The plastic work is per unit volume equal to the area under the plastic stress strain curve.

$$\nabla T(\varepsilon_p) = \frac{\beta}{\rho C_p} \int_0^{\varepsilon_{pMax}} \sigma_p d\varepsilon_p$$

Where

σ_p is the yield stress

ε_p is plastic strain.

β is the fraction of plastic energy converted into heat, usually considered 0.9 for metals.

C_v is the heat capacity. 430 J/Kg K [17].

ρ is is the density. 8042 Kg/m³.

Fig.44 & 45 Below illustrate the temperature rise in the shear band. The temperature rise is between $0.3T_m$ and $0.5 T_m$ which indicates the dynamic recrystallization.

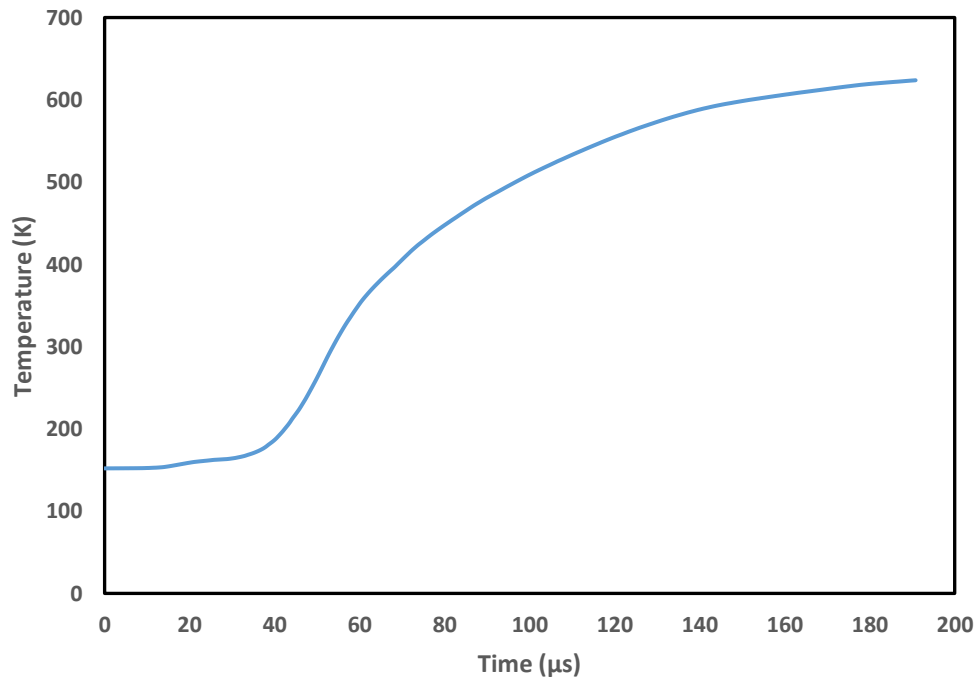


Figure 44 Temperature rise in hat-shape specimen tested at 153K

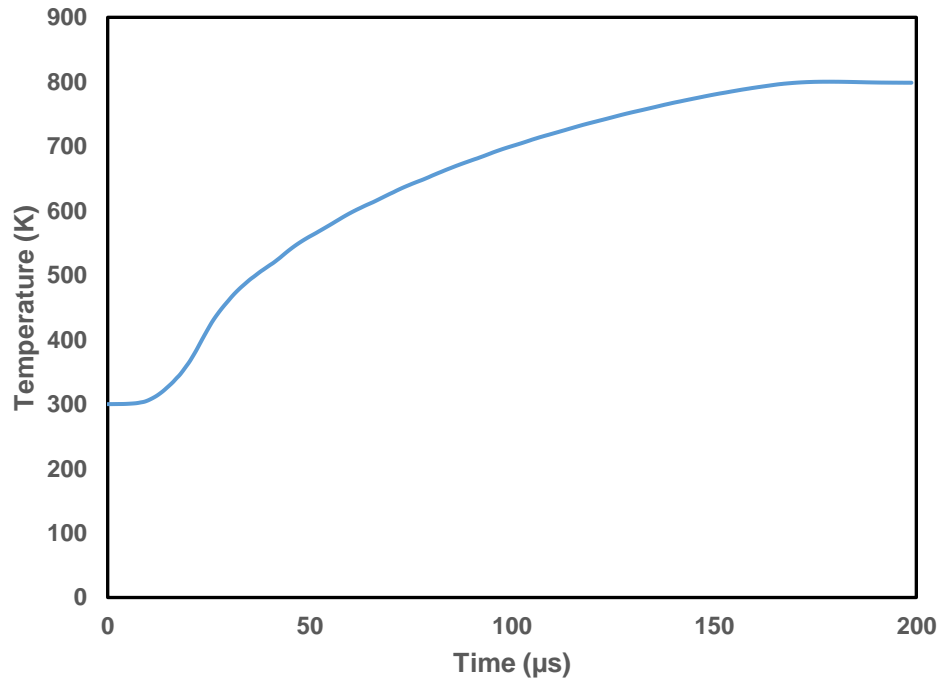


Figure 45 Temperature rise in hat-shape specimen tested at room temperature (300K)

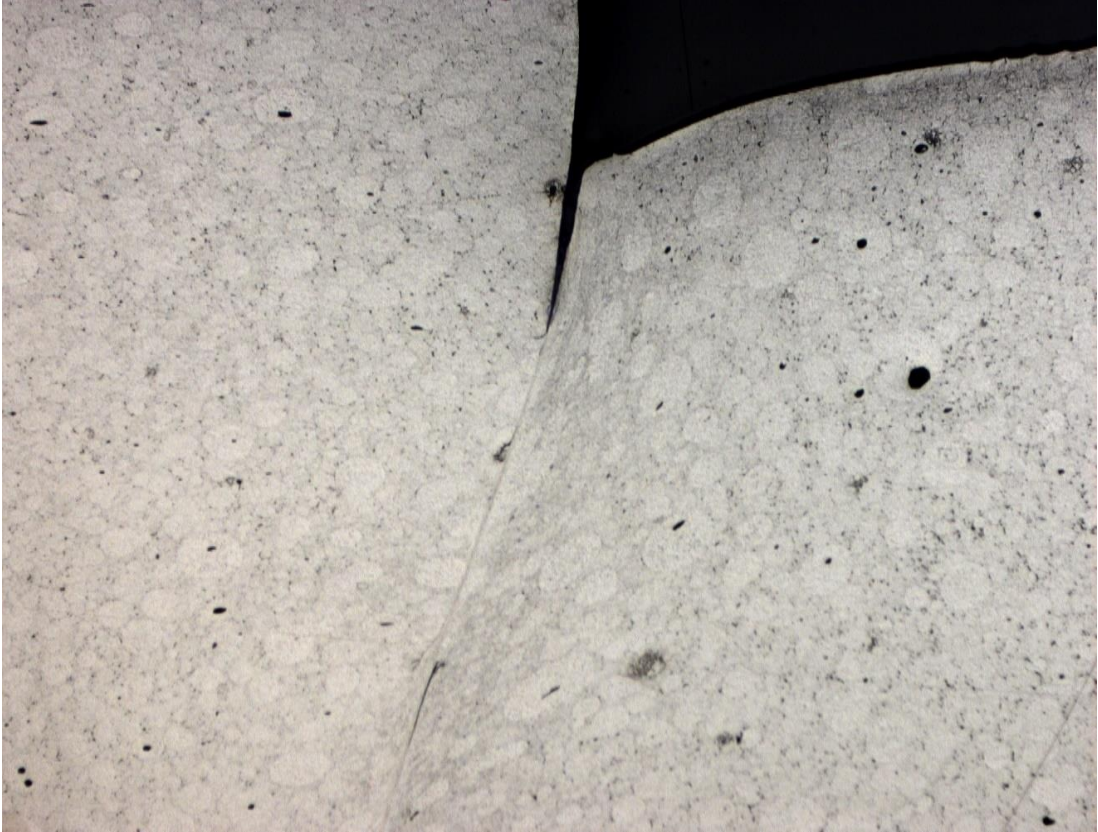


Figure 46 Specimen at room temperature (N1)

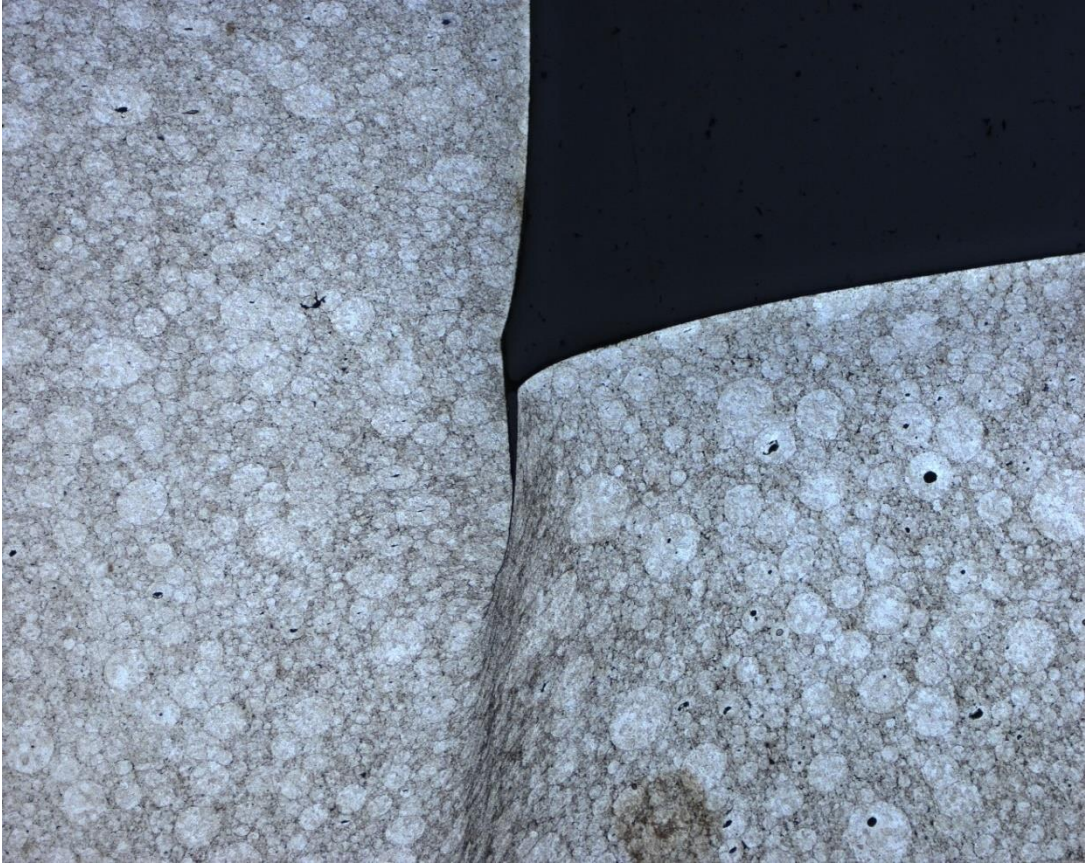


Figure 47 Specimen at room temperature (N2)



Figure 48 Specimen at low temperature (C1)



Figure 49 Specimen at low temperature (C2)

4.2.6 Microstructure inside the adiabatic shear band

TEM was used to have better insight into the microstructure of the adiabatic shear band for a specimen at room temperature and another specimen at 153K. Specimens were prepared by FIB from both specimens.

4.2.6.1 At Low Temperature (153K)

Fig.50 shows an overview of the microstructure of specimen at 153K, the grains are elongate equiaxed. Fig.51 shows a closer look into these equiaxed grains.

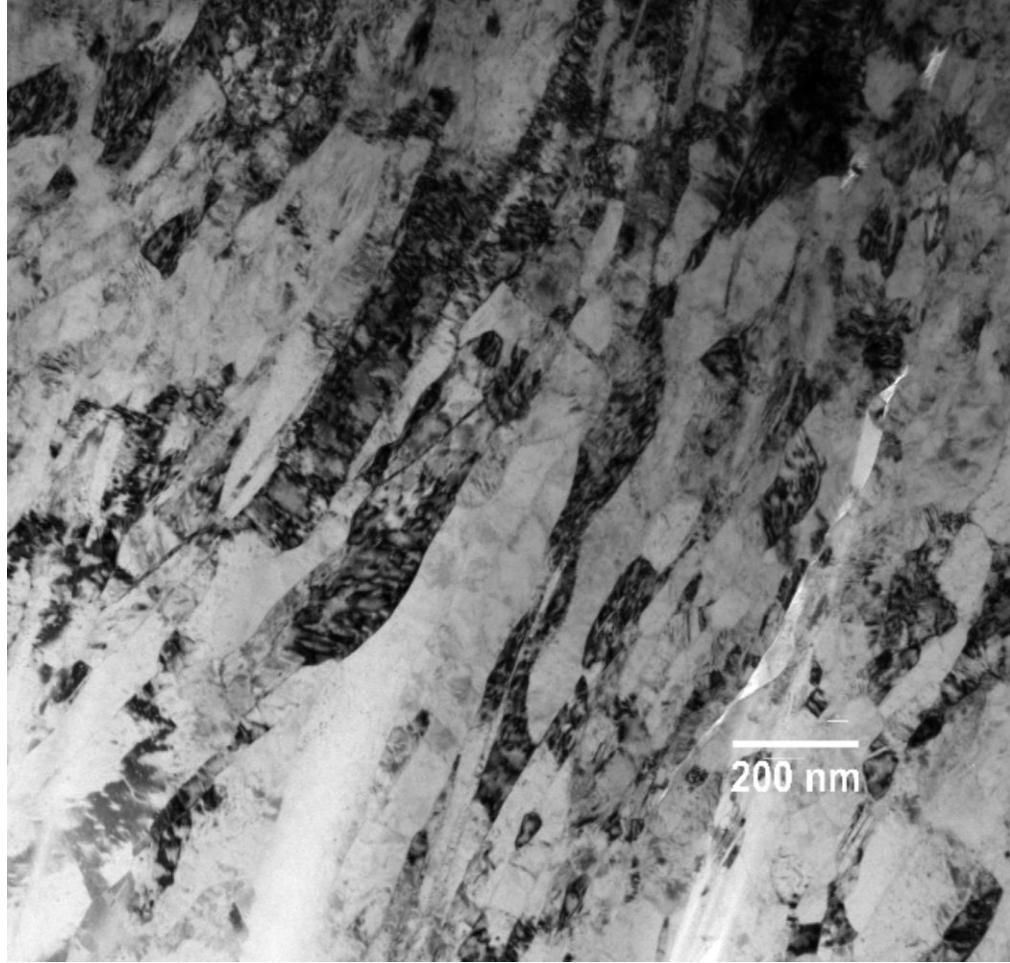


Figure 50 TEM image of shear band microstructure



Figure 51 Higher magnification of TEM image of the microstructure.

It is obvious from these TEM images that the material inside the adiabatic shear band went through significant grain refinement. Grain sizes were measured inside a representative area inside the shear band as shown in Fig.52. 50% of the grains are less than 100nm while the rest is less than 200nm.

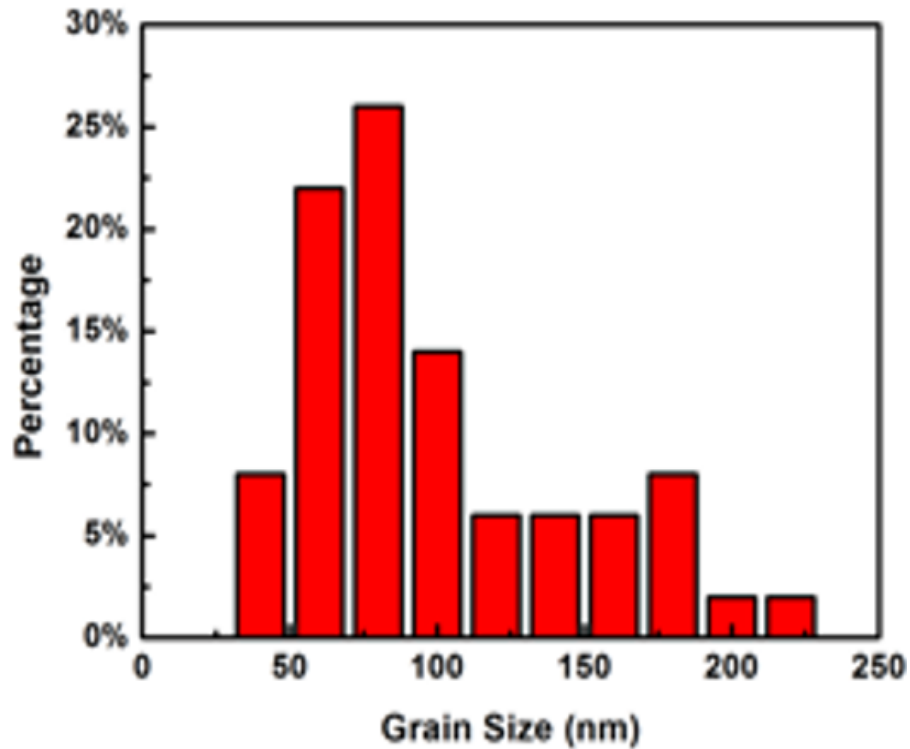


Figure 52 Grain size distribution inside the shear band.

In addition, deformation nanotwins were observed inside the adiabatic shear band. These deformation nanotwins worked as a refinement mechanism to refine the grains by generating additional twin boundaries and hence form elongated nanograins. Fig.53 and Fig.54 below shows how nanotwins has generated elongated nanograins and hence refining the grains inside the adiabatic shear band.

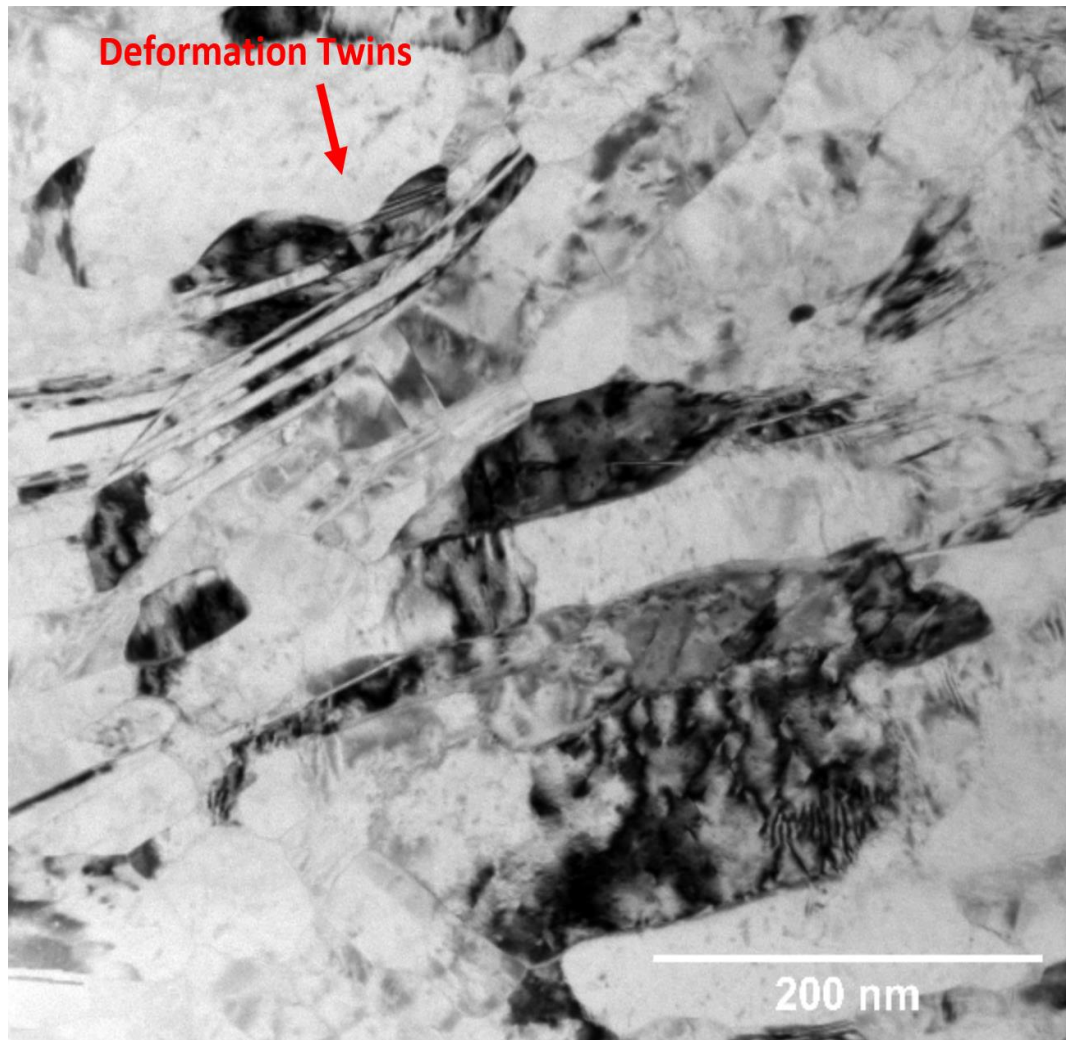


Figure 53 Deformation nanotwins worked as refinement mechanism and generated additional elongated nanograins.

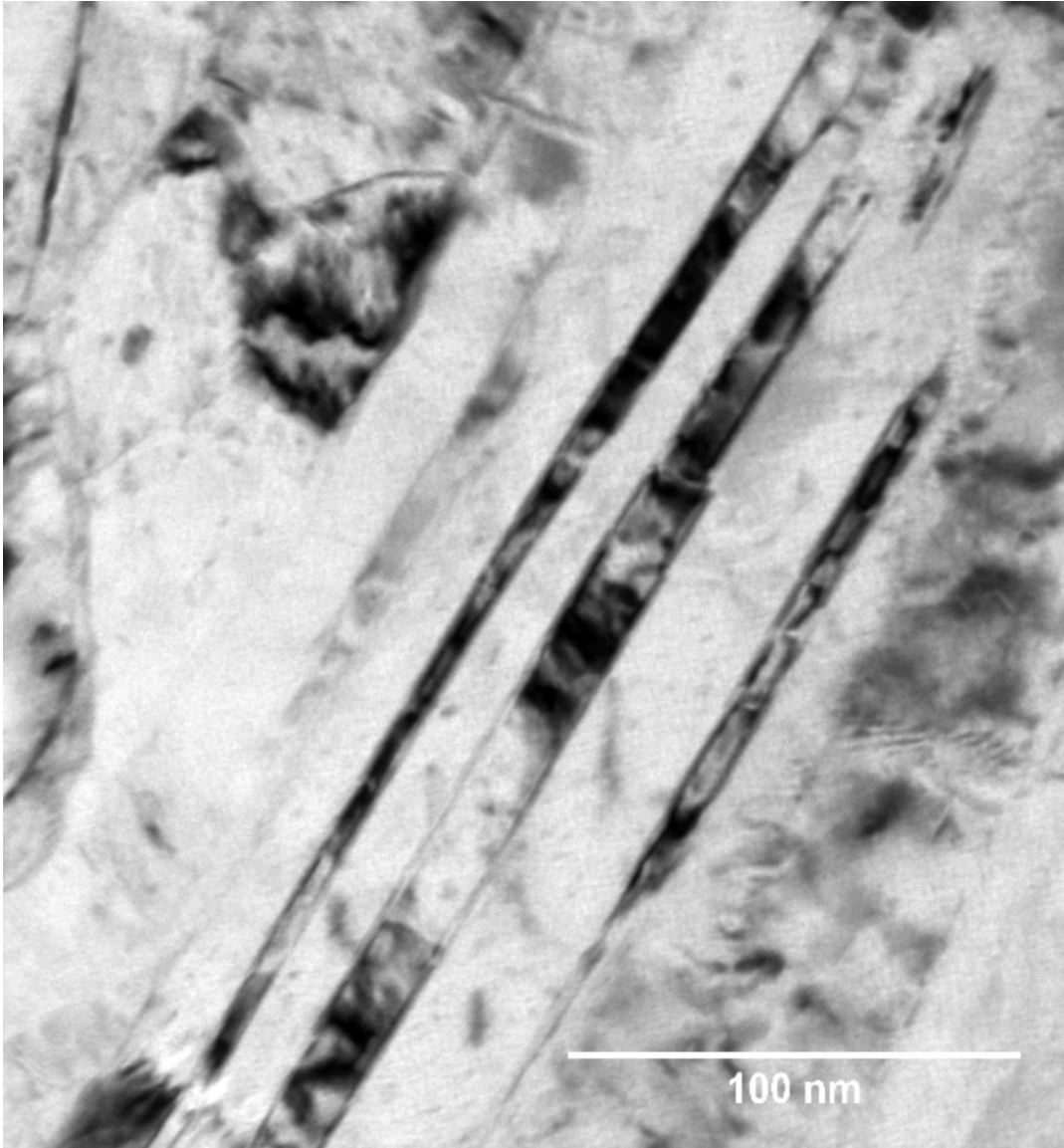


Figure 54 A higher magnification of TEM image that shows nanotwins forming elongated nanograins.
At Room Temperature (300K)

Fig. 55 below shows an overview TEM image inside the shear band. The grains are equiaxed and similar to grains of low temperature specimen, however, the grain sizes are substantially differed. The grains inside the shear band of the room temperature specimen is all ultrafine grains with 70% of them have average sizes between 250nm to 350nm. Fig. 56 shows the grain sizes distribution. In addition, deformation twins were much dense at this specimen compared to low temperature specimen.

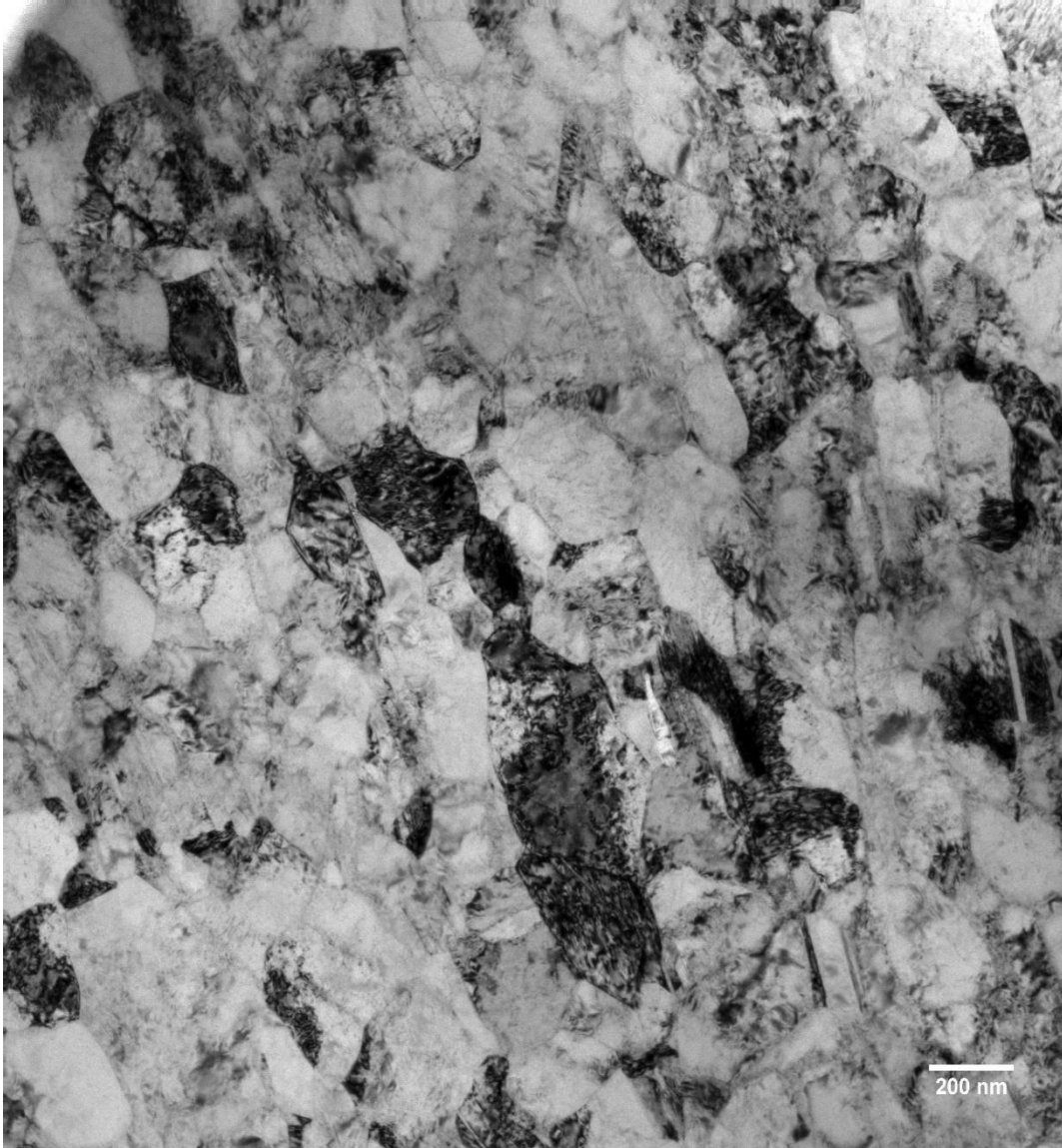


Figure 55 An overview of microstructure inside the shear band.

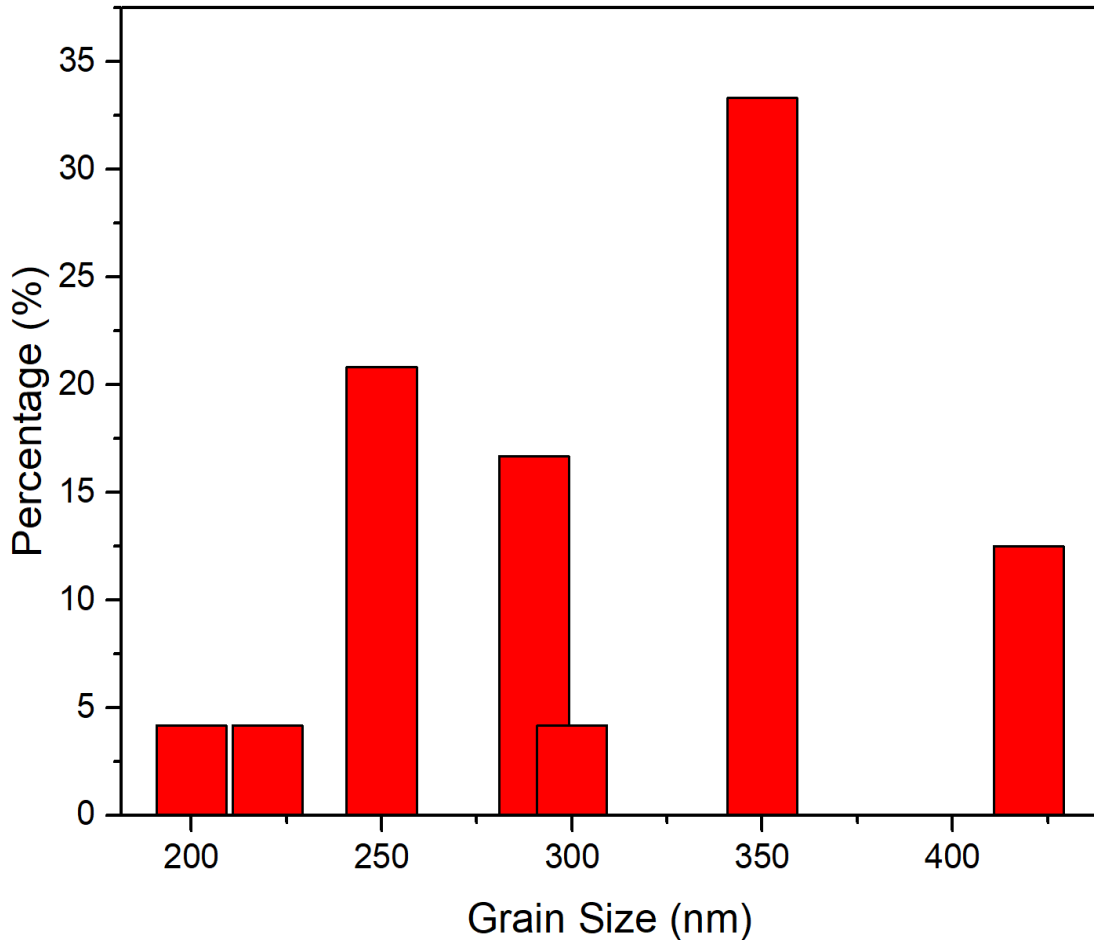


Figure 56 grain sizes distribution for specimen at room temperature (300K)

4.2.6.2 Comparison and Mechanism of Grains Refinement for The Two Specimens

As the shown in this section of the report, the microstructure inside the shear band was extremely refined. Most grains were refined to ultrafine grains in the room temperature specimen while nanograin in the room temperature. The difference in this refinement is believed to be due to increase in deformation twins for the specimen testes at low temperature.

The mechanism of refinement seems to be a dual mechanism, rotational dynamic recrystallization and deformation twinning. The dynamic recrystallization inside the adiabatic shear band in metal and metal alloys were described in different names;

rotational dynamic recrystallization by Derby [18], formation of geometry necessary boundaries by Hughes [19] and continuous recrystallization by Humphreys [27]. However, rotational dynamic recrystallization will be used throughout this report. In the following paragraphs, the sequence of material deformation and microstructural changes will be illustrated.

At the start of deformation, the dislocation density increases. These dislocations are randomly distributed as shown in Fig.53. Then, these dislocations start to accumulate to form cells of dislocations. The accumulated dislocations cells elongate as the plastic deformation increases. The dislocation cells elongate more and forms elongated subgrains as shown in Fig.54. As deformation continues, the elongation decreases the width of these subgrains, then they collapsed vertically as shown in Fig.55. The collapse and formation of vertical dislocation in the elongated cells was to decrease the overall strain energy as shown by Meyers et al in 2000 [21]. This collapse of these cells results in subgrain structures in the middle of the shear band. The collapse of the cells is represented by dislocation pile up in these cells. Dislocation pile up was observed in this material as shown in TEM image in Fig. 56. These subgrains rotates during the recrystallizations to form equiaxed nanograins as shown in Fig.58. In addition, some nanograins experienced further refinement by nanotwinning that refine the nanograins to much smaller elongated nanograins. These nanograins have the length of 0.05-0.2 μm .

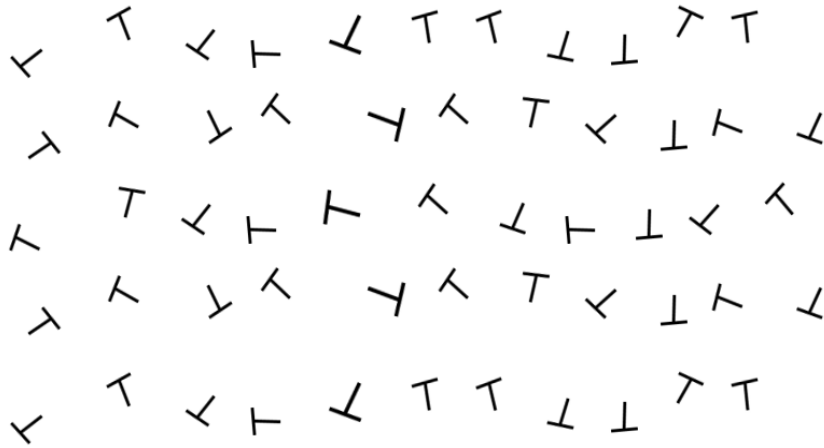


Figure 57 Random distribution of dislocation at the start of plastic deformation.

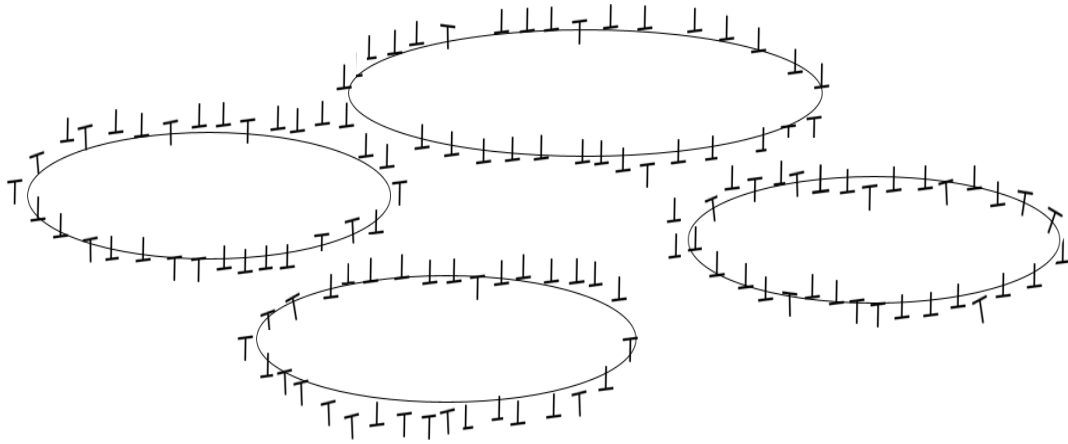


Figure 58 Elongated dislocation cells forms elongated subgrain structures

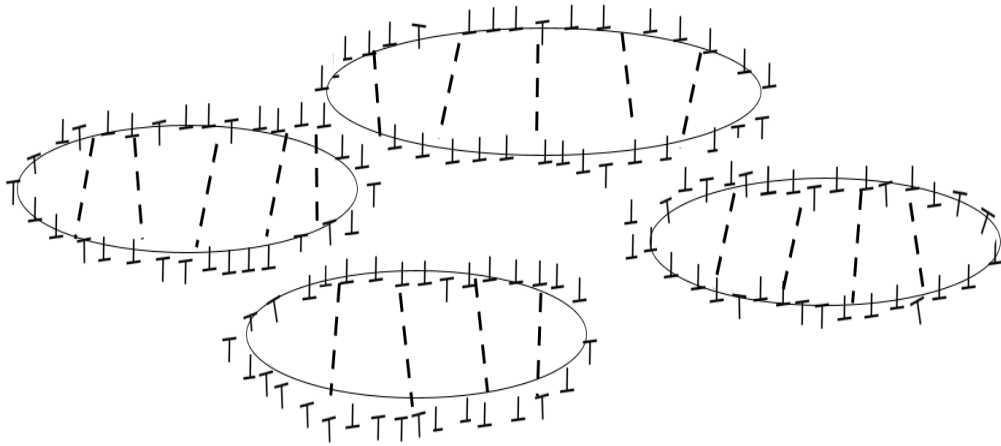


Figure 59 Breakup of elongated subgrains

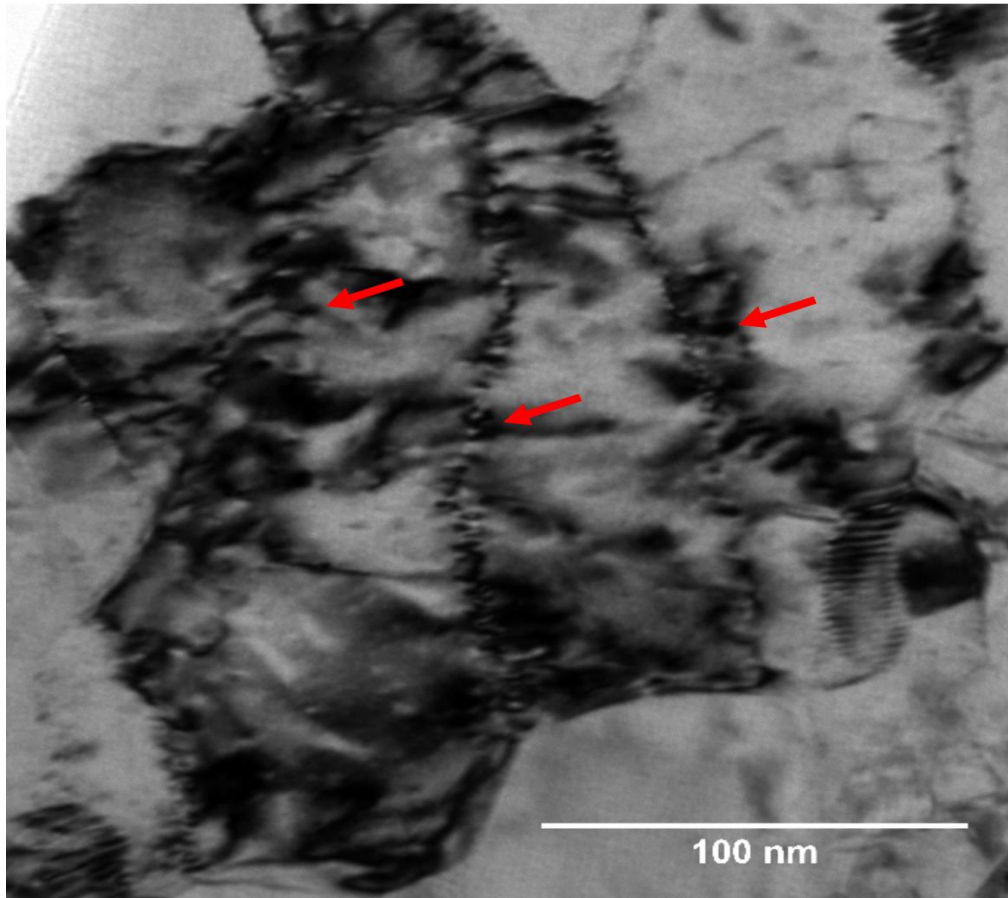


Figure 60 TEM bright field image of dislocation pile-up inside the subgrains.

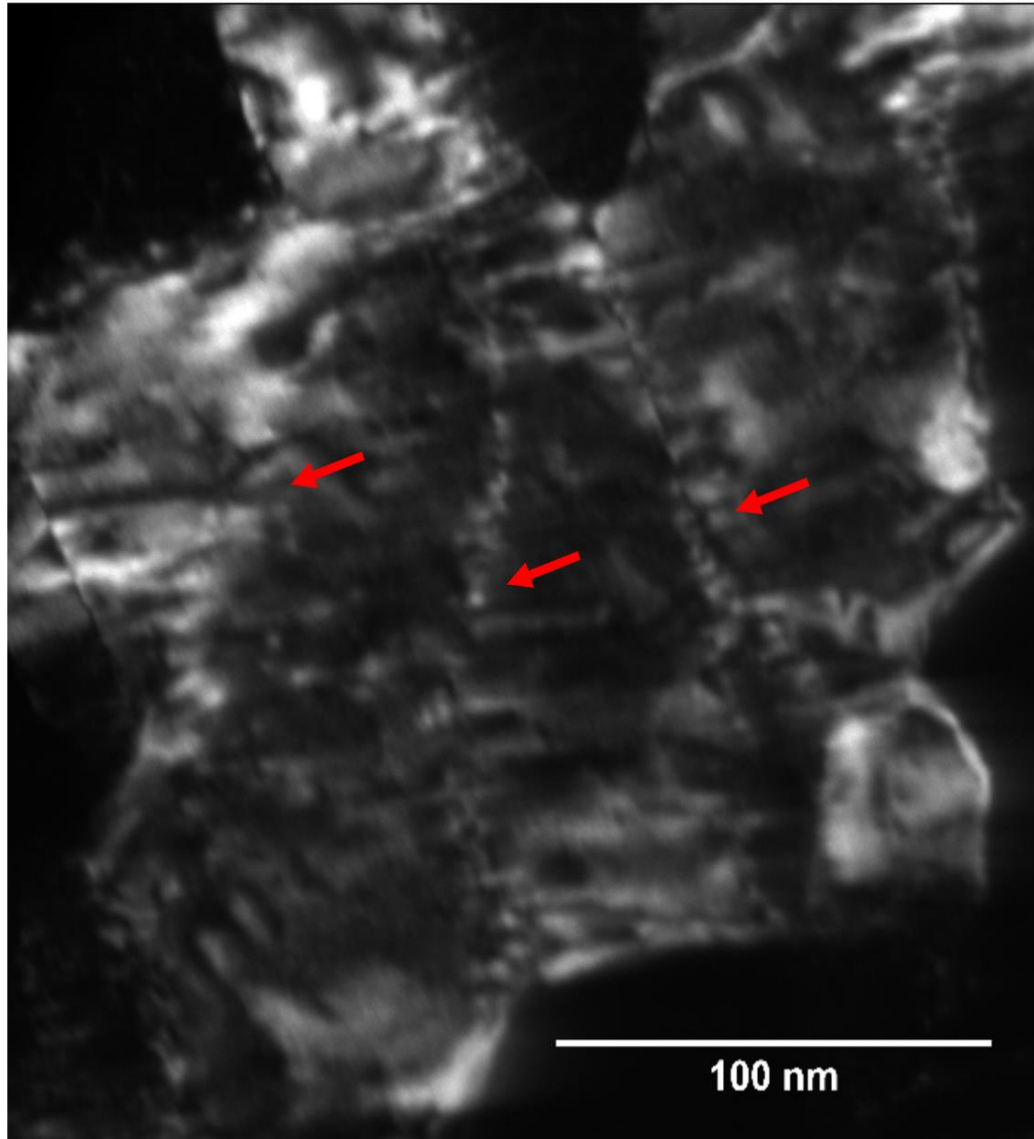


Figure 61 Dark field TEM image of the same subgrain in Fig56 showing the dislocation arrangement in the subgrains.

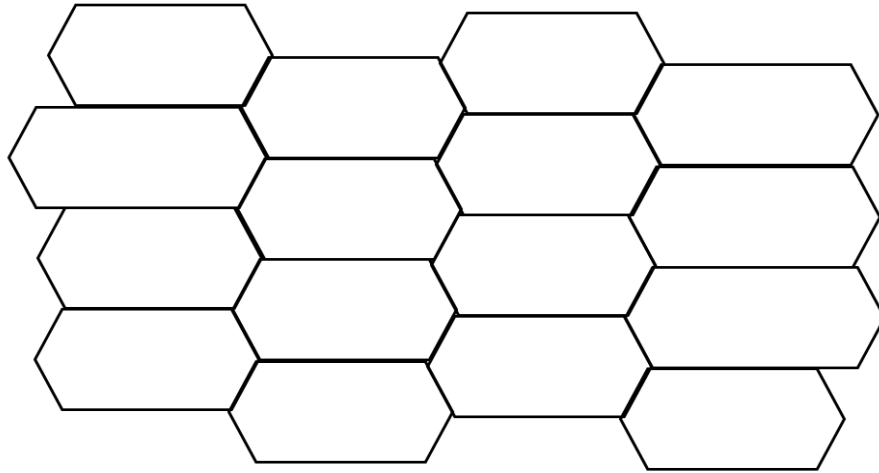


Figure 62 Ultrafine equiaxed grains

4.2.7 Microhardness

The microhardness was measured in the shear band and outside the shear band. This was carried out to examine the hardness of the resulted refined structure. The microhardness measurement shows that CoCrFeMnNi high entropy alloy exhibit better hardness compared with 316L austenitic stainless steel as shown in Fig.59. A high hardness of 510 HV can be achieved for ~ 100 nm CoCrFeMnNi HEA, showing a superior hardness property while only a hardness of 480 HV can be achieved for ~ 40 nm 316L austenitic stainless steel.

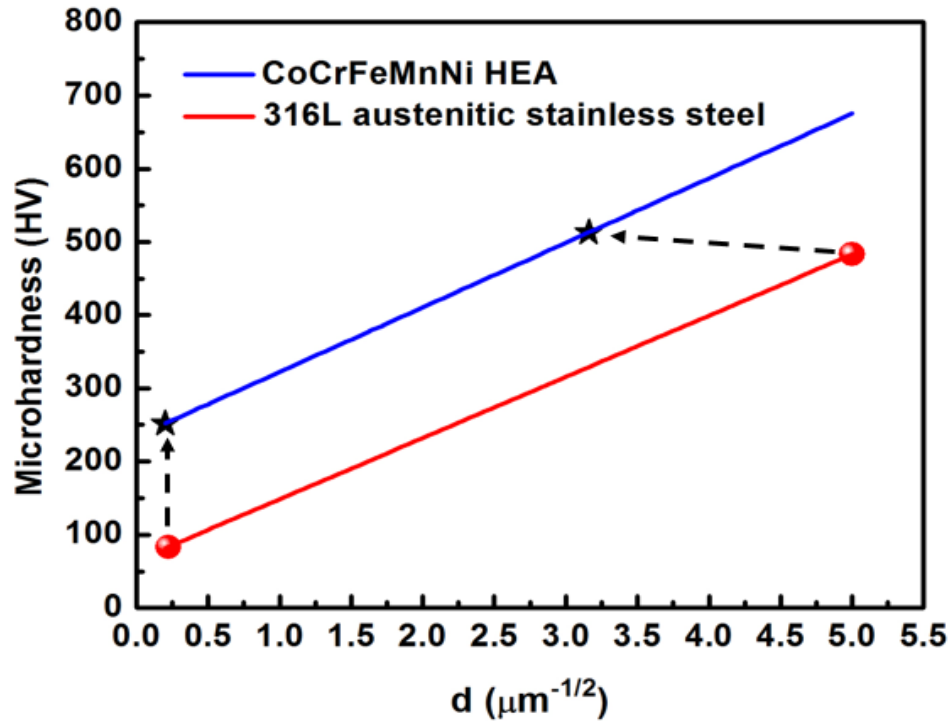


Figure 63 Microhardness measurement of this high entropy alloy in comparison with 316L austenitic stainless steel.

4.3 Finite Element Simulation

The aim of this section is to demonstrate finite element simulation results of CoCrFeMnNi high entropy alloy's hat shape specimen that was examined by Hopkinson bar at strain rate of 2500 s^{-1} . Also, the simulation was carried out to include the CoCrFeMnNi cylindrical samples at the same strain rate. These samples were assumed to undergo adiabatic heating because of high plastic work in a short time; hence, the simulation needs to be an adiabatic process. Therefore, finite element program, Abaqus/explicit, was used to facilitate the simulation of these tests. Explicit is one of Abaqus sub-programming tools that predict the response of dynamic behavior that are characterized by high strain rate and short time. In addition, many trial simulations were conducted to reach an appropriate element type that best fit this problem [22]-[2].

4.3.1 Numerical Model

4.3.1.1 Hat Shape Specimen Model

To reduce the computational cost, the hat shape specimen was modeled as 2-D axisymmetric model since the sample satisfy the axially symmetric loading conditions in respect to the Y-axis. Very fine mesh was used in the shear band region of 10 μ m so the shear band localization could easily be captured. However, other areas were meshed with relatively larger mesh between 40-70 μ m. The total elements in the model were 132,328 of element type CAX3 (A 3-node linear axisymmetric triangle). Fig.60 and Fig.61 show the mesh design of the hat shape specimen. Due to large number of elements, parallelization and multi processors were used and sufficiently reduced the simulation run time from 14 hours to 9 hours. The multiprocessing mode was Threads since other mode are not possible in the computer lab [39]-[42].

Based on several trials, it was evident that shear band region's mesh needs to be significantly less than the shear band width to form the shear band in finite element simulation. In addition, to achieve adiabatic analysis, the elements size needs to satisfy the below sizing condition. Both conditions were satisfied by the current mesh seeding sizes.

$$t_{total} \leq \frac{pc}{6K} \Delta L^2$$

Where,

t_{total} =Simulation time

p = Material Density, C =specific heat, K = Thermal Conductivity,

ΔL = element size in the shear band zone

This sizing will ensure that the mesh is small enough that prevent heat transfer between the elements (Abaqus Manual 16.4)

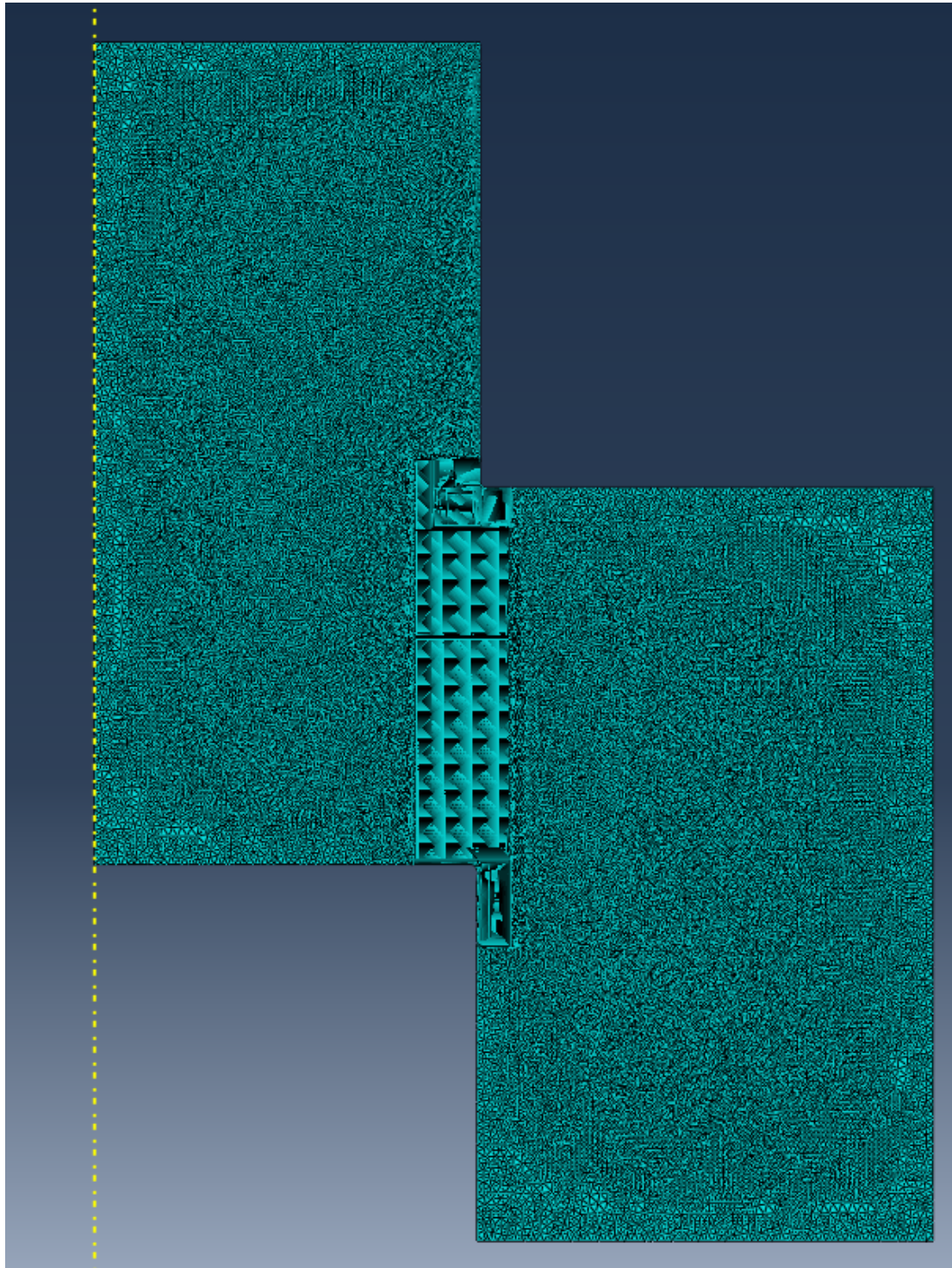


Figure 64 Axisymmetric model of the hat shape specimen

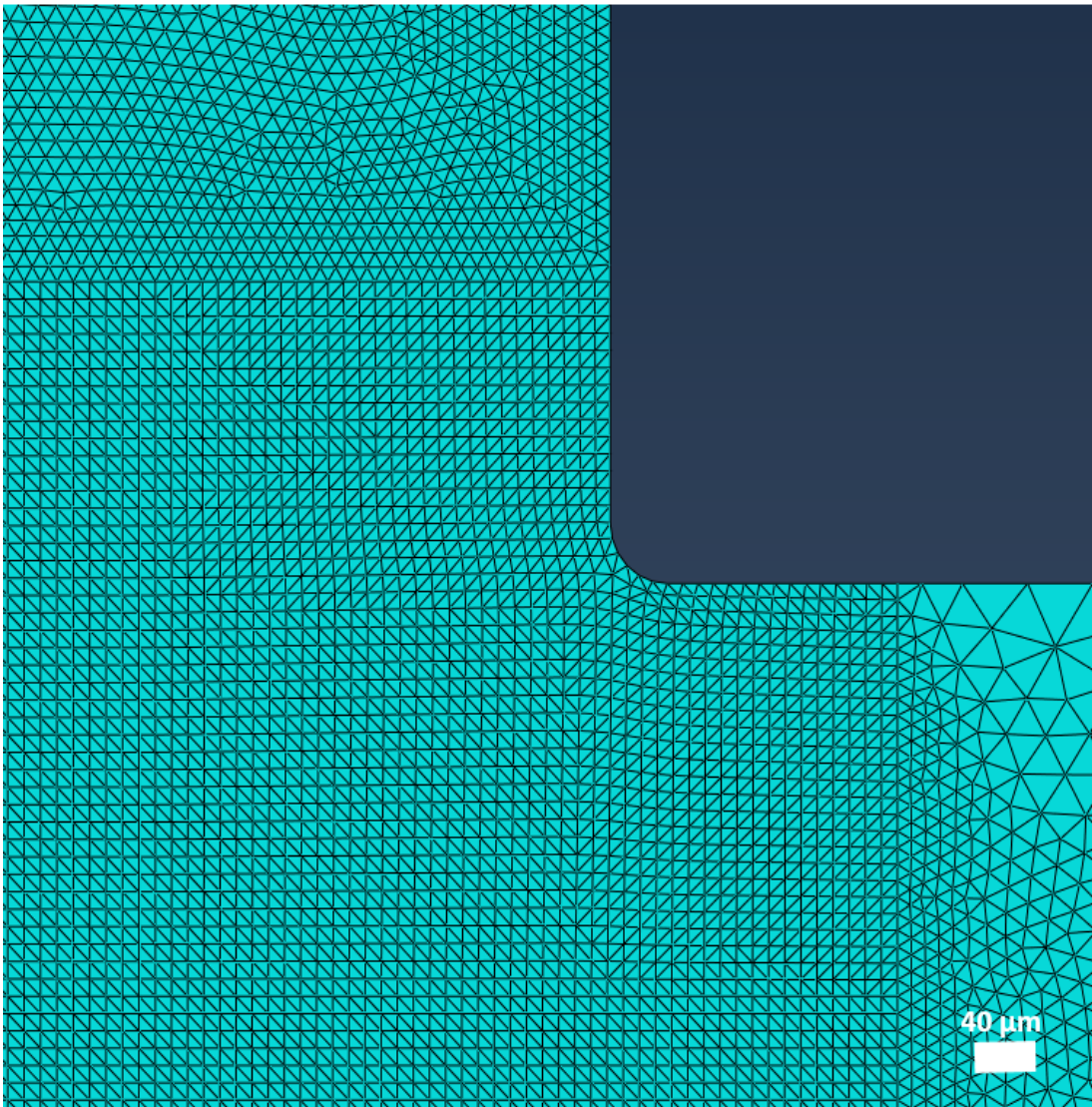


Figure 65 A zoom into the external corner shows the structured and fine mesh size in the designed shear band zone.

4.3.1.2 Cylindrical specimen

The cylinder was modeled with actual dimensions and was fixed at the bottom while load was applied on the top of the model. The sample was meshed by 29,852 elements of a 10-node modified quadratic tetrahedron. The model is a 3D model of the cylindrical sample and the element size was 120 μm . Two identical plates were modeled to apply

the load on the top and bottom of the sample. These plates were modelled as elastic material only and not allowed to deform. The load was in terms of applied displacement of the two plates on the sample.

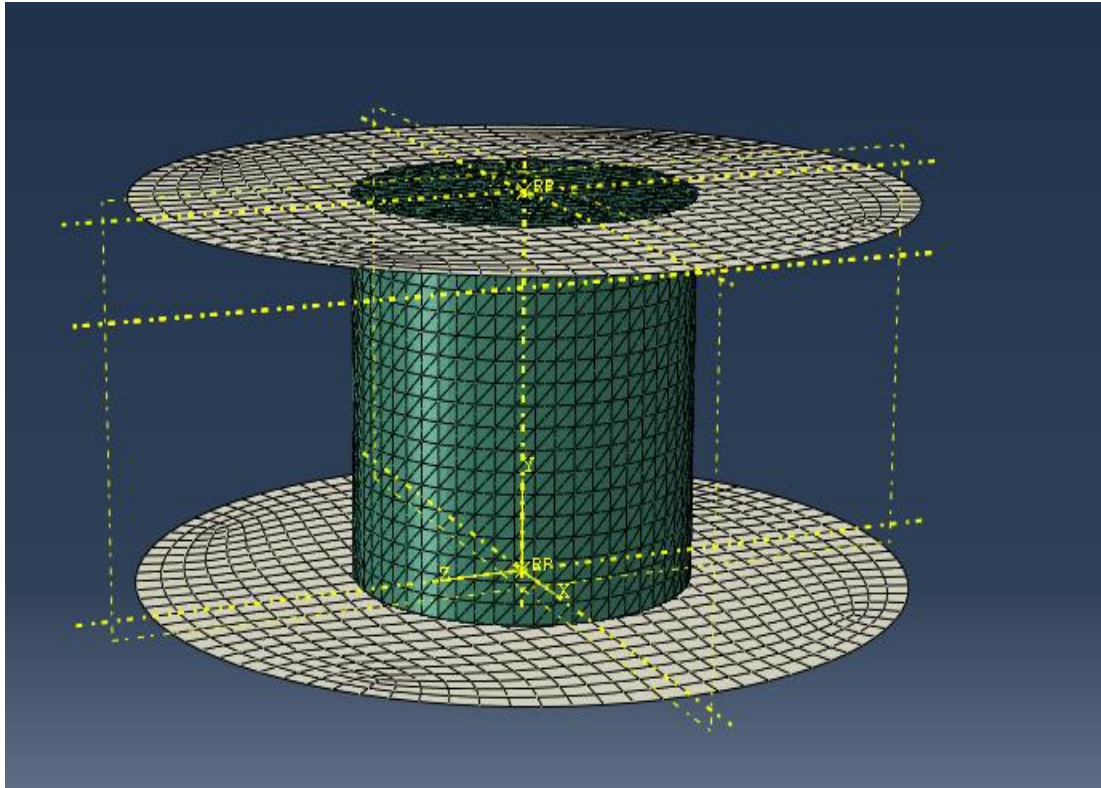


Figure 66 The cylindrical sample meshed with two plate for applying the load.

4.3.2 Material Definition

The material model was specified as in Table.1 and in addition to Fig.2&3. Note that thermal conductivity is neglected since the deformation assumed to be adiabatic, hence, heat is not allowed to transfer between elements during the deformation.

Table 6 Material Properties

Elastic Modulus (GPa)	As per Fig.65 below
Poisson ratio	0.3
Density (Kg/m ³)	8042
Thermal Expansion (K ⁻¹)	1.5E-005
Inelastic heat fraction	0.9
Specific heat (J/ kg-K)	430

Strain hardening and thermal softening play significant role in the material deformation, therefore, it is required to establish the material behavior under different strain rate and at different temperature in the numerical model. The material behavior was incorporated in the model as tabular data as true yield stress- plastic strain behavior. These data must be true yield-stress vs true plastic strain for Abaqus to incorporate the material behavior. Below Figures shows the strain rate and temperature depend data for this alloy that have been incorporated in the data definition in Abaqus

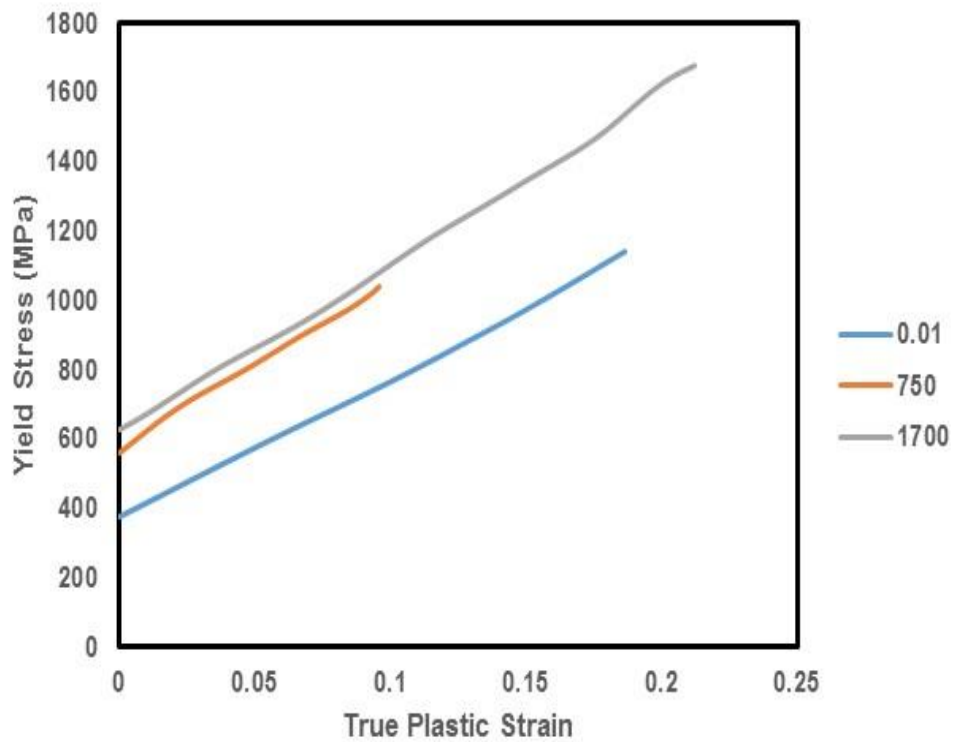


Figure 67 Strain dependent true stress vs true plastic strain of CoCrFeMnNi

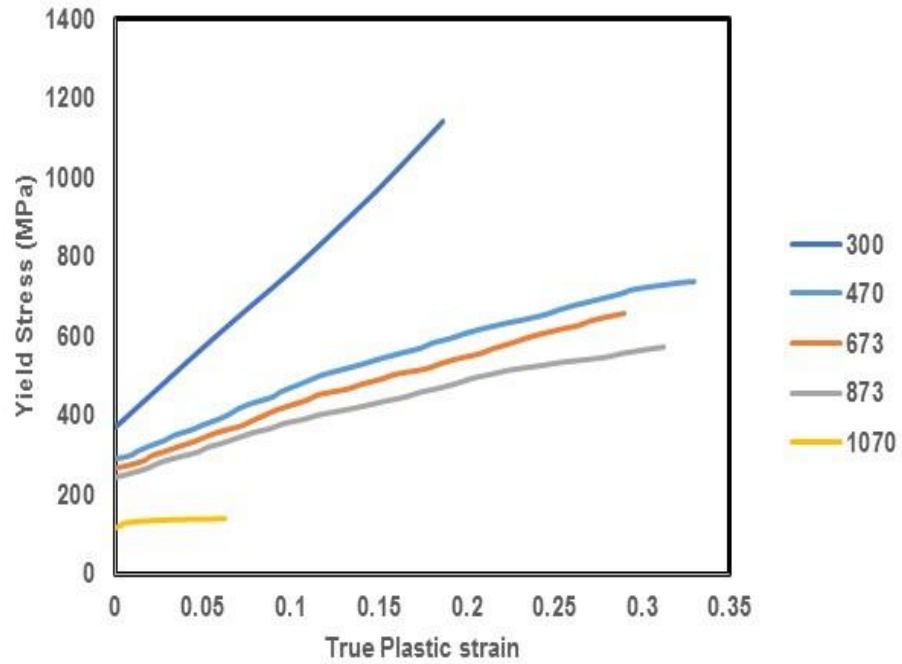


Figure 68 Temperature dependent True Stress vs true plastic strain at constant strain rate of CoCrFeMnNi [22]

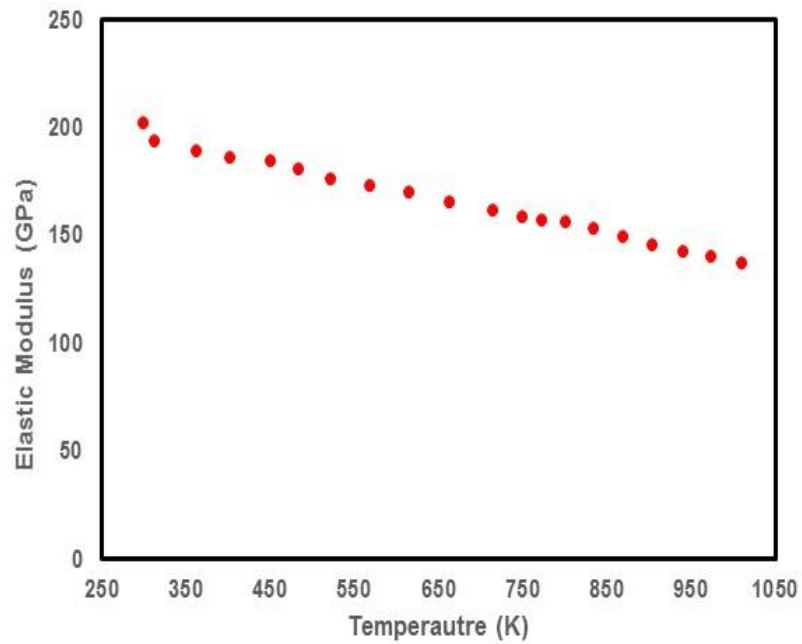


Figure 69 Temperature dependent elastic Modulus of CoCrFeMnNi [22]

Material behavior was incorporated and built in the software as tabular data. As an example, figures below show that the stress strain relationship was built at different strain rate and temperature. As more data to be tabulated, the simulation will be more approximate to the experimental results.

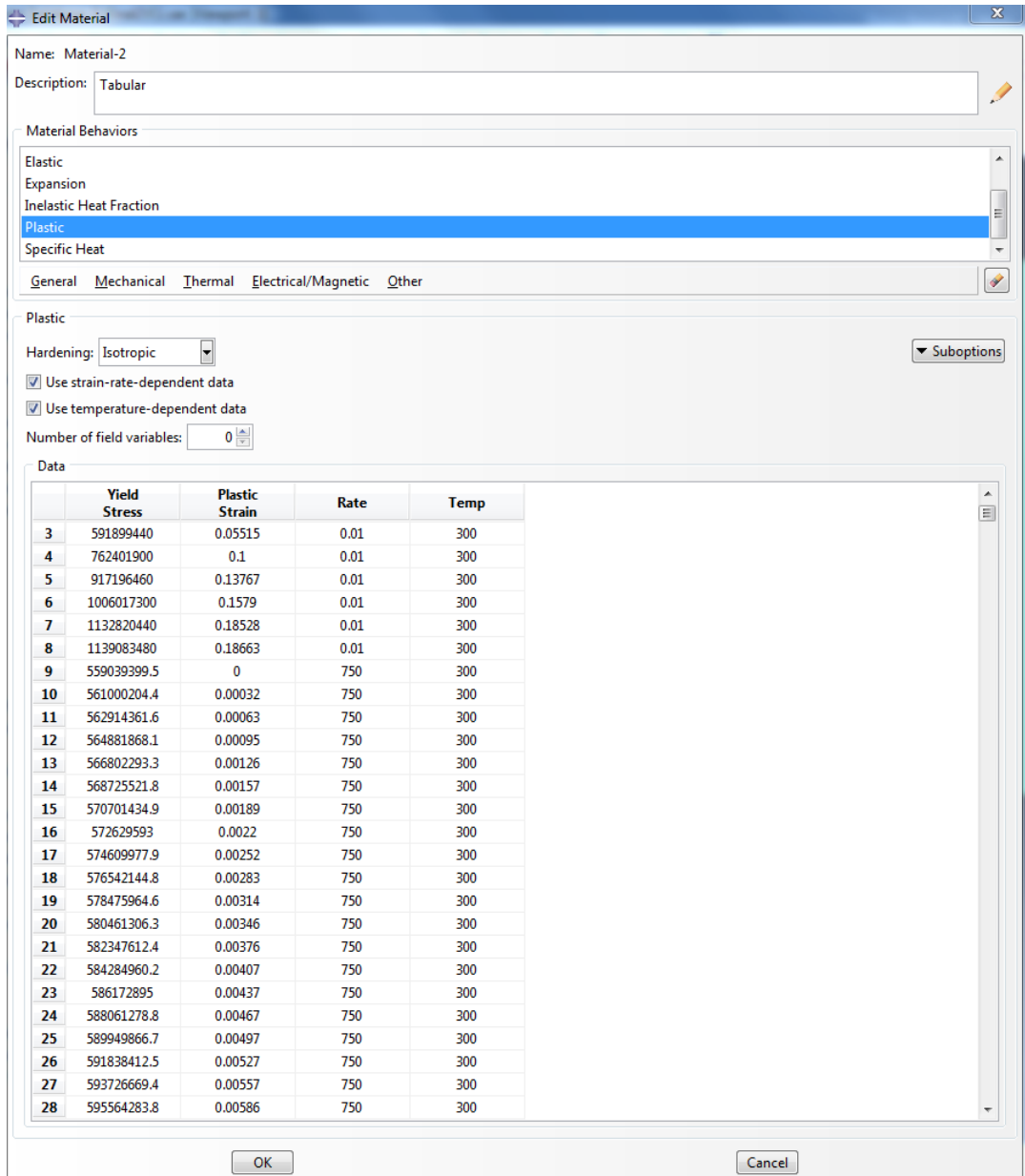


Figure 70 Strain rate dependent plasticity model was incorporated in Abaqus as tabular data for CoCrFeMnNi.

Edit Material

Name: Material-2

Description: Tabular

Material Behaviors

Elastic
Expansion
Inelastic Heat Fraction
Plastic
Specific Heat

General Mechanical Thermal Electrical/Magnetic Other

Plastic

Hardening: Isotropic

Use strain-rate-dependent data
 Use temperature-dependent data

Number of field variables: 0

Data

	Yield Stress	Plastic Strain	Rate	Temp
764	595800000	0.191125122	0.01	470
765	608248000	0.199394516	0.01	470
766	620421000	0.209930242	0.01	470
767	632444000	0.221502147	0.01	470
768	643944000	0.234081202	0.01	470
769	654585000	0.244259565	0.01	470
770	666683000	0.252106556	0.01	470
771	678056000	0.26099598	0.01	470
772	688874000	0.270901611	0.01	470
773	699517000	0.280713818	0.01	470
774	708560000	0.288280964	0.01	470
775	717184000	0.293651224	0.01	470
776	724605000	0.303245608	0.01	470
777	730050000	0.312747005	0.01	470
778	736096000	0.323204871	0.01	470
779	737915000	0.329427138	0.01	470
780	267825000	0	0.01	673
781	275573000	0.007820657	0.01	673
782	287039000	0.016379279	0.01	673
783	298951000	0.020636153	0.01	673
784	311053000	0.029086251	0.01	673
785	323776000	0.037455952	0.01	673
786	335973000	0.045756181	0.01	673
787	348435000	0.05262867	0.01	673
788	360557000	0.060804422	0.01	673
789	373571000	0.071605566	0.01	673

Figure 71 Temperature dependent plasticity model was incorporated in Abaqus as tabular data for CoCrFeMnNi.

4.3.3 Model validation

Once the CoCrFeMnNi material was defined in the software, there was a need to validate the model and compare the simulation and experimental results. There is always an expectation of some deviation as simulation is able mostly to find an approximate and not the exact behavior of the material. Material properties was defined as tabular data as descried in 4.3.2, however, the simulation was also used to validate the Johnson Cook model that has been established for this high entropy in 4.1.2. Cylindrical specimen model, shown in Fig.62, was used to validate this numerical model. Fig.68 shows a comparison between the experiment results with simulation results of tabular and Johnson Cook plasticity models. These results are showing good approximation of the numerical model with the experimental results. It is clear the tabular model was more approximate to the actual stress flow in the material. Therefore, this model has been chosen to be used in this simulation. The tabular model is more time consuming with Johnson cook model since it required to tabulate the material behavior in the software at different temperatures and different strain rate.

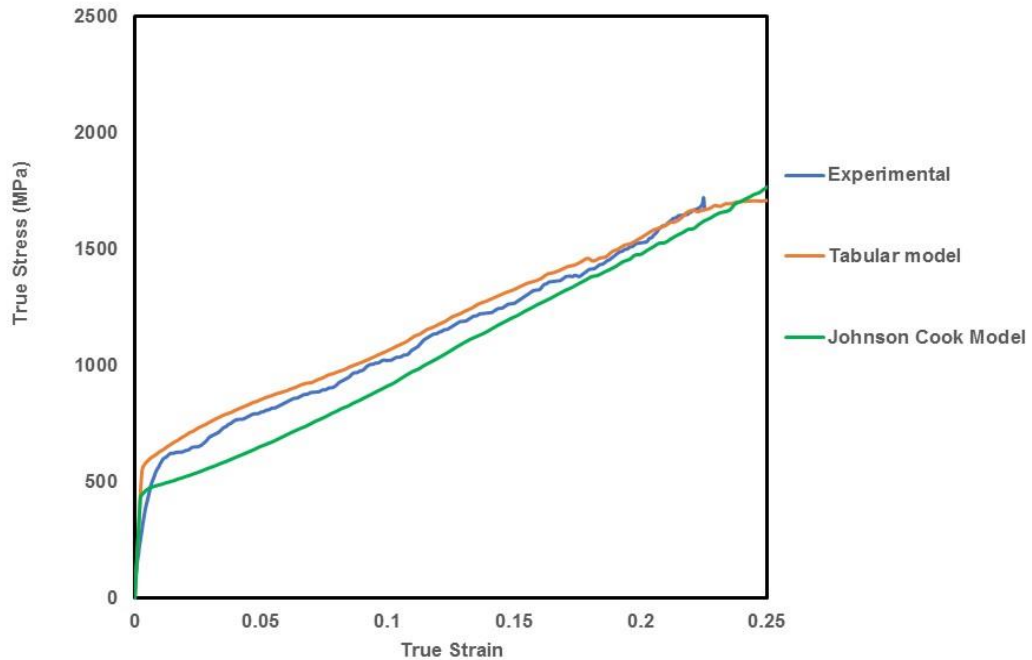


Figure 72 Stress flow comparison between experimental, tabular model and Johnson Cook model results.

4.3.4 Evolution of the shear band

1. Once the sample was impacted and plastic deformation started, high stresses were concentrated on both corners of the design shear band zone. The stresses start and extend from these corners to make a band of high stresses. Meanwhile, effective plastic strain localized at the corners. Below Fig.69 and Fig.70 show the stresses and plastic strain distribution at 10 μ s of impact. In addition, plastic strain concentration is associated with rise in temperature as shown in Fig.71.

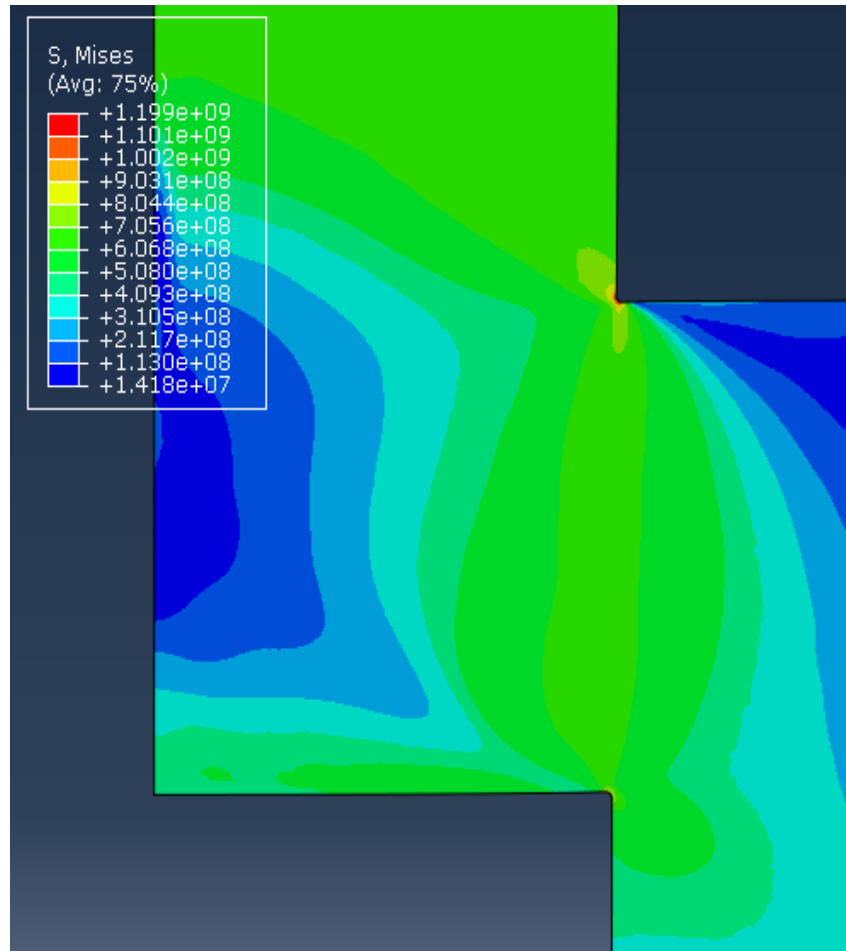


Figure 73 Effective stress at 10 μ s

The effective stress shown in the figure represent Mises stresses during the deformation of the model. The also applies to effective plastic strain which is a scalar quantity that describe the three dimensional plastic strain in the model rather than a strain that is based on one dimension only.

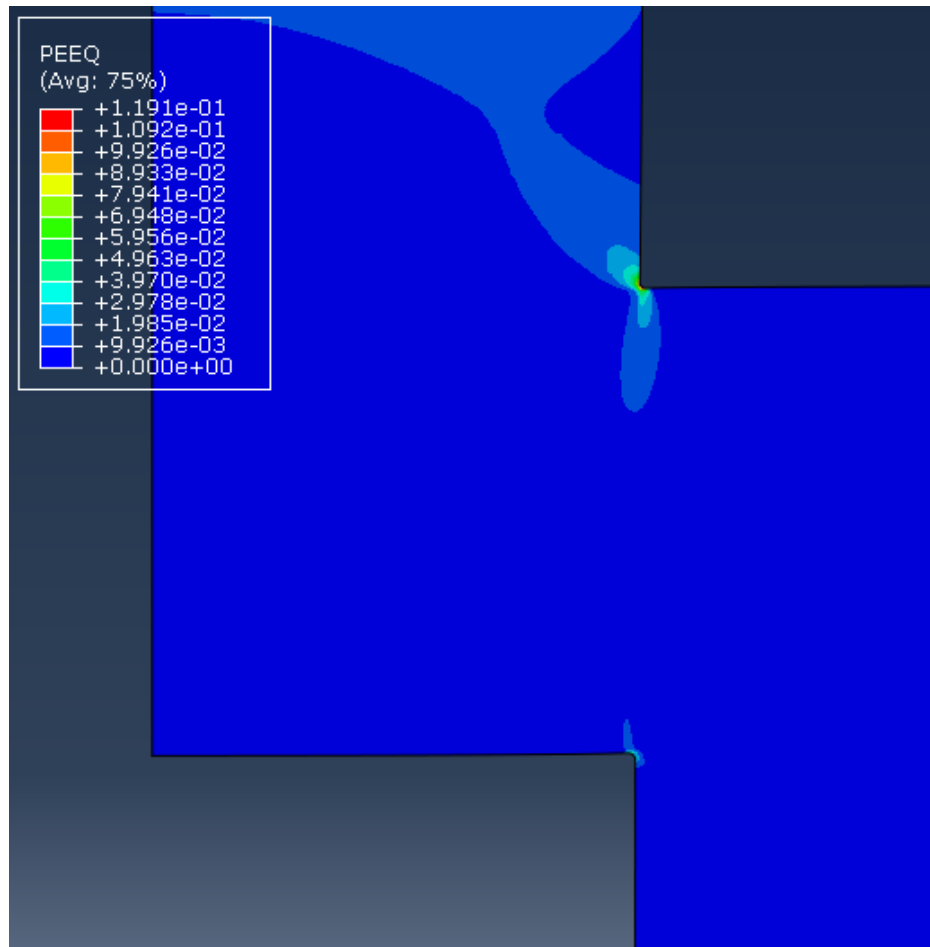


Figure 74 Effective plastic strain at 10 μ s

Note that this effective plastic strain does not mean the start of the shear band that is seen under the microstructural examination. Therefore, to compare the plastic strain in the numerical model with the actual adiabatic shear band localization, temperature rise should be monitored. Once the temperature rise has reached the recrystallization temperature, then effective plastic strain will reflect the actual shear band that is seen in the microstructural examination. Also, temperature profile of the model can be compared with the shear band in the actual examination such as SEM image.

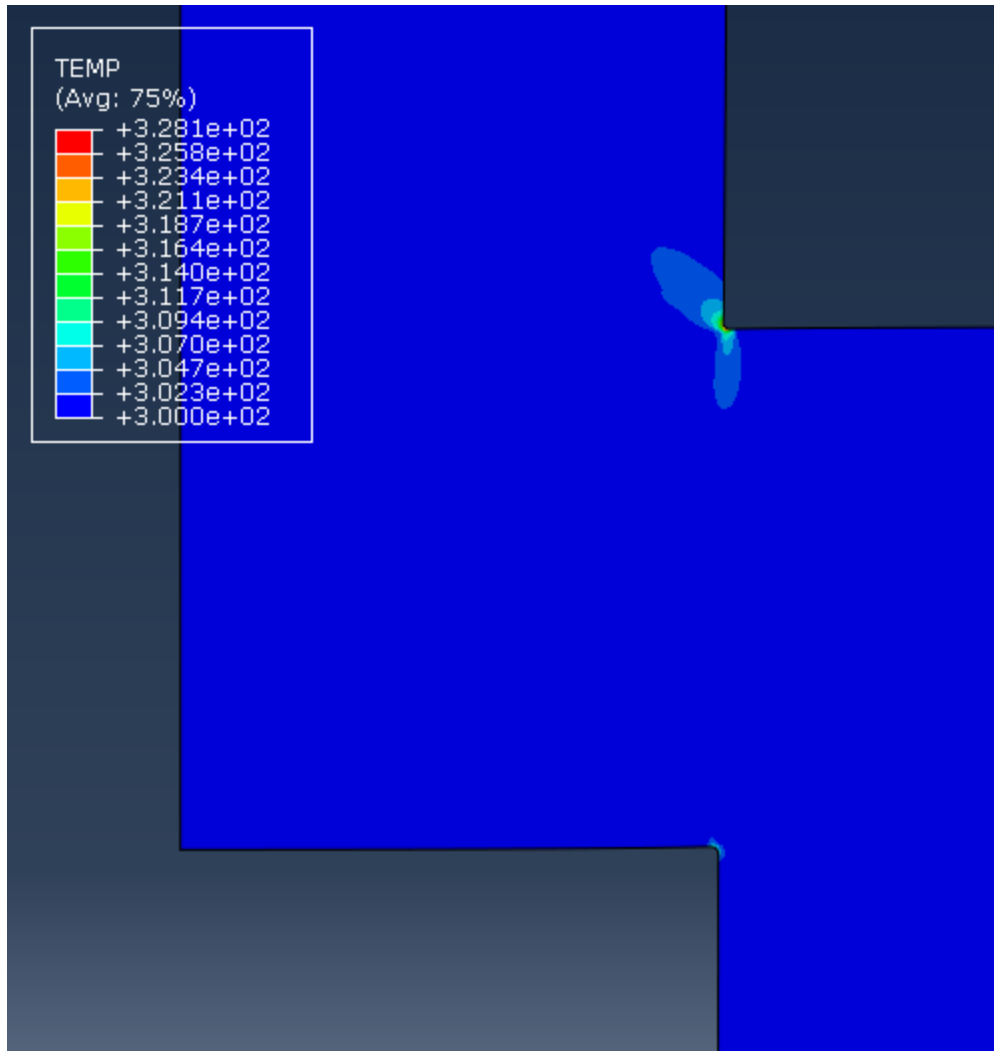


Figure 75 Temperature Distribution at 10 μ s

2. It was assumed that 90% of plastic work converts into heat, hence, leading to temperature rise and softening of the material. Initially, the temperature rise localized at the corners only and mostly in the exterior corner as shown in Fig.71. Therefore, the temperature rise will continue as the plastic strain increases with time and will grow the corresponding plastic strain.
3. The effective plastic strain starts to grow from each corner to be connected along the model.

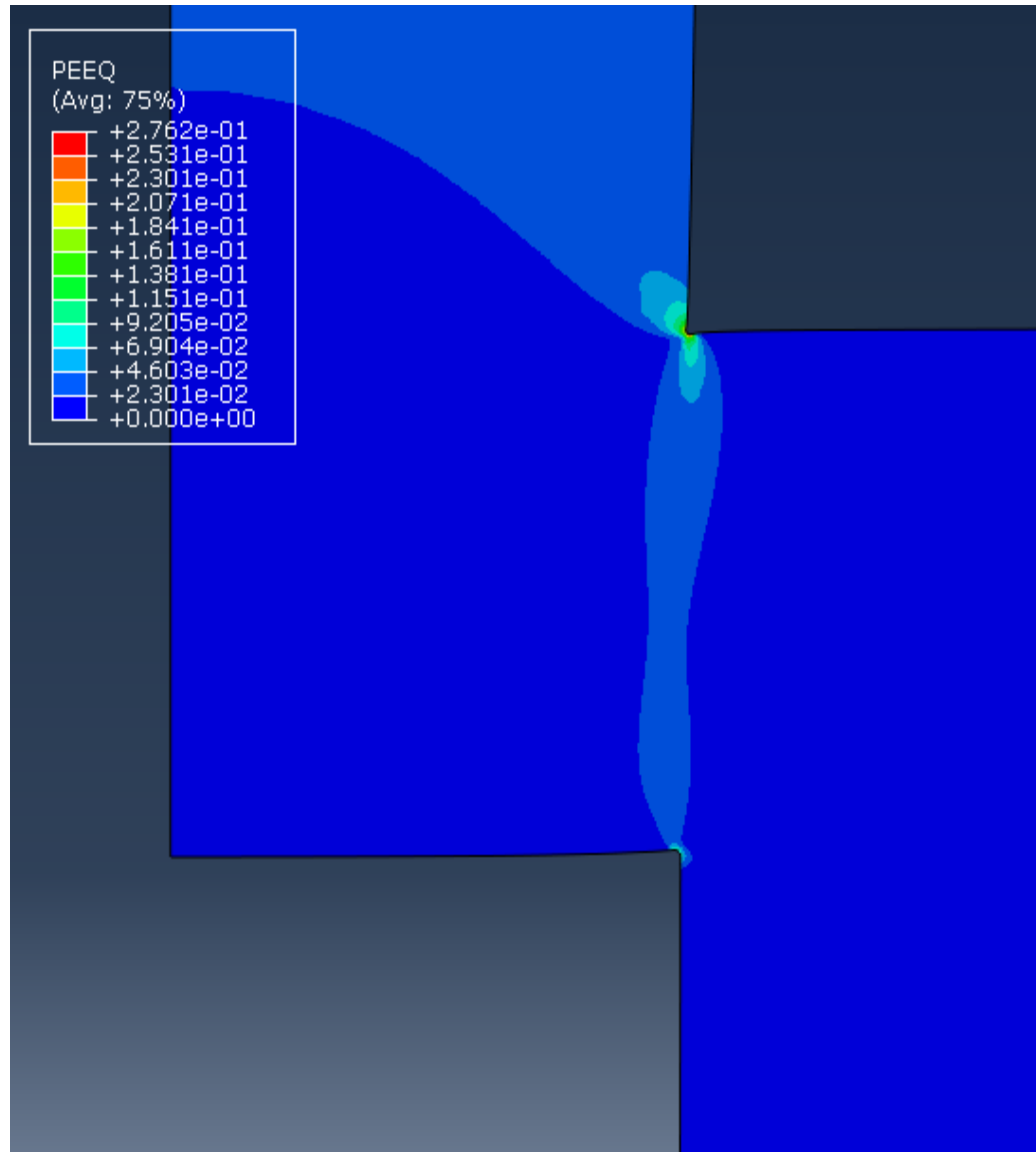


Figure 76 Plastic strain started to grow from each corner and form shear band along the model.

4. The plastic deformation continues by rolling in the exterior corners as shown in Fig.73. Hence, the hat part of the model is being inserted by the force that is exerted on the model.

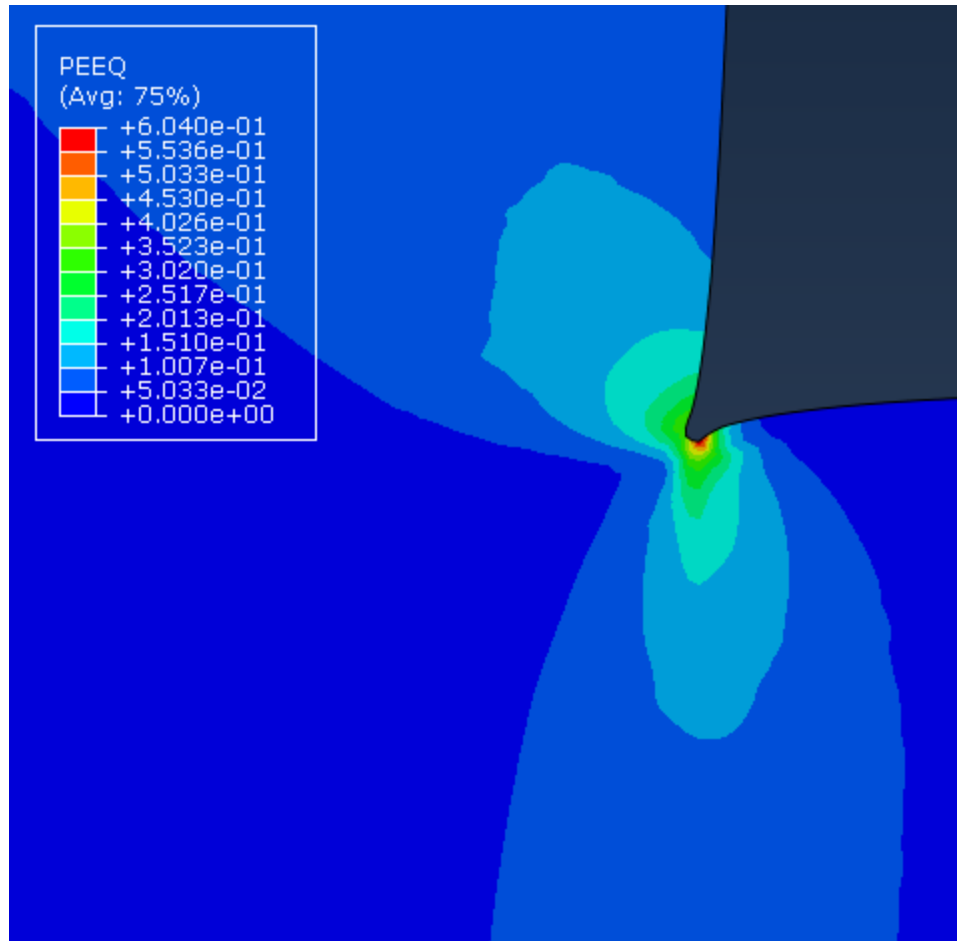


Figure 77 The hat shape specimen continue to deform by rolling in the exterior corner at 50 μ s.

5. The localized temperature rises and plastic strain provided weak path for this crack to start at the corners. The narrow plastic strain and temperature rise band continue to concentrate. The final adiabatic shear band formation in the model is shown in Fig.74

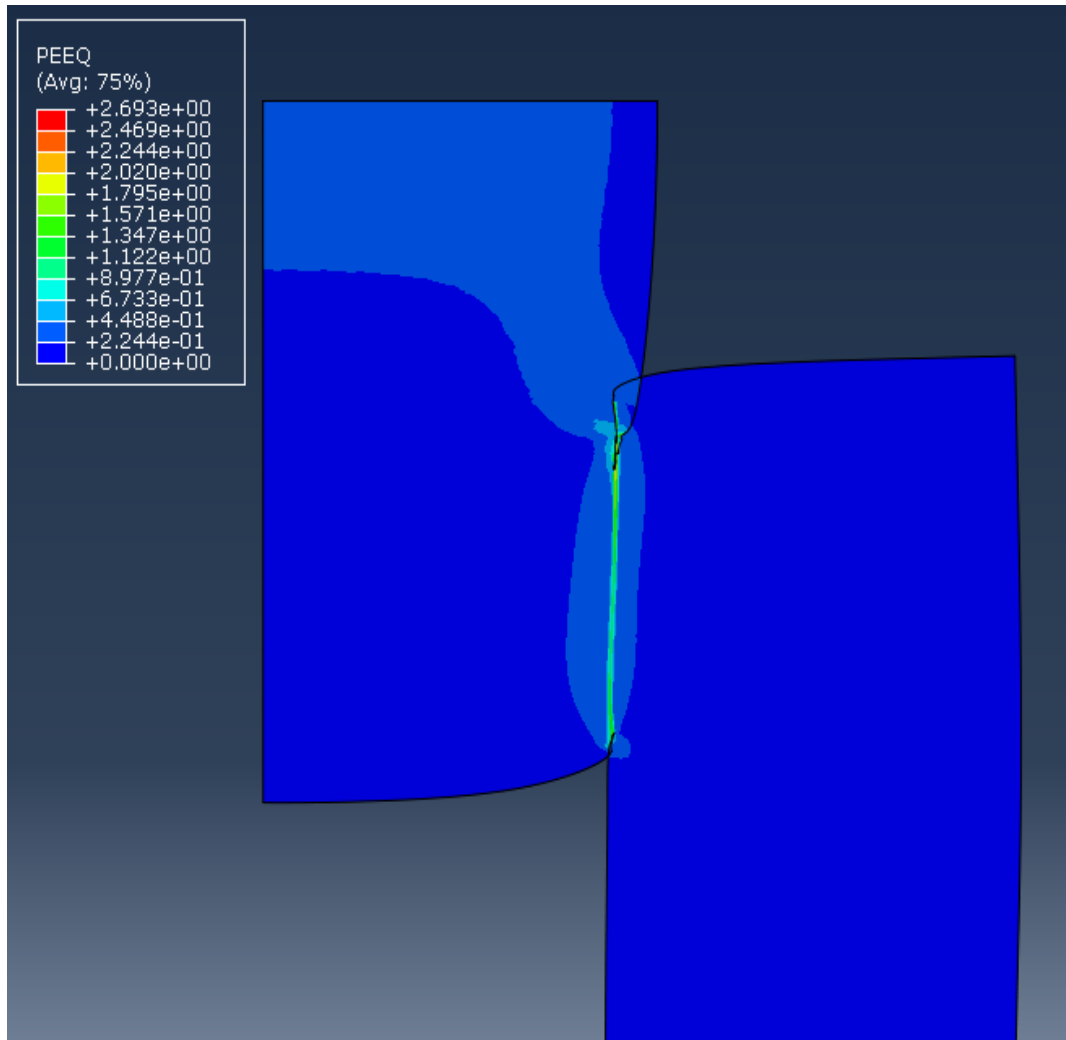


Figure 78 Fully grown plastic strain band at 190 μ s the end of the simulation

- The microscopic characterization of the shear band was based on the critical temperatures, hence, width of the shear bands in the numerical results was measured based on mesh elements that had undergone the critical temperature of $(0.3T_m)$ or more. Below is Fig.75 shows the temperature profile in the model.

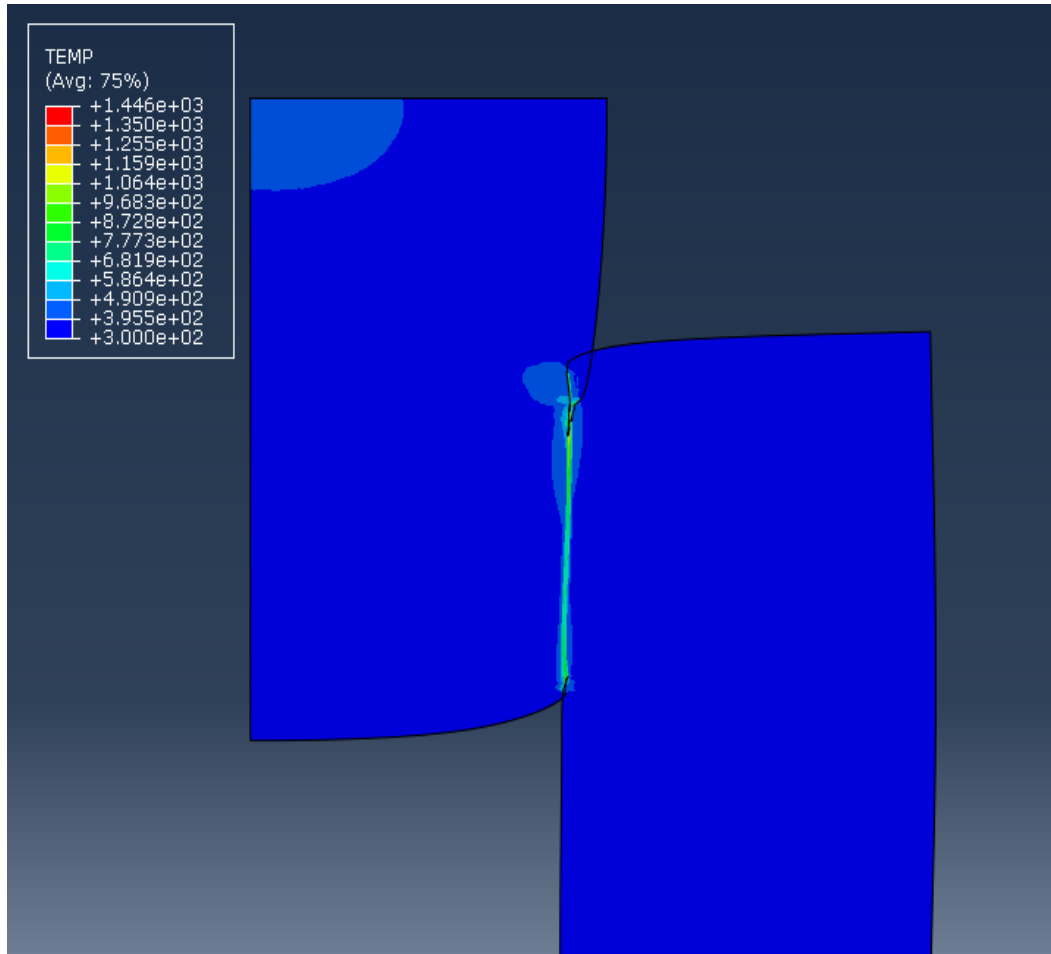


Figure 79 Temperature profile of the adiabatic shear band in the model.

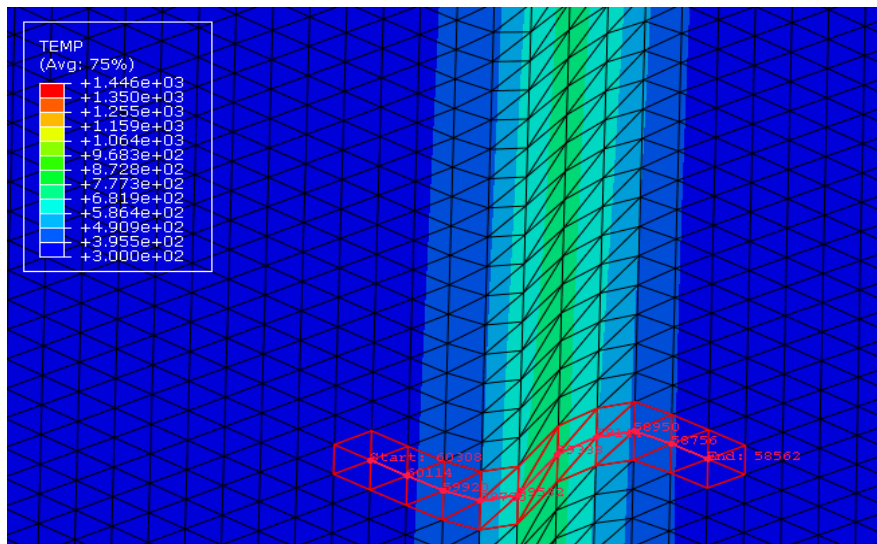


Figure 80 Selected path to measure the temperature rise across the shear band

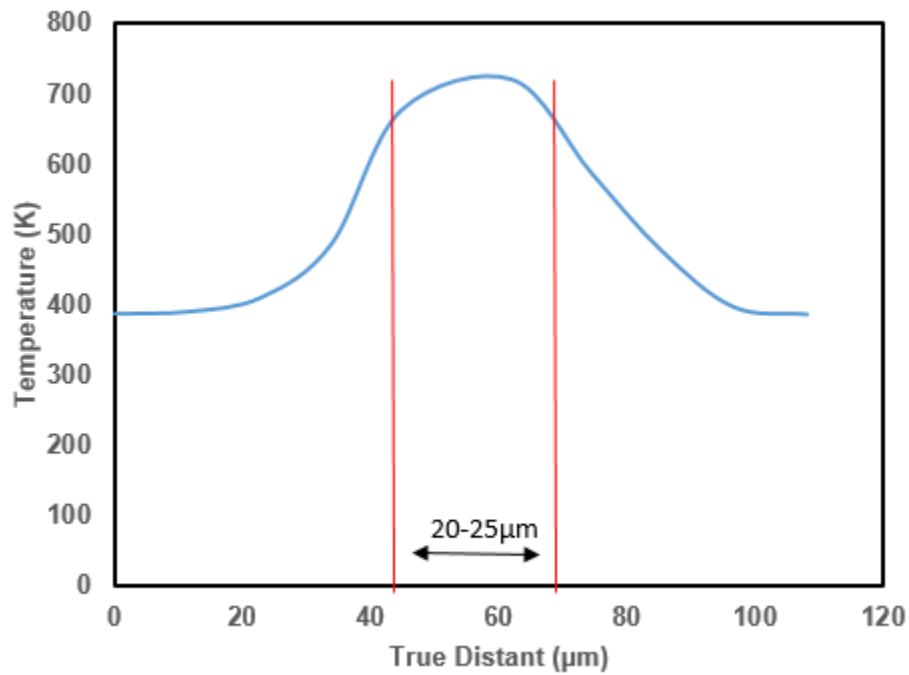


Figure 81 Temperature profile for a path perpendicularly crossing the shear band, the thickness of the shear band is indicated.

The temperature profile was measured by determined a path across the adiabatic shear band then the temperature is measured at the end of the simulation. The width of the shear band is taken as the true distant of between the model elements that reach $0.4T_m$. The width is between $20-25\mu\text{m}$, the element is triangle and its sides' length is in the magnitude of $10\mu\text{m}$ hence it is not easy to determine with better accuracy as these triangles rotate and bend.

5 Conclusion

This work has shown the mechanical response of CoCrFeMnNi high-entropy alloy at different strain rates that range between 10^{-4} s^{-1} to 3000 s^{-1} . In addition, the mechanical response was established at 153K and room temperature. CoCrFeMnNi strengthens with increasing the strain rate and lowering the temperature. At strain rate of 10^{-4} s^{-1} , yield stress jumps from 380 MPa at room temperature to 430 MPa at 153K. At room temperature, the yield stress jump from 380 MPa at strain rate of 10^{-4} s^{-1} to around 540 MPa at 1600 s^{-1} . However, at 153K, the yield stress jump from 430 MPa at strain rate of 10^{-4} s^{-1} to around 650 MPa at 3000 s^{-1} . Strain rate sensitivity is 0.0246 and 0.0202 for room temperature and 153K respectively.

The initial and deformed alloy's microstructure was examined by optical microscopy, SEM, EBSD and TEM. The initial average grains size was $10 \mu\text{m}$ and grains were polygonal. This alloy formed FCC while it has elements of four different phases. Adiabatic shear bands were observed in CoCrFeMnNi hat shape specimens at 153K and room temperature. The grains inside the shear band were extremely refined to elongated equiaxed nanograins. There were dual refinement mechanisms; the deformation twinning, nanotwinning and rotational dynamic recrystallization. Dislocation cells played important part in refining this alloy microstructure by subdividing the initial grains to subgrains. Then rotational dynamic recrystallization helped to the grains to rotate and form equiaxed grains. Finally, additional nanotwinning refined the microstructure and formed nano structures as TEM evidence shows. The initial average grain size was $10 \mu\text{m}$ while the refined equiaxed nanograins were between $0.05\text{-}0.2 \mu\text{m}$. CoCrFeMnNi show excellent microhardness inside the shear band and superior property compared with 316L austenitic stainless steel.

Adiabatic shear band was also observed in finite element model. The numerical model shows good approximation with the actual results and also used to validate the developed Johnson Cook plasticity model.

6 References

- [1] Ashby, M.F., 2011 *Materials Selection in Mechanical Design*, Fourth ed. Butterworth-Heinemann, Elsevier, Oxford, UK.
- [2] Taylor, George Rogers. *The Transportation Revolution, 1815–1860*. ISBN 978-0-87332-101-3. No name is given to the transition years. The Transportation Revolution began with improved roads in the late 18th century
- [3] Cantor, B., Chang, I.T.H., Knight, P., Vincent, A.J.B., 2004 Microstructural development in equiatomic multicomponent alloys. *Mater.Sci Eng. A* 375-377,213-218
- [4] B.S. Murty, J.W. Yeh, S. Ranganathan, *High Entropy Alloys*, Elsevier (2014)
- [5] Cantor, B. Multicomponent and High Entropy Alloys. *Entropy* **2014**, 16, 4749-4768
- [6] Yeh, J.W. ., 2013a. Alloy design strategies and future trends in high-entropy alloys. *J. Met.* 65, 1759-1771.
- [7] Fultz, B., 2010. Vibrational thermodynamics of materials. *Prog. Mater Sci.* 55, 247-352.
- [8] Tasi, K.Y., Tsai, M.H., Yeh, J.W., 2013. Sluggish diffusion in Co-Cr-Fe-Mn-Ni high-entropy alloys. *Acta Mater.* 61, 4887-4897.
- [9] Yeh J. (2015) "Physical metallurgy of high-entropy alloys" *JOM*, 67, 2254-2261.
- [10] C.J. Tong, S.K. Chen, J.W. Yeh, T.T. Shun, C.H. Tsau, S.J. Lin, and S.Y. Chang, Microstructure Characterization of Al_xCoCrCuFeNi High-Entropy Alloy System with Multi-principal Elements, *Metall. Mat. Trans. A*, 36A (2005) 881-893.
- [11] Zhou YJ, Zhang Y, Wang YL, Chen GL. Solid solution alloys of AlCoCrFeNiTi_x with excellent room-temperature mechanical properties. *Appl Phys Lett* 2007;90(18):181904.
- [12] Wang XF, Zhang Y, Qiao Y, Chen GL. Novel microstructure and properties of multicomponent CoCrCuFeNiTi_x alloys. *Intermetallics* 2007;15(3):357–62.

- [13] Gludovatz B, Hohenwarter A, Catoor D, Chang EH, George EP, Ritchie RO "A fracture-resistant high-entropy alloy for cryogenic applications," *Sci.* 345(6201), 1153–1158 (2014).
- [14] Chou, Y.L., Wang, Y.C Yeh, J.W., 2009. Microstructure, thermophysical and electrical properties in $Al_xCoCrFeNi$ ($0 \leq x \leq 2$) high entropy alloys. *Mater.Sci eng. B* 163, 184-189.
- [15] B. Dodd and Y.L. Bai, *Adiabatic Shear Localization: Frontiers and Advances*, Elsevier, Waltham, 2012
- [16] B. Gludovatz, A. Hohenwarter, K. V. S. Thurston, H. Bei, Z. Wu, E. P. George and R. O. Ritchie. Exceptional Damage-Tolerance of a Medium-Entropy Alloy CrCoNi at Cryogenic Temperatures. *Nature Communications*, vol. 7:10602, Feb. 2016.
- [17] Y. Liu, J. Wang, Fang, B. Liu, Y. Wu and S. Chen, Preparation of superfine-Grained High Entropy Alloy by Spark Plasma Sintering Gas Atomized Powder, *Intermetallics*, 2013, 68, P 16-22
- [18] Derby B. *Acta Metall* 1991;39:955
- [20] Hughes DA, Lebensohn RA, Wend HR, Kumar A. *Proc R Soc Lond A* 2000;456:921.
- [22] Humphreys FJ, Hatherly M. *Recrystallization and related annealing phenomena*. Oxford: Pergamon;1995
- [23]M.A. Meyers, V.F. Nesterenko, J.C. LaSalvia, and Q. Xue, Shear Localization in Dynamic Deformation of Materials: Microstructural Evolution and Self-Organization, *Matls. Sci. and Eng. A*317 (2001) 204-225.
- [24] "ABAQUS Users Manual V6.14", Dassault Systems 2016

- [25] Michael C. Gao, Jien-Wei Yeh, Peter K. Liaw, Yong Zhang, High-Entropy Alloys, Fundamentals and Applications
- [26] F. Otto, A. Dlouhy, Ch. Somsen, H. Bei, G. Eggeler, E.P. George, The influences of temperature and microstructure on the tensile properties of a CoCrFeMnNi high-entropy alloy, *Acta Materialia*
- [27] Volume 61, Issue 15, September 2013, Pages 5743–5755
- [28] R.F. Mehl, A Brief History of the Science of Metals, American Institute of Mining, Metallurgical, and Petroleum Engineers, 1948
- [29] C.W. Tsai, M.H. Tsai, J.W. Yeh, C.C. Yang, Effect of temperature on mechanical properties of Al_{0.5}CoCrCuFeNi wrought alloy *J Alloy Compd*, 490 (1–2) (2010), pp. 160–165
- [30] Richie, R O. Gludocatz, B *The Journal of the Minerals, Metals & Material Society*, August 2015
- [31] Otto, F., Yang, Y., Bei, H. & George, E. P. Relative effects of enthalpy and entropy on the phase stability of equiatomic high-entropy alloys. *Acta Mater.* 61, 2628–2638 (2013).
- [32] Y. B. Xu and M. A. Meyers, Nanostructural and Microstructural Aspects of Shear Localization at High-Strain Rates for Materials, in *Adiabatic Shear Localization*, Chapter 3, 2012, B. Dodd and Y. L. Bai, eds., Elsevier.
- [33] M. A. Meyers, M. T. Perez-Prado, Q. Xue, Y. Xu, and T. R. McNelley, Microstructural Evolution In Adiabatic Shear Localization In Stainless Steel, *Acta Materialia*, 51(2003)1307-1325.
- [34] M.A. Meyers, Q. Xue, and V.F. Nesterenko, Evolution in the Patterning of Adiabatic Shear Bands, in *Shock Compression of Condensed Matter*, 2001, (2002) 567-570, AIP.

- [35] M.A. Meyers, M.T. Perez-Prado, Q. Xue, Y. Xu, and T.R. McNelley, Microstructural Evolution in Adiabatic Shear Localization in Stainless Steel, in Shock Compression of Condensed Matter, 2001, (2002)571-574 , AIP.
- [36] J.H. Beatty, Y.-F. Li, M.A. Meyers, and S. Nemat-Nasser, "Adiabatic Shear-Banding in High-Strength Alloys", Proc. 12th Army Symposium on Solid Mechanics, ed. S.C. Chou, 331-345 (1991)
- [37] J.H. Beatty, L.W. Meyer, M.A. Meyers, and S. Nemat-Nasser, "Formation of Controlled Adiabatic Shear Bands in AISI 4340 High Strength Steel", in "Shock Waves and High-Strain-Rate Phenomena in Materials", eds., M.A. Meyers, L.E. Murr, and K.P. Staudhammer, M. Dekker, p. 645-656 (1992).
- [38] C.L. Wittman, M.A. Meyers, and H.-r. Pak, "Observation of an Adiabatic Shear Band in AISI 4340 Steel by High-Voltage Transmission Electron Microscopy", Met. Trans.A, 21A, p. 707-716, (1990).
- [39] M.A. Meyers and H.-r. Pak, "Observation of an Adiabatic Shear Band in Titanium by High Voltage Transmission Electron Microscopy", Acta Met., 34, p. 2493-2499 (1986).
- [40] Chichili, D.R., Ramesh, K.T., Hemker, K.J., 1998. The high-strain-rate response of alpha-titanium: experiments, deformation mechanisms and modeling. Acta Mater. 46, 1025e1043.
- [41] Clayton, J.D., 2005. Dynamic plasticity and fracture in high density polycrystals: constitutive modeling and numerical simulation. J. Mech. Phys. Solids 53, 261e301.
- [42] Meissonnier, F.T., Busso, E.P., O'Dowd, N.P., 2001. Finite element implementation of a generalised non-local rate-dependent crystallographic formulation for finite strains. Int. J. Plast. 17, 601e640
- [43] Meyers, M.A., 1994. Dynamic Behavior of Materials. Wiley, New York.

- [44] Ranc, N., Taravella, L., Pina, V., Herve, P., 2008. Temperature field measurement in titanium alloy during high strain rate loading e adiabatic shear bands phenomenon. *Mech. Mater.* 40, 255e270.
- [45] Zhou, M., Ravichandran, G., Rosakis, A.J., 1996a. Dynamically propagating shear bands in impact-loaded prenotched plates. 2. Numerical simulations. *J. Mech. Phys. Solids* 44, 1007e1032.
- [46] Wright, T.W., Ockendon, H., 1996. A scaling law for the effect of inertia on the formation of adiabatic shear bands. *Int. J. Plast.* 12, 927e934.
- [47] Dorogoy, A. & Rittel, D. Numerical validation of the shear compression specimen. Part I: Quasi-static large strain testing. *Exp. Mech.* 45, 167–177 (2005).
- [48] Teng, X., Wierzbicki, T. & Couque, H. On the transition from adiabatic shear banding to fracture. *Mech. Mater.* 39, 107–125 (2007).
- [49] Zener, C. & Hollomon, J. Effect of strain rate upon plastic flow of steel. *J. Appl. Phys.* 15, 22–32 (1944).
- [50] Knott, J.F. *Fundamentals of fracture mechanics*, Butterworths 1973.
- [51] William.D. Callister Jr., David.G.Rethwisch, *Material Science and Engineering* - 8th edition, John Wiley and Sons Inc.
- [52] A. G.Guy, *Essentials of Materials Science*, McGraw-Hill Book Company, New York, 1976, p. 153.
- [53] Kelly, A.,G.W. Groves, and P. Kidd, *Crystallography and Crystal Defects*,Wiley, Hoboken, NJ, 2000.

- [54] Meyers, M. A., and K. K. Chawla, *Mechanical Behavior of Materials*, Prentice Hall, Upper Saddle River, NJ, 1999.
- [55] G. I. Taylor, The Mechanism of Plastic Deformation of Crystals. Part II. Comparison with Observations, *Proc. R. Soc. Lond. A.* 1934 145 388-404
- [56] MA Meyers, C Aimone, Dynamic Fracture (Spalling) of Metals, *Progress in Materials Science*, 1983. vol 28: p. 1-96.
- [57] F Seitz, TA Read, Theory of the Plastic Properties of Solids I, *Journal of Applied Physics*, 1941. vol 12(2): p. 100-118.
- [58] J Weertman, *Shock Waves and High-Strain Rate Phenomena in Metals*, ed. MA Meyers and LE Murr, New York: Plenum, 1981, p. 607-673.
- [59] MA Meyers, HN Jarmakani, EM Bringa, BA Remington, *Dislocations in Solids*, ed. JP Hirth, L Kubin, Amsterdam: North-Holland, 2009, p. 91.
- [60] MD Furnish, LC Chhabildas, DJ Steinberg, *Dynamic Material Properties of Refractory Metals: Tantalum and Tantalum/Tungsten Alloys*, *Shock Compression of Condensed Matter*, 1994. vol 309: p. 1099.
- [61] G. Laplanche, P. Gadaud, O. Horst, F. Otto, G. Eggeler, E.P. George, Temperature dependencies of the elastic moduli and thermal expansion coefficient of an equiatomic, single-phase CoCrFeMnNi high-entropy alloy, *J. Alloys Cmpds.* 623 (2015) 348e353

[62] P.P. Bhattacharjee, G.D. Sathiaraj, M. Zaid, J.R. Gatti, C. Lee, C.W. Tsai, J.W. Yeh, Microstructure and texture evolution during annealing of equiatomic CoCrFeMnNi high-entropy alloy, *J. Alloys Compd.* 587 (2014) 544e552.

[63] D Hull, DJ Bacon, Introduction to Dislocations, Oxford: Butterworth-Heinemann, 2001, p. 1-157.

[64] B. Schuh, F. Mendez-Martin, B. Volker, E.P. George, H. Clemens, R. Pippan, A. Hohenwarter, Mechanical properties, microstructure and thermal stability of a nanocrystalline CoCrFeMnNi high-entropy alloy after severe plastic deformation, *Acta Mater* 96 (2015) 258e268.

[65] J.-W. Yeh, S.-K. Chen, S.-J. Lin, J.-Y. Gan, T.-S. Chin, T.-T. Shun, C.-H. Tsau, S.-Y. Chang, Nanostructured high-entropy alloys with multiple principal elements: Novel alloy design concepts and outcomes, *Adv. Eng. Mater.* 6 (2004) 299e303.

[66] F. Zhang, C. Zhang, S.L. Chen, J. Zhu, W.S. Cao, U.R. Kattner, An understanding of high entropy alloys from phase diagram calculations, *Calphad* 45 (2014) 1e10

[67] D.R. Gaskell, Introduction to the Thermodynamics of Materials, third ed., Taylor & Francis, Washington, DC USA, 1995.

[68] L.J. Santodonato, Y. Zhang, M. Feygenson, C.M. Parish, M.C. Gao, R.J.K. Weber, J.C. Neufeind, Z. Tang, P.K. Liaw, Deviation from high-entropy configurations in the atomic distributions of a multi-principal-element alloy, *Nat. Commun.* 6 (2015) 5964.

[69] T. W. Wright and R. C. Batra, The Initiation and Growth of Adiabatic Shear Bands, *Int. J. Plasticity*, **1**, 205-212, 1985.

- [70] R. C. Batra and C. H. Kim, An Adaptive Mesh Refinement Technique for the Analysis of Adiabatic Shear Banding, *Mechs. Research Communications*, **17**, 81-91, 1990.
- [71] R. C. Batra and L. Wang, Analysis of Dynamic Shear Bands Under Combined Loading, *Int. J. Eng'g Analysis & Design*, **1**, 79-90, 1994.
- [72] Belotserkovsky, 1994 "Numerical Methods in Continuum Mechanics", Moscow, Fizmatlit, 2nd edition, p.441.
- [73] Umbrello D, Outeiro J.C., M'Saoubi R. The Influence of Johnson - Cook Material Constants on Finite Element Simulation of Machining of AISI 316L Steel. *Int. J. Mach. Tools Manuf.* 2007; **47**: 462–470.
- [74] Abushawashi Y, Xiao X, Astakhov V. A novel approach for determining material constitutive parameters for a wide range of triaxiality under plane strain loading conditions. *Int. J. Mech. Sci.* 2013; **74**: 133–142
- [75] Wang XM and Shi J. Validation of Johnson-Cook plasticity and damage model using impact experiment. *Int. J. Impact Eng.* 2013; **60**: 67-75.
- [76] Asad M, Mabrouki T, Girardin F, Zhang Y, Rigal JF. Towards a physical comprehension of material strengthening factors during macro to microscale milling *Mechanics* 2011; **17**(1): 97-104.
- [77] Johnson GR, Cook WH. A constitutive model and data for metals subjected to large strains, high strain rates and high temperatures. In: *Proc. 7th Int. Symp. On Ballistics*, Hague, Netherlands, April 1983; 541– 547

- [78] Bancroft, D., (1941) 'The velocity of longitudinal Waves in cylindrical Bars', physical Review, V.59 No.59, pp.588-593
- [79] Davies, R. M., (1948) 'A critical study of the Hopkinson pressure bar', phil. Trans. R. Soc., A240, pp.375-457
- [80] Nemat-Nasser, Jon Issac and John Starett. (1991) 'Hopkinson bar techniques for dynamic recovery experiments.' Proc. Royal Soc. Lond. A-435, pp.371-91.
- [81] Y. B. Xu and M. A. Meyers, Nanostructural and Microstructural Aspects of Shear Localization at High-Strain Rates for Materials, in Adiabatic Shear Localization, Chapter 3, 2012, B. Dodd and Y. L. Bai, eds., Elsevier.
- [82] M.A. Meyers, L.W. Meyer, J. Beatty, U. Andrade, K.S. Vecchio, and A. Chokshi, "High Strain, High-Strain Rate Deformation of Copper", in "Shock Waves and High-Strain-Rate Phenomena in Materials", eds., M.A. Meyers, L.E. Murr, and K.P. Staudhammer, M. Dekker, p. 529-542 (1992)
- [83] M. Mishra, M. Martin, N.N. Thadhani, B.K. Kad, E.A. Kenik, and M.A. Meyers, High-Strain Rate Response of Ultra-Fine Grained Copper, Acta Mat., Vol. 56, pp. 2770-2783, 2008.
- [84] M.A. Meyers, J.C. LaSalvia, V.F. Nesterenko, and B.K. Kad, Dynamic Recrystallization in High-Strain-Rate Deformation, in Recrystallization and Related Phenomena, Ed. J.R. McNelley, Proc. Rex. 96, 279-286.
- [85] W.Y. Tang, J.W. Yeh Effect of aluminum content on plasma-nitrided $\text{Al}_x\text{CoCrCuFeNi}$ high entropy alloys Metall. Mater. Trans. A, 40A (2009), pp. 1479-1486

- [86] U. Roy, H. Roy, H. Daoud, U. Glatzel, K.K. Ray Fracture toughness and fracture micromechanism in a cast AlCoCrCuFeNi high entropy alloy system Mater. Lett., 132 (2014), pp. 186-189
- [87] W.H. Liu, Y. Wu, J.Y. He, T.G. Nieh, Z.P. Lu Grain growth and the Hall-Petch relationship in a high-entropy FeCrNiCoMn alloy Scr. Mater., 68 (2013), pp. 526-529
- [88] C. Wang, W. Ji, Z.Y. Fu Mechanical alloying and spark plasma sintering of CoCrFeNiMnAl high-entropy alloy. Adv. Powder Technol., 25 (2014), pp. 1334-1338
- [89] M.-X. Ren, B.-X. Li, H.-Z. Fu Formation condition of solid solution type high-entropy alloy Trans. Nonferrous Metals Soc. China (English Edition), 23 (2013), pp. 991-995
- [90] W. Hume-Rothery, R.W. Smallman, C.W. Haworth The Structure of Metals and Alloys The Institute of Metals, London (1969)
- [91] Y. Zhang, X. Yang, P.K. Liaw Alloy design and properties optimization of high-entropy alloys JOM, 64 (2012), pp. 830-838.
- [92] L.J. Santodonato, Y. Zhang, M. Feygenson, C.M. Parish, M.C. Gao, R.J.K. Weber, J. C. Neufeind, Z. Tang, P.K. Liaw Deviation from high-entropy configurations in the atomic distributions of a multi-principal-element alloy Nat. Commun., 6 (2015), p. 5964
- [93] M.C. Gao, J.-W. Yeh, P.K. Liaw, Y. Zhang High-entropy Alloys: Fundamentals and Applications Springer Publishing Co., New York, NY (2016)
- [94] F.J. Zerilli, R.W. Armstrong, Dislocation mechanics based constitutive relations for material dynamic calculations, J. Appl. Phys. 61 (1987) 1816.
- [95] Y.H. Zhang, Y. Zhuang, A. Hu, J.J. Kai, C.T. Liu, The origin of negative stacking fault energies and nano-twin formation in face-centered cubic high entropy alloys, Scr. Mater. 130 (2017) 96–99.

- [96] Y.T. Zhu, X. Z. Liao, S.G. Srinivasan, E.J. Lavernia, Nucleation of deformation twins in nanocrystalline face-centered-cubic metals processed by severe plastic deformation, *Appl. Phys. Lett.* 98 (2005) 034319.
- [97] D.-H. Lee, M.-Y. Seok, Y. Zhao, I.-C. Choi, J. He, Z. Lu, J. Suh, U. Ramamurty, M. Kawasaki, T.G. Langdon, J.-il Jang, Spherical nanoindentation creep behavior of nanocrystalline and coarse-grained CoCrFeMnNi high-entropy alloys, *Acta Mater.* 109 (2016) 314-322.
- [98] Z. Li, S. Zhao, H. Diao, P. K. Liaw, M.A. Meyers, High-velocity deformation of $Al_{0.3}CoCrFeNi$ high-entropy alloy: Remarkable resistance to shear failure, *Sci. Rep.* (2016) 7:42742.
- [98] X.H. Chen, J. Lu, L. Lu, K. Lu, Tensile properties of a nanocrystalline 316L austenitic stainless steel, *Scr. Mater.* 52 (2005) 1039–1044.
- [99] Narita, N. and Takamura, J. -I., *Dislocations in Solids*, Vol. 9, ed. F.R.N. Nabarro, (1992) 135–189.
- [100] A.J. Zaddach, C. Niu, C.C. Koch, D.L. Irving, Mechanical Properties and Stacking Fault Energies of NiFeCrCoMn High-Entropy Alloy, *J. Mater.* 65 (2013) 1780-1789.
- [101] G. Laplanche, A. Kostka, O.M. Horst, G. Eggeler, E.P. George, Microstructure evolution and critical stress for twinning in the CrMnFeCoNi high-entropy alloy, *Acta Mater.* 118 (2016) 152-163.